ALGERIAN PEOPLE'S DEMOCRATIC REPUBLIC

MINISTRY OF HIGHER EDUCATION AND SCIENTIFIC RESEARCH

Djilali Liables University of Sidi Bel Abbes
Faculty of Technology
Department of Mechanical Engineering

Thesis

Presented by :

BENAYAD ZOUAOUI

TO GET THE PHD DEGREE

Domain: Science and Technology
Field: Mechanical Engineering
Specialty: Energy and environment

Entitled:

Numerical Investigation of Cooling Electronics Components

Before the jury composed of:

Pr. MAKHLOUF Mohammed	**U.D.L. SBA**	President of the jury
Dr. LAOUEDJ Samir	**U.D.L. SBA**	supervisor
Pr. JUAN PEDRO SOLANO	**U.P.C. SPAIN**	Co-superviser
Dr. MEDBER Mohamed Amin	**U. MASCARA**	Examiner
Dr. BENAMARA Nabil	**U.D.L. SBA**	Examiner

ACADEMIC YEAR: 2020-2021

Acknowledgments

I would like to express my deep gratitude to ***Prof LAOUEDJ Samir*** *as he has always been with me, all along my work, bestowing advice upon me and always showing his availability.*

I am highly indebted with special Thanks to the members who concerned themselves with reading, correcting and evaluating my thesis: ***Pr. MAKHLOUF Mohamed****,* ***Dr. MEDBER Mohamed Amin*** *and* ***Dr. BENAMARA Nabil****. I would like to pay tribute to them here, as I can hardly find adequate words of thanks.*

I am equally indebted to Professor ***JUAN Pedro Solano****, the Engineering Department of Thermal and Fluids, Polytechnic University of Cartagena, Murcia, Spain as well as well the team at the Laboratory of Renewable Energies* ***Mr. Alberto Egea Villarreal*** *and* ***Mr. Antonio Zamora****. Helping with precious documentation, providing insightful advice, valuable suggestions and moral support which, I must confess, gave me a giddy round of pleasures beyond all the stress and constraints.*

Dedications

Every challenging work needs self-efforts as well as guidance of elders especially those who were very close to our hearts My humble effort is dedicated to: The sake of Allah, my creator and my master My great teacher and messenger, Mohammed (May Allah bless and grant him), who taught us the purpose of life.

My undying gratefulness goes to my two shields and mentors in life my dear parents who proved to be the perfect example of the desired parents. I fancy granting my thankfulness to my grandparents, dear brother and sisters for their support and love.

My eternal gratitude goes to my colleagues and friends Mr. DAHMANI Abderraouf and Miss MECIEB Fatima zohra and Miss. BENSAAD Siham, for everything he helped with for the sake of fulfilling this work. To all those whom my memory failed to recall, many thanks for every momentous or trivial thing you have taught me for it was all helpful.

Abstract

Recently, the cooling process for electronics components has attracted many researchers and several techniques for improving the cooling efficiency and heat transfer rate have been demonstrated. One of the best efficient techniques is the introduction of a synthetic jet and the modification of heating surface. In the present study, the form of heating surface, as well as the shape and number of orifices and the signal of the diaphragm has been modified to improve the synthetic jet. These modifications are novel and have been applied for the first time with very good thermal enhancement efficiency for microchannels with synthetic jets applications. This study allowed us to make a quantitative comparison between a basic case with a periodic signal and modified case.

The unsteady flow and heat transfer for the two-dimensional synthetic jet are solved using ANSYS fluent code and k-ω (SST) model is selected to account for fluid turbulence.

Obtained results showed a cooling improvement of about 60% for the modified case with two synthetic jets inclined with 3° and converged form of orifices and 10 µm of undulation heated wall when changing the position of the cavities so as to introduce a bi-periodic signalcompared with the basic case.

Key words: Synthetic jet; (SST) K-ω turbulence model; Undulation heated wall; Nusselt number; Periodic signal; Bi-periodic signal.

ملخص

في الآونة الأخيرة، اجتذبت عملية تبريد المكونات الإلكترونية العديد من الباحثين، وقد تم عرض العديد من التقنيات لتحسين كفاءة التبريد ومعدل نقل الحرارة.

واحدة من أكثر التقنيات فعالية هي إدخال نفاثة اصطناعية وتعديل السطح الساخن. في الدراسة الحالية، تم تعديل شكل السطح الساخن للمكونات الإلكترونية مع تعديل عدد فتحات خروج المبرد و كذلك شكل إشارة الحجاب الحاجز لتحسين النفاثة الاصطناعية. هذه التعديلات جديدة وقد تم تطبيقها لأول مرة و تم الحصول على كفاءة تحسين حراري جيدة جدًا بالنسبة للقنوات الصغيرة ذات التطبيقات النفاثة الاصطناعية. سمحت لنا هذه الدراسة بإجراء مقارنة كمية بين حالة أساسية بإشارة دورية وحالات معدلة.

يتم حل التدفق غير المستقر ونقل الحرارة للنفاثة الاصطناعية ثنائية الأبعاد باستخدام برنامج ANSYS fluent ويتم اختيار نموذج K-ω (SST) لحساب اضطراب السوائل.

أظهرت النتائج التي تم الحصول عليها زيادة في رقم النسلت بنحو60% للحالة المعدلة مع نفاثتين اصطناعيتين مائلتين دات فتحات بانسداد متقارب وبمنحدر3 درجة و 10 ميكرومتر من تموج الجدار الساخن عند تغيير موضع التجاويف واضافة إشارة ثنائية الفترات مقارنة بالحالة الأساسية.

كلمات مفتاحية: نفاثة اصطناعية؛ نموذج الاضطراب K-ω (SST)؛ جدار ساخن مموج؛ رقم نسلت؛ إشارة دورية؛ إشارة ثنائية الفترات.

RESUME

Récemment, le processus de refroidissement des composants électroniques a attiré de nombreux chercheurs et plusieurs techniques permettant d'améliorer l'efficacité du refroidissement et le taux de transfert de chaleur ont été démontrées.

L'une des techniques les plus efficaces est l'introduction d'un jet synthétique et la modification de la surface chauffante. Dans la présente étude, la forme de la surface chauffante ainsi la forme et le nombre d'orifices et le signal du diaphragme ont été modifiés pour améliorer le jet synthétique. Ces modifications sont nouvelles et ont été appliquées pour la première fois avec une très bonne efficacité d'amélioration thermique pour les micro-canaux avec des applications de jets synthétiques. Cette étude nous a permis de faire une comparaison quantitative entre un cas de base avec un signal périodique et des cas modifiés.

L'écoulement instable et le transfert de chaleur pour le jet synthétique bidimensionnel sont résolus à l'aide du code fluide ANSYS et le modèle k-ω (SST) est sélectionné pour tenir compte de la turbulence des fluides.

Les résultats obtenus ont montré une amélioration de refroidissement d'environ 60 % pour le cas modifié avec deux jets synthétiques inclinés avec 3° et forme convergente des orifices et 10 µm d'ondulation de la paroi chauffée quand on change la position des cavités ainsi introduire un signal bi-périodique par rapport au cas de base.

Mot clé : Jet synthétique ; modèle de turbulence K-ω (SST); paroi chauffée ondulée ; nombre de Nusselt ; signal périodique ; signal bi-périodique.

List of Figures

List of Tables

Nomenclature

ε	Rate of dissipation of turbulence energy
ω	Specific dissipation rate
k	Kinetic energy of turbulent fluctuation per unit mass
μ	Dynamic molecular viscosty (kg/ms)
μ_t	Dynamic Turbulent viscosity (kg/ms)
ν	Kinematic molecular viscosity (μ/ρ) (m^2/s)
ρ	Density (kg/m^3)
γ	Radial coordinate
τ	Shear stress
τ_{ij}	Specific Reynolds stress tensor $\left(-\overline{u_i' u_j'}\right)$
α	Production coefficient for specific dissipation rate (Wilcox model)
β	Dissipation rate coefficient for specific dissipation rate (Wilcox model)
β^*	Dissipation rate coefficient for turbulence kinetic energy (Wilcox model)
σ	Reciprocal of turbulent Prandtl number for specific dissipation rate (Wilcox model)
σ_k	Turbulent Prandtl number for kinetic energy ($k-\varepsilon$ model)
σ_ε	Turbulent Prandtl number for kinetic energy ($k-\varepsilon$ model)
σ_ω	Turbulent Prandtl number for kinetic energy ($k-\omega$ model)
ϕ	A generalized dependent variable
δ	Boundary layer thickness
δ_{ij}	Kronecker delta
Ω_{ij}	Mean rotation tensor, $\Omega_{ij} = \frac{1}{2}\left(\frac{\partial U_i}{\partial x_j} - \frac{\partial U_j}{\partial x_i}\right)$
S_{ij}	Mean strain rate tensor, $S_{ij} = \frac{1}{2}\left(\frac{\partial U_i}{\partial x_j} + \frac{\partial U_j}{\partial x_i}\right)$
E_{ij}	Component of rate of deformation
f_β	Bounded vortex-stretching function $\left(7/8 \le f_\beta \le 1\right)$
f_{β^*}	Bounded cross diffusion function $\left(1 \le f_{\beta^*} \le 1.7\right)$
x_k	Cross diffusion parameter
x_ω	Vortex-stretching parameter
x_i	Cartesian space coordinate
y	Coordinate normal to wall (m)
u_i	velocity component in corresponding direction $(m.s^{-1})$
U_∞	Incoming flow velocity $(m.s^{-1})$
$C_{1\varepsilon}$	Dissipation rate equation production coefficient

$C_{2\varepsilon}$	Dissipation rate equation dissipation coefficient
C_{μ}	Eddy viscosity coefficient
Re	Reynolds number in pipe flow based on bulk velocity and pipe diameter
St	The Stokes number
Sr	Strouhal Number
Ω	Womersley number
L	Characteristic length of the cross-flow (m)
i, j, k	Subscripts denotiong Cartesian coordinate directions
x, y, z	Cartesian coordinates
∇	Laplacien
A	Diaphragm amplitude (m)
d_c	Cavity width (m)
d_0	Orifice width (m)
D	Channel width (m)
f	Diaphragm frequency (Hz)
h_c	Convective heat transfer coefficient (W/m^2K)
H	Channel height (m)
L	Heater width (m)
K	Thermal conductivity (W/mK)
L_s	Stroke length
Nu	Nusselt number, hH/k
Re_c	Jet Reynolds number, $2\pi fx0H/\upsilon$
S	Stokes number
t	Time (s)
T	Time period, $1/f$ (s)
T_w	Wall temperature (K)
U_c	Characteristic jet velocity $(m.s^{-1})$
u_0	Velocity through orifice $(m.s^{-1})$
V_i	Micro-channel inlet velocity $(m.s^{-1})$
ρ	Density (kg/m^3)
μ	Dynamic viscosity (kg/ms)
ω	Angular velocity (rad/s)

Abbreviations

DLI :	Direct liquid immersion
TECs :	thermoelectric cooler
SJ :	Synthetic Jet
PCM :	Phase change material
eTECs :	Embedded TECs
CFM :	Change form material
LHP:	Loop Heat pipe
CPL :	Capillary pumped loop
CTE :	Coefficient of Thermal Expansion
DNS :	Direct numerical simulation
RANS :	Reynolds Averaged Navier-Stokes
SST:	Shear Stress Transport
RSM :	Reynolds-Stress Model
LES :	Large Eddy Simulation
FVM :	Finite Volume Method
UDF :	user-defined function

Sommaire

Section 2 : Numerical Approach

Section 3 : Results and Discussion : Part 1

Section 4 : Results and Discussion : Part 2

General Introduction

1. Foreword:

The invention of electricity was a major world revolution, and with the passage of time and the world's entry into the industrial revolution, and with the enormous technological development that we are now witnessing in the field of electronics, innovators have attached great importance to the cooling of electronic devices.

We also know that electric current not only produces electricity, but also generates significant thermal energy. Failure to extract this heat will affect the amount of electricity produced, and more importantly will lead to decreased efficiency and even damage to electronic components and devices, which has prompted researchers to design several ways to cool electronic components.

The goal of researchers studying the phenomenon of electronic component cooling and heat transfer is to be able to understand, predict and control all of these phenomena. To do this, two main approaches can be used: Experimental investigations and Numerical Modelling. The high difficulties of calculating some parameters lead researchers to use numerical modeling as another effective and reliable method for research and development.

2. Purpose and organization of work:

In the context of understanding the phenomenon of heat transfer and cooling of electronic components by synthetic jet, the major objective of this work is to better understand the cooling simulation processes using a computational code such as ANSYS-Fluent. On the other hand, this code is used to study cooling numerically. A comparison was made between the different modified cases (Nusselt number, temperature and velocity field).

This work consists of four sections. The first section is a general description of the different techniques of cooling of electrical components, then an overview to the technique of synthetics and a bibliographical research on this technique.

The second section includes the Numerical Approach. First, It contains Navier-Stokes Equations and Models of Turbulence. Then, we present the Numerical methods.

In the third section of this thesis, we present the first part of the simulations where we change the forme of cases and forme and number of cavities, we fend also the validation as well as the analysis of the results obtained by the simulation of the different modified cases.

In the last section, we present the second part of the simulations where we make a modification on the oscillation signal of the daiphragm and the analysis of the results obtained by the simulation.

The results will be analysed, interpreted and discussed.

At the end, a final conclusion will summarise all the results achieved and give future prospects for development based on this work.

Section 1

Cooling of electronic components

1.1 Cooling systems :

There are different cooling system technologies that can be divided into two main categories:

– **Active cooling systems**

This technique is based on heat transfer by forced convection and requires the use of a mechanical pump to circulate the heat-transfer fluid and an external circuit to remove heat from the system to the outside.

– **Passive cooling systems**

They do not require an external power supply, which reduces the energy cost. Passive cooling can itself be classified in two sections: direct or indirect depending on whether the heat transfer fluid is or is not in contact with the electronic components.

A. Arshad et al [1] summarize the different types of cooling of electronic components :

Types	Methods
Conduction cooling	Conduction circuits, Wedge Lok Technology
Conventional cooling Technologies	Thermo siphons, heat sink, Fan and heat sink, Fan, Heat sink and heat pipe.
Advance cooling Technologies	Cryogencics cooling, Refrigerant cooling, Direct liquid immersion (DLI) cooling, hibrid cooling, thermoelectric cooler (TECs), spray cooling, micro minichannel, cold plate technologies, Synthetic Jet (SJ) cooling.
Hybrid cooling Technologies	Electro wetting, Spot cooling, Vapor chamber cooling, Heat pipes/heat super conductors, Compact heat exchangers, Phase change material (PCM), Micro TECs cooling, Embedded TECs (eTECs), Jet impingment cooling.

Table 1.1. Innovative cooling technologies for thermal management of electronics, [2,3].

1.1.1 Monophasics cooling systems

Monophasics heat exchangers incorporate a structure in which the passage of the coolant is carried out without change of state. The power to be dissipated is evacuated to the outside by conduction, convection and capacitive transport. The fluid is "charged" with the power dissipated by the electronic element, raising the temperature of the fluid. There are two

types of fluid cooling systems: single-phase gaseous cooling systems (mostly air) and liquid cooling systems. [4].

1.1.1.1 Air cooling system

Air cooling systems are used for electronic components with low thermal stress. The main advantages of this cooling system are its relative simplicity and low technical implementation cost.

The exchanges between the electronic element, which is the thermal source and the environment, which is the heat sink, are convective and radiative.

1.1.1.1.1 Natural convection in the air

The electronic element is placed in the ambient air at rest, the difference in temperature between the ambient environment and the electronic element allows an exchange whose exchange coefficient h is between 5 and 25 $W.m^{-2}.K^{-1}$. In order to use power convection for higher levels of power to be exhausted, air cooling systems require fins or honeycomb, giving the cooler a larger exchange surface between the element to be cooled and the ambient environment (see example Figure 1.1). The use of these systems makes it possible to increase the exchange coefficient h up to a ratio of 20 (from 25 $W.m^{-2}.K^{-1}$ to 500 $W.m^{-2}.K^{-1}$) in the case of natural convection [5]. In the case of air convection using an increase in the exchange surface, it is thus necessary to determine the thermal operating point of the cooler to benefit from optimum cooling (Example: determination of the wings spacing).

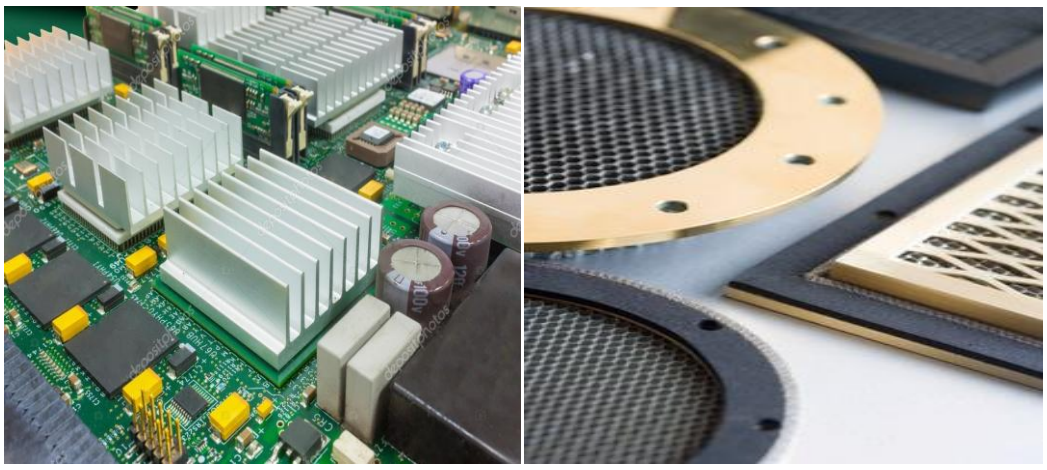

Figure 1.1. Example of a cooling wing and honeycomb to increase the convective exchange surface.

1.1.1.1.2 Forced convection in the air

Forced air blowing through fans is the most widely used method for cooling electronic components due to its simplicity of use, cost and reliability. The air is set in motion by means of a flow generator (ventilator) as shown in the example in Figure 1.2. The exchange coefficient h is of the order of 10 to 500 $W.m^{-2}.K^{-1}$. Piezoelectric ventilator cooling is another cooling technique based on air blowing. The principle of operation is based on a ceramic blade supplied with electric current, which starts to oscillate at very high frequencies. An air movement is created which can increase the convective exchange coefficient by up to 100% compared to a "classic" ventilator-based convective exchange.

With the increase in the thermal density of the components, the radiators have reached dimensions that impact the overall dimensions. The classic example is liquid cooling with water radiators, by analogy with air cooling with air radiators. The heat transfer by sensible heat is about 3000 times higher for water compared to air [6].

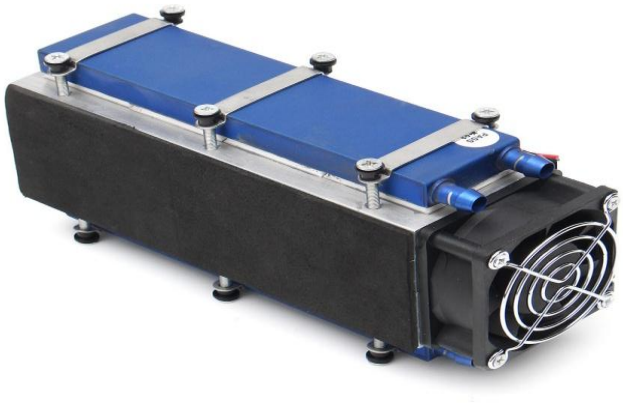

Figure 1.2. Forced air cooling system Radiator.

1.1.1.2 Liquid cooling system

Indirect monophasics liquid cooling is implemented in electronic components in the form of a water plate in which a heat transfer liquid circulates or fluidic pipes attached to the walls to be cooled. A system consisting mainly of a pump and an exchanger allows the heat contained in the heat transfer liquid to be evacuated to the outside of the server. Variations of cold plate liquid cooling are available. For channel diameters between 10 and 800 µm, the cold plate is said to be microchannel (Figure 1.3) and for diameters from 1 to 10 mm, it is said

to be minichannel (Figure 1.4). Above 10 mm, these systems are usually referred to as cold plate [7,8].

Figure 1.3. Micro-channel liquid cooling.

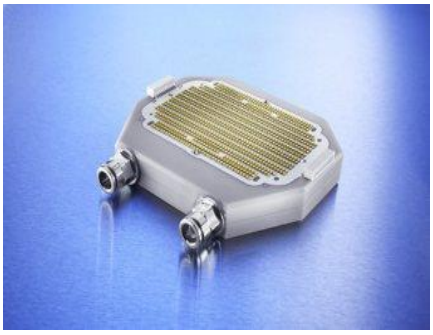

Figure 1.4. Mini-channel liquid cooling.

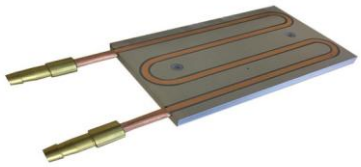

Figure 1.5. Cold plate liquid cooling.

Several studies [9,10] have shown that the properties of this heat transfer fluid vary according to the period of use of the electronic components. For the sizing of the cooling system, it is thus imperative to take into account the degradation of the heat transfer fluid and to take a sizing margin to tolerate these performance drifts. For environments with high/low temperature differences, the use of liquid metals is mandatory. Due to their excellent physical properties and high thermal conductivity, liquid metals are good electrical conductors, allowing the use of electromagnetic or magnetodynamic pumps. This type of pump is based on the coupled use of a magnetic field and an electric current creating a Laplace force driving the fluid through the circuit. Heat flows of around 200W.cm-2 can be evacuated at a flow rate of 0.3 l/min and the loss of hydraulic energy in this case is 15 kPa [11].

Disadvantages to the use of a liquid in a cooling system must be considered: liquid leaks, corrosion, extra weight and finally condensation.

1.1.1.3 Spray cooling

With liquids, several solutions are possible: using the fluid as a simple heat transfer medium, increasing convective exchanges by means of jets, or benefiting from the evaporation of the liquid. Cooling by means of a jet of atomised liquid or "spray cooling". The principle consists in spraying a liquid close to the wall to be cooled (Figure 1.6).

Specifically, the principle is as follows. When, under given pressure conditions, a sufficient flow of heat is applied to a liquid, its temperature rises to a certain value, the boiling temperature, and then an increasing part of it changes to the gaseous state, the temperature remaining substantially constant. The amount of heat required for this transformation of a unit of mass is the enthalpy of vaporization. This phenomenon is reversible, and when it returns to a liquid state (condensation), this amount of heat is released. The circulation of a fluid between two points, in the vapour state in one direction and in the liquid state in the other, therefore allows a transfer of heat from one to the other. Since boiling temperature is an increasing function of pressure, in constant volume systems, pressure and temperature increase simultaneously as more liquid turns to vapour [12]. Figure 1.6 shows the different components of a spray cooling system: condenser, compressor, plate and spray zone.

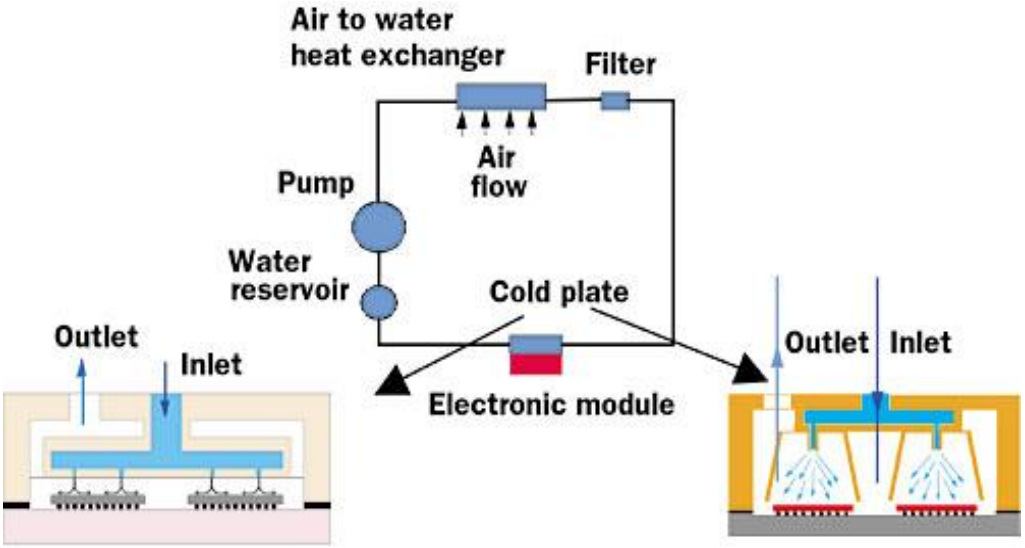

Figure 1.6. Spray cooling principle.

1.1.1.4 Jet cooling

Jet cooling is preferred solution in industrial applications when you want to extract or bring an intense heat flow to a surface. In the field of electronics, the perpetual increase of the

power dissipated by modern components, as well as the constant concern for compactness, have led to the need to find efficient solutions to the problem of heat extraction in confined spaces. This function is often performed by compact heat exchangers whose walls are cooled by impact jets Figure 1.7.

The efficiency of this cooling system depends on the number of jets, the diameter of the jet, the fluid and the liquid flow rate. This type of active cooling requires the installation of a complete hydraulic circuit, as well as a fluid pressurization system. As with spray-cooling, the adjustment of the jet flow rate, the impact zone and the distance of the jet are important parameters to be taken into consideration and require a lot of work upstream of the installation of the system [13].

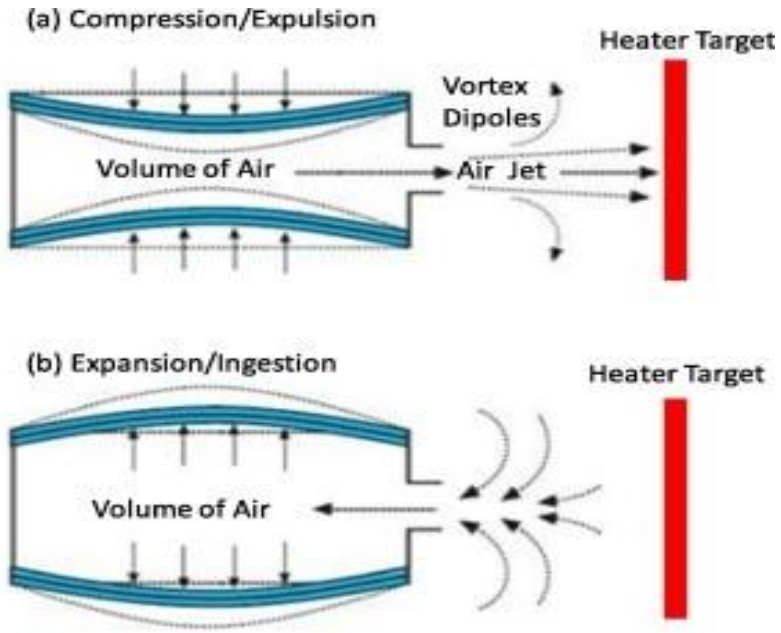

Figure 1.7. Jet cooling.

1.1.2 Diphasic cooling systems

1.1.2.1 Solid-liquid phase change cooling

A phase change material (PCM) is a substance with a high heat of fusion which, by liquefying or solidifying at a certain temperature, is capable of storing or releasing large amounts of energy. The heat is absorbed when the material changes from solid to liquid state, and is released when the material changes from liquid to solid state. The high latent heat of CFMs is effective in absorbing heat and slowing the temperature rise of the electronic chips. Its integration in a cooling system will therefore be ideal for devices that operate periodically.

When the latent heat of the CFM is exhausted, heat is still generated and the temperature rises to a steady state. The heat released by the electronic chip is conducted by the PCM to the outer edge of the heat sink and is dissipated by natural air convection.

Figure 1.8 Using PCM with graphite to cool batteries shows an example of using PCM with graphite sheets to cool lithium batteries.

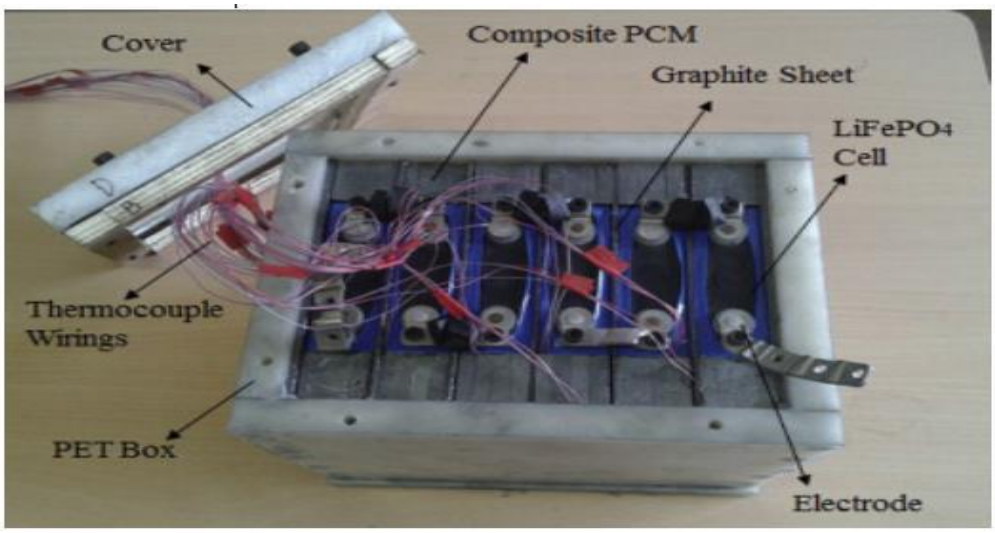

Figure 1.8. Use of PCM with graphite for cooling batteries.

1.1.2.2 Cooling by liquid-vapor phase change

This liquid-vapour phase change cooling method is considered one of the most efficient and adaptable ways to cool energy systems. The amount of heat dissipated depends on the mass flow rate of the heat transfer fluid and its heat of vaporization. The major advantage of this cooling method is that the fluid circulates without any mechanical pump.

1.1.2.2.1 Cooling by immersion in a dielectric fluid

The components to be cooled are placed in a sealed enclosure partially filled with the dielectric liquid.

The heat is dissipated at the surface-liquid interface where the heat exchange takes place via the boiling of the heat transfer liquid. The steam produced is condensed in a heat exchanger cooled by air in natural convection or by liquid in forced convection. This exchanger, also called a condenser, can be external or internal as shown in Figure 1.9.

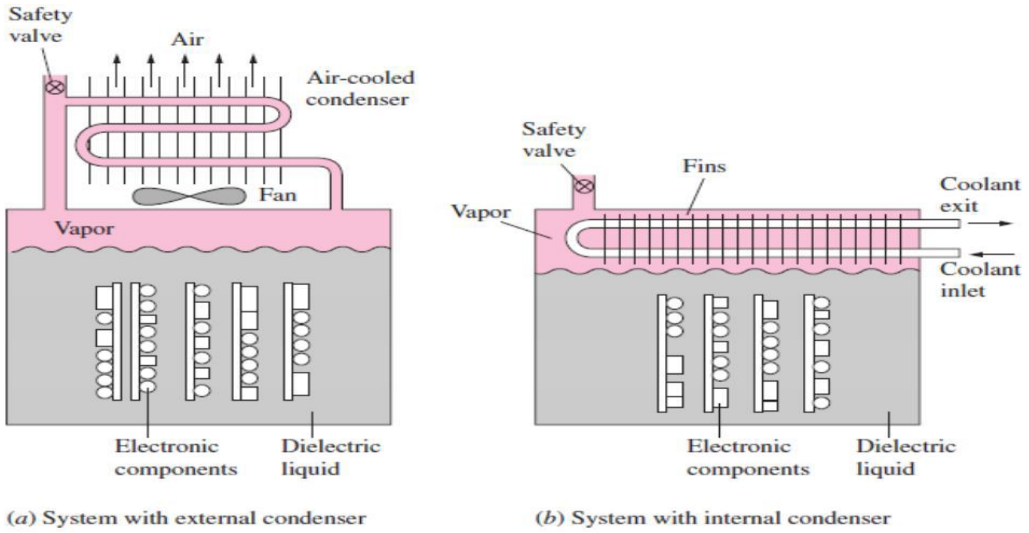

Figure 1.9. Dielectric fluid cooling systems with external (a) internal capacitor (b).

1.1.2.2.2 Heat pipe cooling

The heat pipe is a closed di-phasic cooling system whose operation is based on a closed-loop circulation of the heat transfer fluid. They operate without any moving parts, which reduces noise and requires little maintenance.

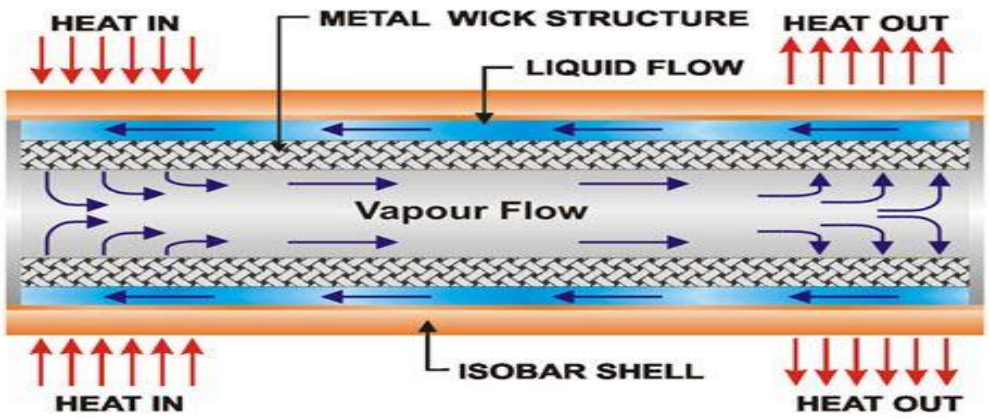

Figure 1.10. Schematic diagram of a heat pipe.

Figure 1.10 shows a schematic diagram of a heat pipe. The capillary structure has a higher thermal conductivity than that of the heat transfer fluid. The fluid is vaporized at the evaporator, which creates a movement of the vapor along the adiabatic section, then the vapor gives up its heat in the condenser by condensing. The amount of condensing heat is transferred through the walls of the heat pipe to an external heat receiver. This condensation

process saturates the capillary structure with fluid. This capillary structure can be made of sintered copper, for example. The pore diameters are in the order of a few microns. The capillary pressure is inversely proportional to the bending radius of the liquid-vapour interface. The difference in saturation, therefore, causes a pressure difference in the capillary structure between the condenser and the evaporator and the medium flows through the capillary structure due to this pressure.

1.1.2.2.3 Thermosiphon cooling

The major difference between a heat pipe and a thermosiphon is that a thermosiphon tube works without a porous wick. The condensate is returned to the evaporator solely by gravitational forces. It is a simple and inexpensive system for transferring heat from the system to the outside. The movement of steam from the evaporator to the condenser is caused by buoyancy forces due to the change in density of the heat transfer medium. Figure 1.11 shows a schematic diagram of a closed tube thermosiphon.

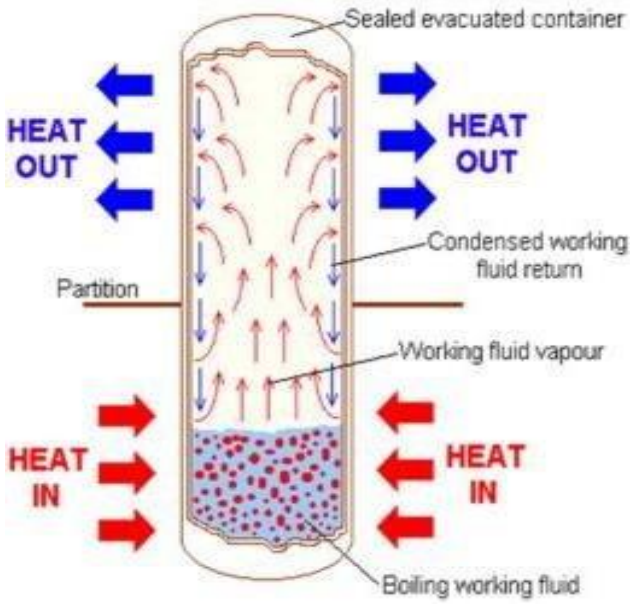

Figure 1.11. Schematic diagram of a thermosiphon in a closed tube.

Thermosiphon tubes are generally closed. They use the process of heat transfer by boiling, and condensation of the heat transfers fluid. They contain a well-defined quantity of heat transfer fluid which plays a predominant role in the transport of thermal energy from one end to the other.

Thermosiphon cooling can be carried out in a loop, which allows the transfer of a quantity of energy from the system to be cooled to the condenser. The circulation of the heat transfer medium takes place in a natural way in pipes connecting an evaporator and a condenser. The heat transfer fluid is evaporated in the evaporator and then transferred to a condenser via a steam line. In the condenser, the heat transfer medium gives up its heat to the environment and returns to the evaporator in a liquid state via a liquid line. This creates a temperature difference and thus a density gradient along the loop. The gravitational force field in the liquid line activates the buoyancy forces in the vapour line. In addition, a thermosyphon uses the difference in saturation pressure between the two sources to cause the heat transfer medium to flow through the loop. The geometric configuration of a thermosiphon loop must be such that condensate can flow back down the evaporator under the forces of gravity. In a state of equilibrium, the buoyant force is equalized by the pressure losses along the pipe.

1.1.2.2.4 Cooling by Diphasic loop cooling CPL and LHP

These diphasic loops work passively thanks to the capillary forces produced in a porous structure such as a heat pipe. They operate on the principle of separation of the two phases in their evolution from one end of the loop to the other. This makes it possible to eliminate liquid-vapour interactions in adiabatic zones, and to independently manage heat losses in each phase during sizing. Only the evaporator part is equipped with a capillary medium to allow maximum pressure jump. This capillary medium must compensate for the pressure drops generated by the circulation of the fluid in the various elements of the loop.

Two systems are distinguished: CPL [14] and LHP. These devices have different configurations depending on the position of the tank in the circuit. Figure 1.12 shows the two different LHP and CPL systems.

In the CPL loop, the receiver and the evaporator are separated by a liquid line. The LHP loop is characterized by a strong thermo-hydraulic coupling between the tank and the evaporator which helps to stabilize the loop: the tank and the evaporator are connected as only one component.

They are separated by two porous media: a primary porous medium made of fine pores in order to develop sufficient capillary pressure and circulate the fluid in the loop, and a secondary porous medium made of larger pores in order to control the flow of heat transfer fluid between the tank and the evaporator.

The flow pattern in separate pipelines leads to higher maximum performance than heat pipes. However, the operation of diphasic loops can be very unstable and sometimes very difficult at low power.

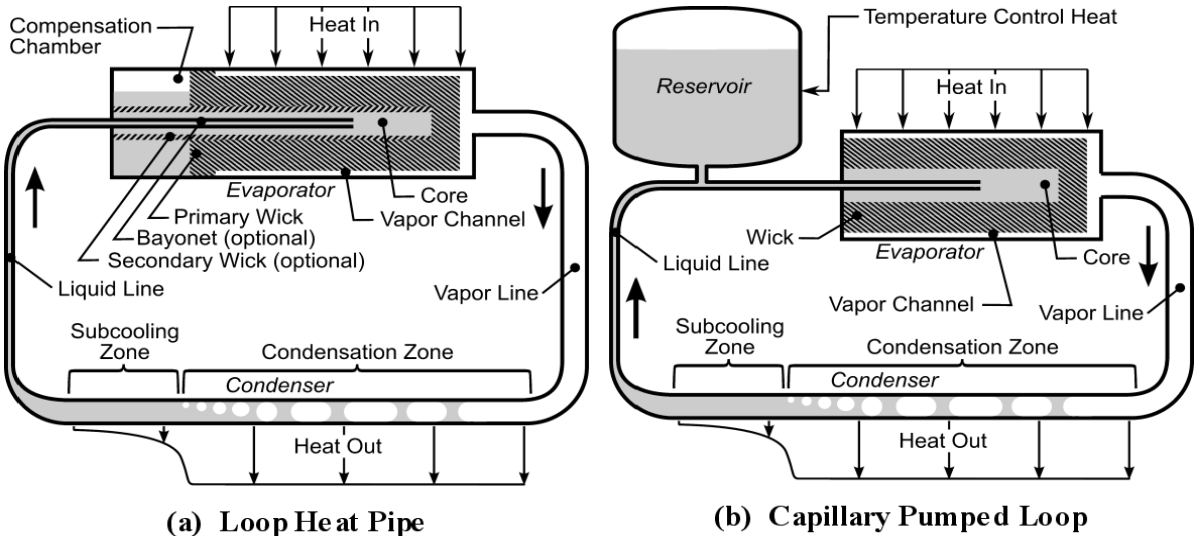

Figure 1.12. Di-phase loops LHP and CPL.

The tank in the CPL and LHP loops acts as a regulator. It sets the system pressure and thus the evaporation temperature of the heat transfer medium. It serves as an expansion vessel in the loop, particularly during the loop start-up or power variation phases. It also provides a liquid reserve to compensate for the presence of micro-leaks in the circuit.

1.1.3 Thermal drainage

Heat dissipation by thermal conduction is preferred when, for weight, space and cost reasons, the use of thermal convection is not possible. Thermal conduction is chosen for mechatronic components with low induced thermal power (less than 10W), for printed circuit boards or housings of electrical systems [15].

Thermal drains must have a good thermal conductivity in order to evacuate heat quickly but also have a coefficient of thermal expansion close to that of the ceramic substrate, in order to reduce the thermomechanical stresses between the different components. They must therefore have the lowest possible density.

The first generation of thermal drains was made from monolytic materials: aluminium or copper. However, these two materials have a very high CTE, which generates mechanical stresses during operation that deteriorate the reliability of the assemblies (Table 2).

In order to further improve the properties, a second generation of drains has been developed, this time using composites, in particular aluminium reinforced with silicon carbide (Al/SiC) particles but also alloys such as Invar or Kovar. These two alloys are interesting because of their low coefficient of expansion but have a much too low thermal conductivity [16].

	1st generation thermal drains				2nd generation thermal drains		
	monolytic materials		Copper alloys				
materials	**Al**	**Cu**	**Cu-W (10-20% Cu)**	**Cu-Mo**	**Invar**	**Kovar**	**AL/SiC**
Thermal conductivity ($W.m^{-1}k^{-1}$)	218	400	180 - 200	160 - 170	13	17	180
CTE ($10^{-6}.k^{-1}$)	23	17	6,5 - 8,3	7,0 - 8,0	1,7 - 2,0	5,0	8,7
Density	2,7	8,9	15,7 - 17,0	10,0	8,0	8,4	3,0

Table 1.2. Thermal properties of 1st and 2nd generation thermal drains.

In order to obtain properties close to the ideal material, the third generation of thermal drains combines metallic matrices such as aluminium or copper, with high thermal conductivity reinforcements such as carbon fibres, carbon nanofibres, carbon nanotubes, SiC particles or diamond particles [17].

1.1.4 Peltier cooling

One possibility to produce refrigeration without the use of refrigerant mechanisms and flows is to use a chiller that relies on thermoelectric effects. Considering a closed circuit formed by two conducting wires, made of different materials, in contact at each end. By heating one of the junctions, an electric current starts to flow in the circuit. These thermoelectric effects that result from the coupling between the phenomenon of thermal conduction and that of electrical conduction. If an electrical potential difference is applied to the circuit, a cooling effect result. The cold junction cools down and the hot junction heats up. This is the Peltier effect on which thermoelectric cooling is based.

In practice, in order to improve performance in terms of power, efficiency and temperature difference, thermoelements are multi-staged, each stage comprising a decreasing number of Peltier junctions mounted in parallel, resulting in a pyramid shape, with the lower stages having to pump the heat dissipated at the hot end of the upper stages Figure 1.13.

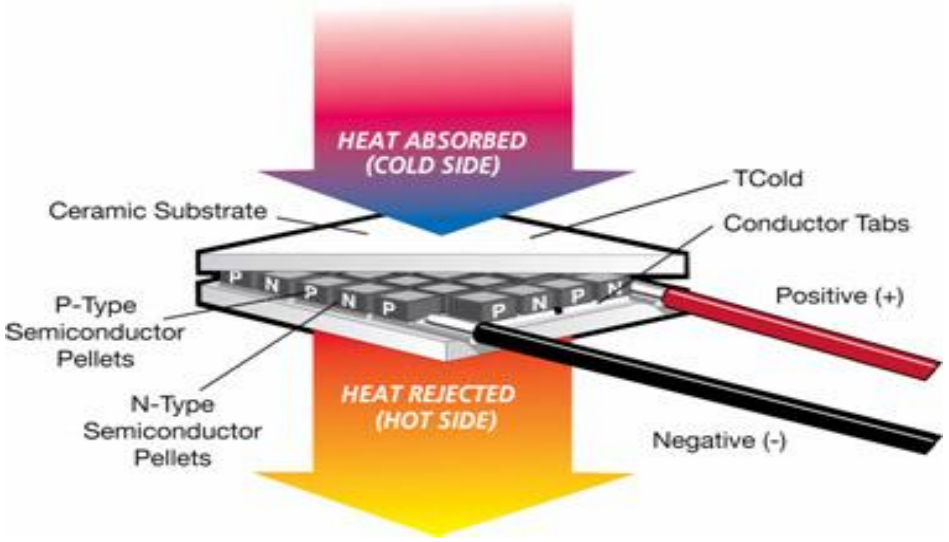

Figure 1.13. Peltier Effect**.**

1.2 Generality on Synthetic Jet:

1.2.1 Introduction

Active flow control is one of the most active areas in applied aerodynamics. The interests are both practical and fundamental. Of all the actuators available for flow control, synthetic jets have demonstrated their effectiveness in increasing mixing and controlling disbonding. The main advantage of synthetic jets over continuous blowing or suction is that they provide virtually the same performance improvements at zero momentum rates. But there is another reason for this. The synthetic jet provides an unsteady solution in contrast to blowing and suction. This difference allows for effective control by coupling with the natural frequencies of vortex detachments. In the end, the desired effects are:

- Forcing the flow in frequency. The instabilities disappear in front of the predominance of the unsteady effects of the actuator;
- Increasing the parietal friction, which delays the appearance of possible detachment

  Glue back the boundary layer.

The synthetic jet is embedded in the wall where control of the boundary layer peeling is desired. The two phases of blowing and suction contribute effectively to the control. In addition, they do not require complex piping systems because the expulsion of momentum is only due to the periodic movement of the diaphragm or piston at the bottom of a cavity.

To study the efficiency of this actuator, various key parameters must be analysed: the frequency and amplitude of the excitation, the time evolution of the jet velocity, the size and position of the actuator.

1.2.2 Working Principle

The schematic diagram of the principle of operation of a synthetic jet is shown in Figure 1.14. A typical actuator consists of a cavity open upwards through a small slot and a diaphragm or membrane which generates the flow inside the cavity. The periodic motion of the diaphragm varies the volume of the cavity. This periodic movement consists of two phases, the suction phase, when the volume of the cavity increases where the fluid enters the cavity through the slot and the blowing phase, when the volume of the cavity decreases. The movement generates a flow that separates at the borders of the slot and is transformed into a pair of vortices generated at the edges of the slot, of the "round smoke" type if the orifice is circular and two parallel vortices in the case of a rectangular orifice. These vortices moves by their own induced velocity. The repetition of the suction and blowing phases makes it possible to inject unsteady structures into the flow and to increase the efficiency of the control compared to stationary solutions such as continuous suction or blowing.

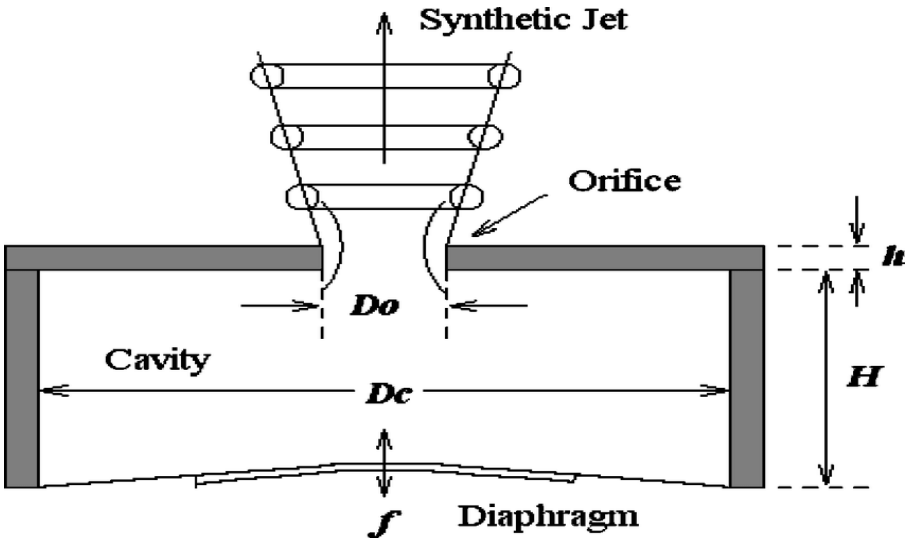

Figure 1.14. shematic of a synthetic jet actuator.

1.2.3 Characteristics parameters effecting the flow field of Synthetic Jet

Figure 1.15 summarize the different parameters effecting the flow field of Synthetic Jet for cooling of electronic components [1]:

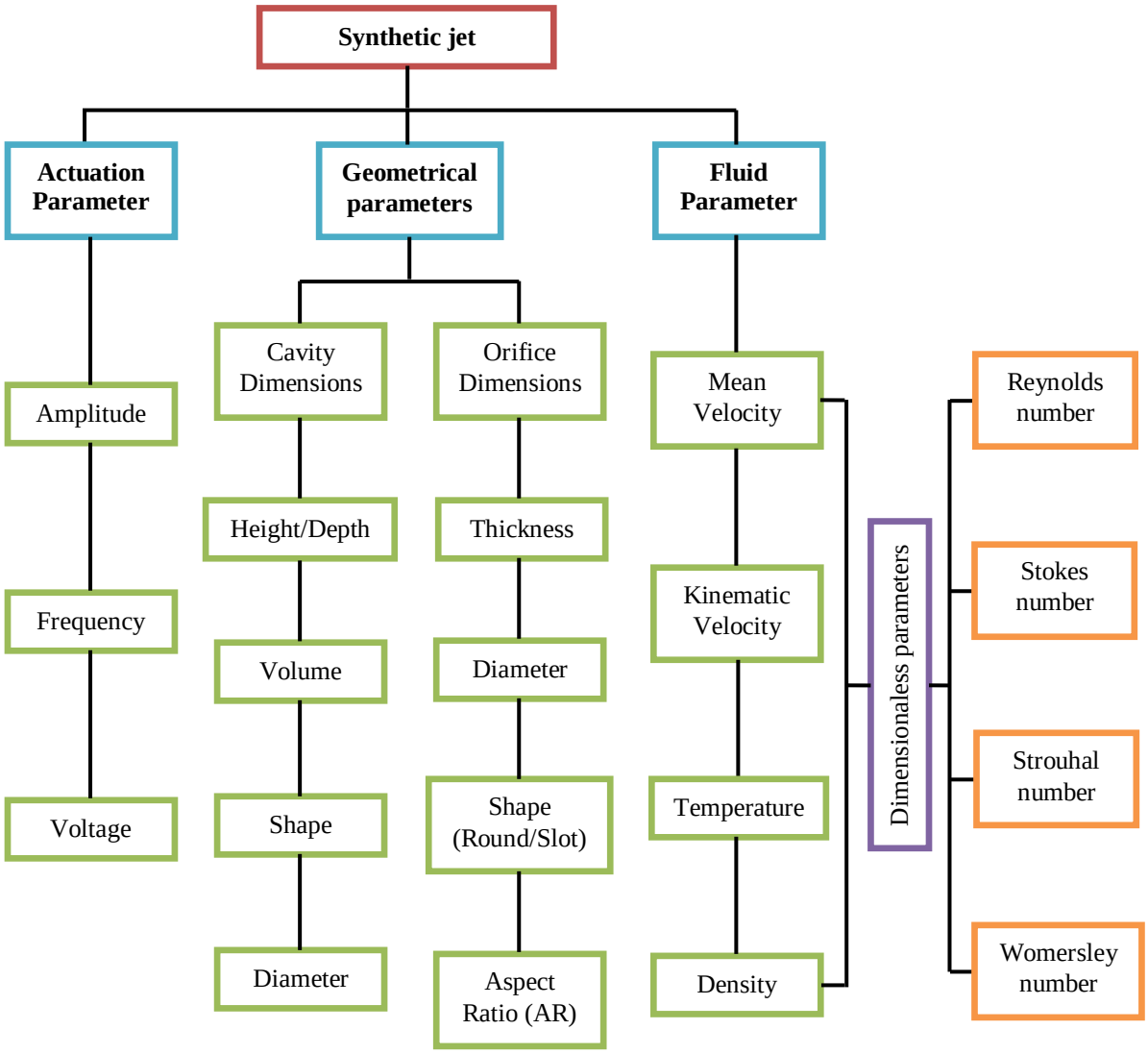

Figure 1.15. Characteristics parameters effecting the flow field of Synthetic Jet [18].

1.2.4 Reynolds Number

– Reynolds number based on velocity scale :

Reynolds number based on orifice width d and velocity U_0.

$$Re_{U_0} = U_0 d / v \quad (1.1)$$

With

U_0: Average over a period of time of the jet ejection velocity at Center of the orifice.

$$U_0 = L/T = \frac{1}{T}\int_0^t u_0(t)dt \tag{1.2}$$

Alternatively, Holman et al [19] define another Reynolds number based on the orifice width d and the space-time averages of the jet velocity at the outlet $\overline{U}$ during the ejection phase

$$Re_{\overline{U}} = \overline{U}\, d/\upsilon \tag{1.3}$$

With

$\overline{U}$: Space-time average of the jet speed at the exit of the orifice during the ejection phase

$$\overline{U} = \frac{1}{T}\frac{1}{S}\int_S \int_0^t u(x,t)dtdS \tag{1.4}$$

S: Orifice outlet section.

x: Transverse coordinate.

$u(x,t)$: Instantaneous velocity of the jet at the orifice outlet.

It can be noted that, taking into account the velocity profile in the outlet section of the orifice during the ejection phase, the velocity scales used to construct the Reynolds numbers Re_{U_0} and $Re\overline{U}$ are linked by the relation :

$$\overline{U} = 2U_0 \tag{1.5}$$

– Reynolds number based on the impulse

$$Re_{I_0} = I_0/\mu d = \frac{1}{\upsilon}\int_0^\tau u_0^2(t)dt \tag{1.6}$$

With:

I_0: movement quantity per unit width

$$I_0 = \rho d \int_0^\tau u_0^2(t)dt \tag{1.7}$$

ρ: density (kg/m^3)

μ: dynamic viscosity

1.2.5 Stokes Number

The Stokes number is given by

$$St = \sqrt{\frac{\omega_j D_j}{\upsilon}} \tag{1.8}$$

Where D_j is the slot diameter and ω_j is the oscillation speed. This formulation is typical for the studies of the synthetic jet, in other applications it is known by the name of Roshko. Holman et al [19], have shown that the criterion for the formation of structures vortices can be expressed as $Re_j/S^2 > K_j$ or $K_j \approx 1\ and\ 0.16$ for jets two-dimensional and axisymmetric synthetics, respectively.

1.2.6 Strouhal Number

Dimensionless number allows to compare the characteristic advection time of the vortex structures emitted by the synthetic jet d/U_0 to the characteristic working time of the actuator $1/\omega$ defined from the average velocity of the jet at the center of the orifice during the ejection phase U_0, the frequency f of membrane actuation and the width of the slot d

$$Sr = fd/U_0 = d/L_0 \tag{1.9}$$

And can also be expressed in terms of Reynolds and Stokes numbers

$$1/Sr = U_0/fd = \overline{U}/\omega d = (\overline{U}d\ /\nu)/(\omega d^2/\nu) = Re_{U_0}/St^2 \tag{1.10}$$

With

$$\omega\ =\ 2\pi f \tag{1.11}$$

1.2.7 Womersley number [1]

Womersley number (Ω) is the dimensionless number that relates pulsatile flow frequency with the viscous effects which is defined as [20–22]

$$\Omega = \sqrt{\frac{Transient\ Inertia\ Force}{Viscous\ Force}} = \sqrt{\frac{2\pi f\omega^2}{\upsilon}} \tag{1.12}$$

1.3 Bibliographical research on the development of Synthetic Jet

With the development of technology in the electronic field especially speed and resistance, the electronics components become more powerful and increasingly small. The components can dissipate several hundred Watts per square micro-meter, thus requires a cooling process. Several cooling techniques have been developed with the aim of improving the heat transfer rate and increasing the efficiency of the cooling systems [23]. Recently, to improve the performances of cooling and the methods of transport of heat, this with amelioration of thermal management in elec-tronic systems S.V. Garimella et al. [24]. Research studies focused on the use and the development of the cooling technique based synthetic jet.

Synthetic jets are a common method for many fluid engineering applications, such as boundary-layer separation control, jet vectoring, heat transfer enhancement, better mixing of fuel in the engine combustion chamber and creation of local turbulence. Synthetic jets can deliver similar cooling effects to conventional steady flow impinging jets without the need for an external air supply system. The main issue about synthetic jet is the enhancement of heat transfer rates or increasing of uniformity on the impingement surface by the control of jet flow. Due firstly to the important role of the synthetic jets in heat transfer enhancement techniques and secondly to the high complexity of the flow structure, the synthetic jet has received considerable research attention.

Campbell and al [25] illustrated the usage of synthetic air micro jets for powerful cooling of laptop processors while different researchers established the viable software of synthetic jets for excessive strength digital cooling via an included active heat sink [26,27]. Throbbing or discontinuous impinging planes are via and big usual to enhance the warm temperature circulate while contrasted with relentless planes, no matter the truth that there stays a scarcity of agreement at the degree of the upgrade and for sure situations the warm temperature flow may even be hindered [28,29].

T. Persoons et al. [30] imposed a margin for the Reynolds number and he modified several parameters which are the height, the diameter of the tube, the distance between the entry and the exit of the orifice, and he compared the effect of each modification on the Nusselt number. Other researchers improve the importance of the changement of the characteristics of the heated surface, Sagot. [31] imposed a change on the heated surface contact by using different corrugations and the com-parison of the results has shown that the

rectangular corrugation gives a higher Nusselt number which is better than both: the triangular corrugations and the surface without corrugation. The distance between the orifice and the heated surface is one of the major factors that influences the heat transfer by synthetic jet and have been studied and proven by many researchers experimentally [32-34] and numerically using ANSYS Fluent code where the unsteady Navier–Stokes equations and the convection–diffusion equation were solved using a fully unsteady [35], experimental study based on the characteristic of synthetic jet impinging upon a vertical heater, and results showed that the heat transfer has the higher performance with a jet-to-surface spacing between 5–10 [36]. Another experimental investigation by P. Gil and J. Wilk [37] studied the effect of the synthetic jet generated by special actuator consisting in a plexiglass cavity and a loudspeaker on the heat transfer phenomenon. the different modifications of the parameters are frequency f = 5 / 600 Hz, root mean square voltage E = 1, 2, 3, 4, 6 V and for the Changes of actuator geometry we found orifice diameters d = 9, 15, 24 mm, orifice thickness t = 3, 5, 20 mm and cavity depth H = 20, 40, 60 mm. And for the parameters: Reynolds number from 3600 to 22950, jet-to-surface spacing x/d = 1 / 20 and the dimensionless stroke length L_0= 0.84 / 170.5, the results are compared and confirmed by literature data in the considered test range.

Different alternative techniques have been investigated experimentally to increase the heat transfer such as the introduction of multi-orifices into the cavity [38] or using multi-cavities is using Particle Image Velocimetry (PIV) [39, 40]. G. Paolillo et al [41] studied experimentally the influence of impinging quadruple synthetic jets for different configuration monopole-like, dipole-like, quadrupole-like and 90-degrees-circularly-shifted-jets for Reynolds = 4000 and Strouhal numbers = 0.2, results indicated that that the 90-degrees-circularly-shifted-jets configuration give the highest heat transfer rates. Luo et al [42] used an innovating technology of cooling which is based on an actuator with a double injection of vectorial synthesis dual synthetic jet in experiment work, knowing that the heat transfer influences domain has been established and validated. In other side, L.D. Mangate, M.B. Chaudhari [38] applied multiple-orifice synthetic jet for cooling the electronic components to improve the heat transfer. Chaudhari et al [43] studied the influence of the addition of orifices around the main orifice for different configurations of satellite orifices with and without the centre orifice and the results shown that the number of satellite orifices affects on the heat transfer and the satellite orifices with the centre orifice gave a relatively high heat transfer coefficient at lower axial distances. Where-as, Fanning et al [44] established two synthetic jets adjacent and they modified the height between the orifices — wall as the distance between the

two, the results proved that there is an improvement in the transferred heat and the convection coefficient.

Another factor is the shape of the opening orifice. Xiao-ming [45] investigated experimentally the efficiency of different opening hole forms including square and rectangular shapes. Results indicated that the synthetic jet with the rectangular orifice was more efficient. Furthermore, the comparison between the rectangular and the elliptic shapes are experimentally tested and showed that the rectangular orifice develops stronger streamwise vortices [46]. Chaudhari et al [47] worked on the influence of the shape of the orifice of a synthetic jet on the phenomenon of cooling by the introduction of three types of orifice: rectangular, cylindrical and square forms with a change of the parameters founded that the form square gives the maximum of heat transfer. Another experimental investigation compared a circular and chevron opening hole forms for an impinging synthetic jet and results showed that for the chevron opening hole shape the heat transfer is greater up to 20% compared to the circular opening hole shape [48].

The control of the synthetic jet in order to perform their efficiency was widely used such as acoustic excitation [49]; using multi-channel swirl generators [50]; nozzle with obstructions [51]. Several studies were carried out to increase the heat transfer rates of synthetic jets. Hsu et al [52] made a comparison of double acting synthetic jets with single-acting synthetic jets. The convective heat transfer was increased in more than two times. A double-acting synthetic jet revealed good potential with significant vorticity enhancement for the design of synthetic jet in heat transfer applications. Cadirci et al [53] showed the effect of an oscillatory zero-net-mass flux device and vortex actuator on the laminar boundary layer; it was appeared that this technique produced qualitatively different flow regimes depending on its actuation parameters. Nuntadusit et al [54] studied the flow and heat transfer characteristics of multiple swirling impinging jets. The use of this technique offered higher heat transfer rates on impinged surfaces than the multiple conventional impinging jets of all jet-to-jet distances. Thieler et al [55] studied the effect of nozzles arrangement on the heat transfer of multiple impinging jets with square/circular arrangements; it was observed that jet arrangement affects the flow characteristics with a slight influence on heat transfer. Yu et al [56] investigated the heat transfer produced by a single row of impinging jets inside a confined channel with different triangle tabs orientations at the jet exits. Results showed that the presence of tabs increased the jet core velocity, induces array pairs of vortices and enhances the heat transfer. In other work Yu et al [57] investigated the effect of the cross-

flow-to-jet Reynolds number ratio and cross-flow holes arrangement on the jet impingement behaviors. The tab-excited jet impingement behaviors in a confined channel with non-uniform cross-flow. Results showed that the effect of the tabbed excitation worsened the convective heat transfer near impingement region inside a cross-flow channel as compared to the absence of initial cross-flow. Results showed that the convective heat transfer coefficients are increased up to 25% by the tabbed excitation but only a 10% of improvement was reported for the situation with the initial flow. A new method of cooling by synthetic jet, it is by atomizing water is investigated experimentally by W. He et al [58], the idea is to use a dual synthetic jet actuator. The maximum atomization rate is 3.4 L/h at a control frequency of 700 Hz and a control voltage of 210 V, the results founded that the new method of spray cooling reaches as 59 W/cm2 and the cooling capacity is mainly influenced by the Reynolds number of the dual synthetic jet and the volume flow of water. L. Mangate, et al [59] studied the impact of a multiple-orifice synthetic jet of a circular, oval and diamond shapes are experimentally studied at different Stokes numbers, the results showed that the average Nusselt number obtained with a a multiple-orifice synthetic jet is 75% higher than with a single orifice synthetic jet using the same input power to the actuator of the synthetic jet. The diamond-shaped multiple-orifice gives better thermal performance compared to other shapes.

In the last year, a lot of experimental and numerical researchers worked to study the physical evolution between heated plan surface and caloporter fluid in high density.

A. Agrawal, G. Verma [60] gave a comparison between a continuous jet and synthetic jet where they have used the experimental results to mention the importance of the synthetic jet to the thermal transfer. Al-Atabi [61] studied the homogeneity of the fluid injected by a synthetic jet to reduce the high rate of shearing of the coolant injected and to minimize the damage to sensitive materials.

On the other side, there have been several studies that focused on the effect of the cavity shape on the synthetic jet performance and the improvement in the heat transfer characteristics. Results showed that the basic cylindrical shape maximized momentum flux and provides better performance from an experimental work [62], Lv Yuan-wei et al [63] carried out numerical investigation based ANSYS Fluent code on the effect of the cavity and orifice dimensions and the excitation frequency of the actuator on the synthetic jet fluidic characteristics. Obtained results showed that the orifice diameter and thickness, as well as the cavity depth and diameter, had major influence on the synthetic jet fluidic characteristics. Another experimental work tested the modification on the cavity using silicone elastomer

membranes together with either soft composite or rigid neodymium magnets, and they found good results for low-frequency range [64].

Heat transfer produced by a synthetic jet depends on a number of parameters such as Reynolds number of the jet, Strouhal number, stroke length, etc. It is well known that the geometry of the orifice nozzle have a significant effect on the heat transfer produced by the synthetic jet. Chungsheng Yao et al [65] investigated the effect of the jet produced by the orifice nozzles with contoured outlets. Results showed that the local heat transfer produced was up 20-30% higher than that produced by a simple square orifice nozzle.

The change in function of oscillation mode in the cavity of synthetic jet proved that the sinusoidal function is better than the triangular function [66]. Numerical investigation carried out by Zhang et al [67] in which three wave forms for synthetic jet including sinusoidal, rectangular and triangular forms for Strouhal number (St) between 0.012– 2.4 have been investigated. Reported results showed that at $St < 0.06$ the rectangular jet is better than the sinusoidal and triangular jets, and for St number ranging between 0.24 to 0.48, triangular jet is better. Further, numerical investigation based Computational Fluid Dynamics (CFD) and the open-source OpenFOAM code has been carried out by King and Jagannatha [68]. Results indicated that the non-sinusoidal function gave an improvement in heat transfer than sinusoidal function.

Section 2

Numerical Approach

2.1 Navier-Stokes Equations and Models of Turbulence [69]

2.1.1 Navier-Stokes Equations

2.1.1.1 The continuity equation

The first equation is the continuity equation (the balance equation for mass) which reads [70]

$$\dot{\rho} + \rho v_{i,j} = 0 \tag{2.1}$$

Change of notation gives

$$\frac{d\rho}{dt} + \rho \frac{\partial v_i}{\partial x_i} = 0 \tag{2.2}$$

For incompressible flow (ρ = const) we get

$$\frac{\partial v_i}{\partial x_i} = 0 \tag{2.3}$$

2.1.1.2 The momentum equation

The next equation is the momentum equation. We have formulated the constitutive law for Newtonian viscous fluids [70]

$$\sigma_{ij} = -P\delta_{ij} + 2\mu S_{ij} - \frac{2}{3}\mu S_{kk}\delta_{ij} \tag{2.4}$$

$$\tau_{ij} = 2\mu S_{ij} - \frac{2}{3}\mu S_{kk}\delta_{ij} \tag{2.5}$$

Inserting Eq 2.5 into the balance equations, Eq (2.6), we get Eq (2.7)

$$\rho \frac{dv_i}{dt} = \frac{\partial \sigma_{ji}}{\partial x_j} + \rho f_i \tag{2.6}$$

$$\rho \frac{dv_i}{dt} = -\frac{\partial P}{\partial x_i} + \frac{\partial \tau_{ji}}{\partial x_j} + \rho f_i = -\frac{\partial P}{\partial x_i} + \frac{\partial}{\partial x_j}\left(2\mu S_{ij} - \frac{2}{3}\mu \frac{\partial v_k}{\partial x_k}\delta_{ij}\right) + \rho f_i \tag{2.7}$$

where μ denotes the dynamic viscosity. This is the Navier-Stokes equations (sometimes the continuity equation is also included in the name "Navier-Stokes"). It is also called the transport equation for momentum. If the viscosity μ is constant it can be moved outside the derivative. Furthermore, if the flow is incompressible, the second term in the parenthesis on the right side is zero because of the continuity equation. If these two requirements are satisfied, we can also re-write the first term in the parenthesis as

$$\frac{\partial}{\partial x_j}\left(2\mu S_{ij}\right) = \mu \frac{\partial}{\partial x_j}\left(\frac{\partial v_i}{\partial x_j} + \frac{\partial v_j}{\partial x_i}\right) = \mu \frac{\partial^2 v_i}{\partial x_j \partial x_j} \tag{2.8}$$

because of the continuity equation. Eq (2.7) can now – for constant μ and incompressible flow – be written

$$\rho \frac{dv_i}{dt} = -\frac{\partial P}{\partial x_i} + \mu \frac{\partial^2 v_i}{\partial x_j \partial x_j} + \rho f_i \tag{2.9}$$

In inviscid (potential) flow, there are no viscous (friction) forces. In this case, the Navier-Stokes equation reduces to the Euler equations.

$$\rho \frac{dv_i}{dt} = -\frac{\partial P}{\partial x_i} + \rho f_i \tag{2.10}$$

2.1.1.3 The energy equation [70]

We have derived the energy equation which reads

$$\rho u - v_{i,j}\sigma_{ji} + q_{i,i} = \rho z \tag{2.11}$$

where u denotes internal energy. q_i denotes the conductive heat flux and z the net radiative heat source. For simplicity, we neglect the radiation from here on. Change of notation gives

$$\rho \frac{du}{dt} = \sigma_{ji} \frac{\partial v_i}{\partial x_j} - \frac{\partial q_i}{\partial x_i} \tag{2.12}$$

we formulated the constitutive law for the heat flux vector (Fourier's law)

$$q_i = -k \frac{\partial T}{\partial x_i} \tag{2.13}$$

Inserting the constitutive laws, Eqs (2.4) and (2.13), into Eq (2.12) gives

$$\rho \frac{du}{dt} = -P \frac{\partial v_i}{\partial x_i} + \underbrace{2\mu S_{ij} S_{ij} - \frac{2}{3}\mu S_{kk} S_{ii}}_{\Phi} + \frac{\partial}{\partial x_i}\left(k \frac{\partial T}{\partial x_i}\right) \tag{2.14}$$

where we have used $S_{ij}\, \partial v_i / \partial x_j = S_{ij}\left(S_{ij} + \Omega_{ij}\right) = S_{ij} S_{ij}$ because the product of symmetric tensor, S_{ij}, and an anti-symmetric tensor, Ω_{ij}, is zero. Two of the viscous terms (denoted by Φ) represent irreversible viscous heating (i.e. transformation of kinetic energy into thermal energy); these terms are important at high-speed flow (for example re-entry from outer space) and for highly viscous flows (lubricants). The first term on the right side represents reversible heating and cooling due to compression and expansion of the fluid. Equation (2.14) is the transport equation for (internal) energy, u.

Now we assume that the flow is incompressible (i.e. the velocity should be smaller than approximately 1/3 of the speed of sound) for which

$$du = c_p dT \tag{2.15}$$

where cp is the heat capacity so that Eq. 2.14 gives (cp is assumed to be constant)

$$\rho c_p \frac{dT}{dt} = \Phi + \frac{\partial}{\partial x_i}\left(k \frac{\partial T}{\partial x_i}\right) \tag{2.16}$$

The dissipation term is simplified to $\Phi = 2\mu S_{ij} S_{ij}$ because $S_{ii} = \partial v_i / \partial x_i = 0$. If we furthermore assume that the heat conductivity coefficient is constant and that the fluid is a gas or a common liquid (i.e. not an lubricant oil), we get

$$\frac{dT}{dt} = \alpha \frac{\partial^2 T}{\partial x_i \partial x_i} \tag{2.17}$$

where $\alpha = k/(\rho c_p)$ is the thermal diffusivity. The Prandtl number is defined as thermal diffusivity

$$Pr = \frac{\upsilon}{\alpha} \tag{2.18}$$

where $\nu = \mu/\rho$ is the kinematic viscosity. The physicalmeaning of the Prandtl number is the ratio of how well the fluid diffuses momentum to how well it diffuses internal energy (i.e. temperature). The dissipation term, Φ, is neglected in Eq (2.17) when one of two assumptions are valid:

A. The fluid is a gas with low velocity (lower than 1/3 of the speed of sound); this assumption was made when we assumed that the fluid is incompressible
B. The fluid is a common liquid (i.e. not an lubricant oil). In lubricant oils the viscous heating (i.e. the dissipation, Φ) is large. One example is the oil flow in a gearbox in a car where the temperature usually is more than $100^o C$ higher when the car is running compared to when it is idle.

2.2 Turbulence models [71]

2.2.1 Nature of turbulence

Turbulent flows are highly chaotic flows because the convective term no-linear is more important than viscosity. To characterize such a flow, the Reynolds number of the flow is denoted as follows: if U is a value characteristic of the flow velocity and L is a scale characteristic of the flow, then the convective term is all the more preponderant the greater the Reynolds number given by Eq (2.19).

$$R_e = \frac{U\,L}{\nu} \tag{2.19}$$

On the one hand, at each point in the flow, the values of velocity and pressure chaotically fluctuate over time, and on the other hand, if one moves in the flow at a given point in time t, the observed fluctuations in velocity and pressure are more or less significant. Despite the chaotic nature of turbulent flows, there is a spatio-temporal coherence that is characterized by the presence of structures called eddies. Vortices have different sizes and characteristic times and exchange energy with each other. Each vortex of characteristic size l is associated with a Reynolds number $R_e(l) = \frac{u(l)l}{\nu}$. The largest eddies have sizes close to that of the mean flow, known as the integral scale. They are produced by the velocity gradients of the mean flow and carry most of the turbulent kinetic energy of the flow. But these large structures are unstable and they break down into smaller and smaller structures with less and less energy - this is the Kolmogorov inertial cascade phenomenon - until they reach a scale l where the Reynolds number $R_e(l)$ is so small that the effects of molecular viscosity become preponderant and dissipate energy efficiently. The minimum scale reached by the vortices is called the Kolmogorov scale.

In order to better illustrate the phenomenon of energy transfer from large to small eddies, it is necessary to look more specifically at the effects due to the no-linear convective term. For this, consider the simple case of the no-viscous Burgers equation

$$\frac{\partial u}{\partial t} + u\frac{\partial u}{\partial x} = 0 \tag{2.20}$$

We start from an initial condition of the form $u(x, t_0) = U\cos(Kx)$ where the flow has only one characteristic vortex size: $\frac{1}{K}$. By doing a Taylor development in time, we get

$$u(x,t_0+\delta t) = u(x,t_0) + \delta t \left.\frac{\partial u}{\partial t}\right|_{t_0} + O\left(\delta t^2\right) \quad (2.21.a)$$

$$= u(x,t_0) - \delta t u \left.\frac{\partial u}{\partial x}\right|_{t_0} + O(\delta t^2) \quad (2.21.b)$$

$$= u(x,t_0) + \delta t U^2 K \cos(Kx) + O(\delta t^2) \quad (2.21.c)$$

$$= u(x,t_0) + \delta t U^2 \frac{K}{2} \sin(2Kx) + O(\delta t^2) \quad (2.21.d)$$

The non-linear term has therefore created a structure that is half the size. This phenomenon also occurs for the convective term of the Navier-Stokes equations.

2.2.2 Direct numerical simulation DNS

Direct numerical simulation solves the Navier-Stokes equations without making any approximations other than those due to numerical discretization (numerical error with respect to the solution of the partial differential equations). One must therefore use meshes that are fine enough to capture all turbulent structures y including the smallest ones. It is shown [72] that if L is the size of the full scale and λ the Kolmogorov scale, then $\frac{L}{\lambda}$ is in the order of $Re^{\frac{3}{4}}$, where Re is the Reynolds number based on the characteristic turbulent flow quantities. Thus, if we are interested in a flow in a characteristic size domain L, then the number of nodes N in each direction necessary to simulate phenomena of the Kolmogorov scale is proportional to $Re^{\frac{3}{4}}$. Thus, even for a low Reynolds number, $Re = 10^4$, a direct simulation requires 10^3 points in each direction, resulting in a total of one billion nodes! Flows in industrial configurations have Reynolds numbers based on the average flow of the order of 10^6 to 10^8 (which corresponds to a turbulent Reynolds number of the order of 10^4 to 10^6), it is therefore impossible and for a long time to perform DNS on industrial configurations despite the exponential progress of computing resources. It is therefore necessary to implement turbulence models that allow to model the smallest or all turbulent structures and no longer to simulate them by calculation.

2.2.3 Reynolds Averaged Navier-Stokes models RANS

RANS models predict only the mean portion of the flow with modeling for Reynolds tensor terms. All scales of turbulence are thus modeled, not simulated. This allows the use of much coarser meshes than in DNS because only the mean flow of the fluid needs to be predicted. However, as instantaneous values are not available, certain applications cannot be achieved with these turbulence models: the evaluation of thermal fatigue, the determination of

stress spectra of a fluid on a solid structure, etc. Among the most widely used RANS models in the industry are the $k-\varepsilon$, and the $k-\omega-SST$ which are first-order models (Reynolds stress modeling uses the Boussinesq hypothesis). Second-order models such as the $R_{ij}-\varepsilon$ or SSG predict each of the components of the Reynolds tensor which are then injected into the Navier-Stokes equations to predict the average velocity components.

2.2.3.1 k − ε model : [73,74]

The standard $k-\varepsilon$ model has two model equations, one for k and one for ε. We use k and ε to define velocity scale ϑ and length scale ℓ representative of the large-scale turbulence as follows [75]

$$\vartheta = k^{1/2} \tag{2.22}$$

$$\ell = \frac{k^{3/2}}{\varepsilon} \tag{2.23}$$

Applying the same approach as in the mixing length model we specify the eddy viscosity as follows

$$\mu_t = C\rho\vartheta\ell = \rho C_\mu \frac{k^2}{\varepsilon} \tag{2.24}$$

Where C_μ is a dimensionless constant.

The standard model uses the following transport equations used for k and ε :

In words the equations are

Rate of charge of k or ε	+	Transport of k or ε by convection	=	Transport of k or ε by diffusion	+	Rate of production of k or ε	-	Rate of destruction of k or ε

For turbulent kinetic energy k

$$\frac{\partial(\rho k)}{\partial t} + div(\rho k U) = div\left[\frac{\mu_t}{\sigma_k} grad\ k\right] + 2\mu_t E_{ij}E_{ij} - \rho\varepsilon \tag{2.25}$$

$$\frac{\partial(\rho k)}{\partial t} + \frac{\partial(\rho k u_i)}{\partial x_i} = \frac{\partial}{\partial x_j}\left[\frac{\mu_t}{\sigma_k}\frac{\partial k}{\partial x_j}\right] + 2\mu_t E_{ij}E_{ij} - \rho\varepsilon \tag{2.26}$$

For dissipation ε

$$\frac{\partial(\rho\varepsilon)}{\partial t} + div(\rho\varepsilon U) = div\left[\frac{\mu_t}{\sigma_\varepsilon} grad\ \varepsilon\right] + C_{1\varepsilon}\frac{\varepsilon}{k}2\mu_t E_{ij}E_{ij} - C_{2\varepsilon}\rho\frac{\varepsilon^2}{k} \quad (2.27)$$

$$\frac{\partial(\rho\varepsilon)}{\partial t} + \frac{\partial(\rho\varepsilon u_i)}{\partial x_i} = \frac{\partial}{\partial x_j}\left[\frac{\mu_t}{\sigma_\varepsilon}\frac{\partial\varepsilon}{\partial x_j}\right] + C_{1\varepsilon}\frac{\varepsilon}{k}2\mu_t E_{ij}E_{ij} - C_{2\varepsilon}\rho\frac{\varepsilon^2}{k} \quad (2.28)$$

where

u_i : represent velocity component in corresponding direction.

E_{ij} : represent the component of rate of deformation.

μ_t : represent eddy viscosity :

$$\mu_t = \rho C_\mu \frac{k^2}{\varepsilon} \quad (2.29)$$

The equations also consist of some adjustable constants. The values of these constants have been arrived at by numerous iterations of data fitting for a wide range of turbulent flows. These are as follows:

σ_k	σ_ε	$C_{1\varepsilon}$	$C_{2\varepsilon}$	C_μ
1.00	1.30	1.44	1.92	0.09

Table 2.1. The various closure coefficients appearing in the $k-\varepsilon$ model.

The $k-\varepsilon$ model has two main weaknesses: it over-predicts the shear stress in adverse pressure gradient flows because of too large length scale (due to too low dissipation) and it requires near-wall modification (i.e. low-Re number damping functions/terms).

2.2.3.2 k-omega Model :

The $k-\omega$ model is better than the $k-\omega$ model at predicting adverse pressure gradient flow and the standard $k-\omega$ model does not use any damping functions. However, the disadvantage of the standard $k-\omega$ model is that it is dependent on the free-stream value of ω.

2.2.3.2.1 k-omega Two-Equation Model (Wilcox1988) [76] :

k-omega Model has two model equations, one for k and one for ω as follows :

For turbulent kinetic energy k

$$\frac{\partial(\rho k)}{\partial t}+\frac{\partial\left(\rho k u_j\right)}{\partial x_j}=P-\beta^*\rho\omega k+\frac{\partial}{\partial x_j}\left[(\mu+\sigma_k\mu_t)\frac{\partial k}{\partial x_j}\right] \tag{2.30}$$

For Specific Dissipation Rate ω

$$\frac{\partial(\rho\omega)}{\partial t}+\frac{\partial\left(\rho\omega u_j\right)}{\partial x_j}=\frac{\gamma\omega}{k}P-\beta\rho\omega^2+\frac{\partial}{\partial x_j}\left[(\mu+\sigma_\omega\mu_t)\frac{\partial\omega}{\partial x_j}\right] \tag{2.31}$$

Where the turbulent eddy viscosity is computed from

$$\mu_t=\frac{\rho k}{\omega} \tag{2.32}$$

And

$$P=\tau_{ij}\frac{\partial u_i}{\partial x_j} \tag{2.33}$$

$$\tau_{ij}=\mu_t\left(2S_{ij}-\frac{2}{3}\frac{\partial u_k}{\partial x_k}\delta_{ij}\right)-\frac{2}{3}\rho k\delta_{ij} \tag{2.34}$$

$$S_{ij}=\frac{1}{2}\left(\frac{\partial u_i}{\partial x_j}+\frac{\partial u_j}{\partial x_i}\right) \tag{2.35}$$

The equations contains constants. These are as follows:

σ_k	σ_ω	β^*	β	γ
0.5	0.5	0.09	$\frac{3}{40}$	$\frac{5}{9}$

Table 2.2. The various closure coefficients appearing in the $k-\omega$ model.

2.2.3.2.2 Wilcox's modified k-omega model [77] :

For the same equations of turbulent kinetic energy k Eq (2.30) and Specific Dissipation Rate ω Eq (2.31) but the constants changes:

Where

$$\beta=\beta_0 f_\beta \tag{2.36}$$

With

$$f_\beta=\frac{1+70x_\omega}{1+80x_\omega} \tag{2.37}$$

$$x_\omega = \left|\frac{\Omega_{ij}\Omega_{jk}S_{ki}}{(\beta_0^*\omega)^3}\right| \tag{2.38}$$

And

$$\beta^* = \beta_0^* f_{\beta^*} \tag{2.39}$$

With

$$f_{\beta^*} = \begin{cases} 1, & x_k \le 0 \\ \dfrac{1+680x_k^2}{1+400x_k^2}, & x_k > 0 \end{cases} \qquad with\ x_k = \frac{1}{\omega^3}\frac{\partial k}{\partial x_j}\frac{\partial \omega}{\partial x_j} \tag{2.40}$$

σ_k	σ_ω	γ	β_0	β_0^*
0.5	0.5	$\frac{13}{25}$	$\frac{9}{125}$	0.09

Table 2.3. The various closure coefficients appearing in the modified $k-\omega$ model.

2.2.3.2.3 k-omega SST (Menter's Shear Stress Transport) turbulence model [78] :

The SST (Shear Stress Transport) model is an eddy-viscosity model which includes two main novelties:

– It is combination of a $k-\omega$ model (in the inner boundary layer) and k − ε model (in the outer region of the boundary layer as well as outside of it).

– A limitation of the shear stress in adverse pressure gradient regions.

Eq (2.30) and Eq (2.31) are multiplied by F_1 and Eq (2.26) and Eq (2.28) are multiplied by $(1-F_1)$, and the results equations of each set are added together to give the new model

$$\frac{\partial(\rho k)}{\partial t} + \frac{\partial(\rho k u_j)}{\partial x_j} = P - \beta^*\rho\omega k + \frac{\partial}{\partial x_j}\left[(\mu + \sigma_k\mu_t)\frac{\partial k}{\partial x_j}\right] \tag{2.41}$$

$$\frac{\partial(\rho\omega)}{\partial t} + \frac{\partial(\rho\omega u_j)}{\partial x_j} = \frac{\gamma\omega}{k}P - \beta\rho\omega^2 + \frac{\partial}{\partial x_j}\left[(\mu + \sigma_\omega\mu_t)\frac{\partial\omega}{\partial x_j}\right] + 2(1-F_1)\frac{\rho\sigma_{\omega_2}}{\omega}\frac{\partial k}{\partial x_j}\frac{\partial\omega}{\partial x_j} \tag{2.42}$$

Where

$$\mu_t = \frac{\rho\alpha_1 k}{max(\alpha_1\omega, \Omega F_2)} \qquad with\ \alpha_1 = 0.31 \tag{2.43}$$

Take ϕ represent any constant $(\sigma_k, \sigma_\omega \dots)$ in the new model, ϕ_1 for any constant in the $k-\omega$ model and ϕ_2 for any constant in the $k-\varepsilon$ model, the relation betweeen all this constants is

$$\phi = F_1\phi_1 + (1 - F_1)\phi_2 \tag{2.44}$$

For F_1

$$F_1 = \tanh(arg_1^4) \tag{2.45}$$

$$arg_1 = min\left[max\left(\frac{\sqrt{k}}{\beta^*\omega y}, \frac{500\nu}{y^2\omega}\right), \frac{4\rho\sigma_{\omega 2}k}{CD_{k\omega}y^2}\right] \tag{2.46}$$

$$CD_{k\omega} = max\left(2\rho\sigma_{\omega 2}\frac{1}{\omega}\frac{\partial k}{\partial x_j}\frac{\partial \omega}{\partial x_j}, 10^{-20}\right) \tag{2.47}$$

$$\nu = \frac{k}{\omega} \tag{2.48}$$

For F_2

$$F_2 = \tanh(arg_2^2) \tag{2.49}$$

$$arg_2 = max\left(2\frac{\sqrt{k}}{\beta^*\omega y}, \frac{500\nu}{y^2\omega}\right) \tag{2.50}$$

Where the costants of ϕ_1 are

σ_{k1}	$\sigma_{\omega 1}$	β_1	β^*	k	γ_1
0.5	0.5	0.075	0.09	0.41	$\frac{\beta_1}{\beta^*} - \frac{\sigma_{\omega 1}k^2}{\sqrt{\beta^*}}$

Table 2.4. The various costants appearing in ϕ_1.

And the costants of ϕ_2 are

σ_{k2}	$\sigma_{\omega 2}$	β_2	β^*	k	γ_2
1.0	0.856	0.0828	0.09	0.41	$\frac{\beta_2}{\beta^*} - \frac{\sigma_{\omega 2}k^2}{\sqrt{\beta^*}}$

Table 2.5. The various costants appearing in ϕ_1.

For the Far Field

$$\frac{U_\infty}{L} < \omega_{FarField} < 10\frac{U_\infty}{L} \tag{2.51}$$

$$\frac{10^{-5}U_\infty^2}{Re_L} < k_{FarField} < \frac{0.1U_\infty^2}{Re_L} \tag{2.52}$$

For the Far Field

$$\omega_{wall} = 10\frac{6\nu}{\beta_1(\Delta y_1)^2} \tag{2.53}$$

$$k_{wall} = 0 \tag{2.54}$$

The principal RANS models available are listed in the Table 2.6 [79]

Models	Advantages	Disadvantages
Spalart-Allmaras	Economical. Good for free flows, and profile flows without delamination or large pressure gradients.	Needs greater mesh resolution at the boundaries
standard $\boldsymbol{k-\varepsilon}$	Robust, economic and fairly reliable. Suitable for high Reynolds number flows.	Poor results for complex flows (strong pressure gradient, rotation and swirl).
RNG $\boldsymbol{k-\varepsilon}$	Guided by a rigorous statistical approach (Renormalization Group theory). Good for moderately complex flows (jet impact, flow separation, recirculation).	Limited by the isotropic turbulent viscosity theory.
Realizable $\boldsymbol{k-\varepsilon}$	Respects a physical constraint that can be violated by the $k-\varepsilon$ model . Offers the same advantages as RNG. Recommended in turbomachine applications.	Limited by the isotropic turbulent viscosity theory.
SST and Standard $\boldsymbol{k-\omega}$	Recommended model for turbomachinery problems (to be compared to Realizable $k-\varepsilon$). The version SST $k-\omega$ consists of a transition between the standard $k-\omega$ model (developed for moderate Reynolds numbers and boundary layers) and a high Re version of $k-\varepsilon$ when far from the walls.	Need higher resolution of the mesh at the borders
Reynolds-Stress Model (RSM)	The most physically complete model (transport and turbulence anisotropy are taken in consideration).	Requires more CPU time. The equations of momentum and turbulence transport are closely related.

Table 2.6. RANS type statistical turbulence models.

2.2.4 Large scale simulation LES

The Large Eddy Simulation (LES) approach is to simulate the largest scales of the turbulence, those that carry most of the turbulent kinetic energy, and to model the smaller

scales. It is therefore possible to use coarser meshes than in DNS, but still finer than for RANS models, bearing in mind that the smallest scales that can be resolved are of the order of the mesh size (more exactly twice the mesh size). Smaller scales, which are dissipative, are considered to be only minimally influenced by flow characteristics and are therefore isotropic and homogeneous. This makes it possible to build sub-grid models (i.e. those that take into account everything that happens at scales smaller than the grid) that are universal and therefore applicable to any flow. The LES thus makes it possible to deal with vibratory problems or thermal fatigue (unsteady problems).

2.2.5 RANS/LES coupling

The RANS/LES coupling consists in simulating part of the flow with a LES model while the rest of the domain uses a RANS model. This technique provides instantaneous information on a predefined area of the computational domain. On the other hand, a coarser mesh for the rest of the domain, where unsteady data is not required, can be used.

2.3 Numerical methode

2.3.1 Finite Volume Method (FVM) [80,81]

The method of finite volume is a special variant of the weighted residuals method in which the function of projection equals unity. This approach consists of subdividing the study area into elementary volumes such that each volume surrounds a major node P. Each volume is delimited by: two interfaces noted in the monodimensional case, four two-dimensional case interfaces (e, w, s, n) and six three-dimensional case interfaces (e, w, s, n, b). Each main node P is bounded in the one-dimensional case by neighboring nodes (E, W), (E, W, S, N) in the two-dimensional case, and (E, W, S, N, T, B) in the three-dimensional case. Any finite elementary volume embeds the differential equation. In order to calculate the integral in this elementary number, the unknown is defined by an approximation function between two consecutive nodes. In the field of study, then, the integral form is discrete. The discretization outcome provides an algebraic equation composed of the nodal values.

2.3.2 Finite Volume Method in the monodimensional Case

– Monodimensional Finite Volume Method Formulation of the Poisson Equation

In the monodimensional case the Poisson equation is written as follows

$$\frac{d}{dx}\left(\varepsilon\frac{d\phi}{dx}\right)+\rho=0 \qquad (2.55)$$

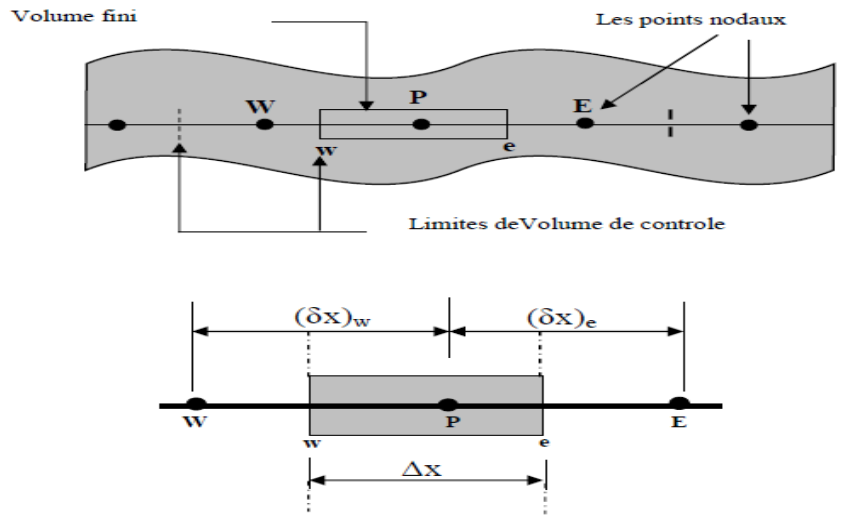

Figure 2.1. Discretization in finite volumes in the monodimensional case.

Equation (2.55) is integrated on the finite volume bounded by the faces (w,e)

$$\int_e^w \frac{d}{dx}\left(\varepsilon\frac{d\phi}{dx}\right)dx + \int_w^e \rho dx = 0 \tag{2.56}$$

After integration we'll have

$$\left(\varepsilon\frac{d\phi}{dx}\right)_e - \left(\varepsilon\frac{d\phi}{dx}\right)_w + \int_w^e \rho dx = 0 \tag{2.57}$$

A linear profile has been chosen to express the variation of the potential ϕ between neighbouring nodes

$$\left[\varepsilon_e\left(\frac{\phi_E - \phi_P}{(\delta x)_e}\right) - \varepsilon_w\left(\frac{\phi_P - \phi_W}{(\delta x)_w}\right)\right] + \rho_P \Delta x \tag{2.58}$$

such as

ϕ_P : Electrical potential at the node P.

ϕ_E : Electrical potential at the node E.

ϕ_W : Electrical potential at the node W.

$(\delta x)_e$: Distance between the nodes P and E.

$(\delta x)_w$: Distance between the nodes W and P.

Δx : Length of finite volume.

The final algebraic equation is written in the form

$$a_P\phi_P = a_E\phi_E + a_W\phi_W + S \tag{2.59}$$

With

$$a_E = \frac{\varepsilon_e}{(\delta x)_e} \tag{2.60}$$

$$a_W = \frac{\varepsilon_w}{(\delta x)_w} \tag{2.61}$$

$$a_P = a_E + a_W \tag{2.62}$$

$$\text{source term } S = \rho_P \Delta x \tag{2.63}$$

In the case of a uniform mesh size

$$\Delta x = (\delta x)_e = (\delta x)_w \tag{2.64}$$

And

$$a_E = \frac{\varepsilon_e}{\Delta x} \tag{2.65}$$

$$a_W = \frac{\varepsilon_w}{\Delta x} \tag{2.66}$$

$$a_P = a_E + a_W \tag{2.67}$$

Then we get an algebraic equation that links each principal node "P" to the neighboring nodes "E" and "W". If the discretization of the domain has N nodes, we are led to solve a system of N equations with N unknown. The resulting system will be solved by numerical methods of resolution.

2.3.3 Finite Volume Method in the bidimensional Case

The bidimensional formulation consists of subdividing the field of study (Ω) into a number of finite elements. Each element contains four nodes. A finite volume surrounds each node.

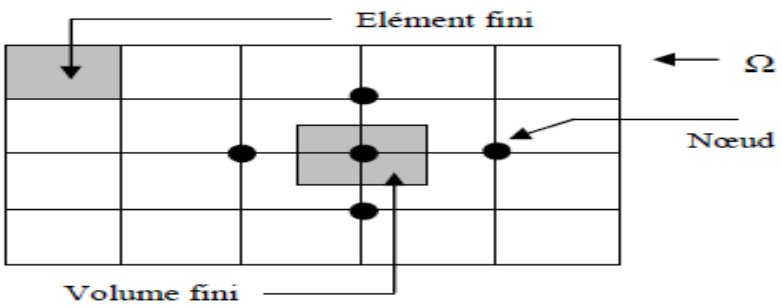

Figure 2.2. Discretization in finite volumes in the bidimensional case.

The main node "P" is surrounded by four neighboring nodes "N", "S", "W" and "E". The points (e, w, n, s).

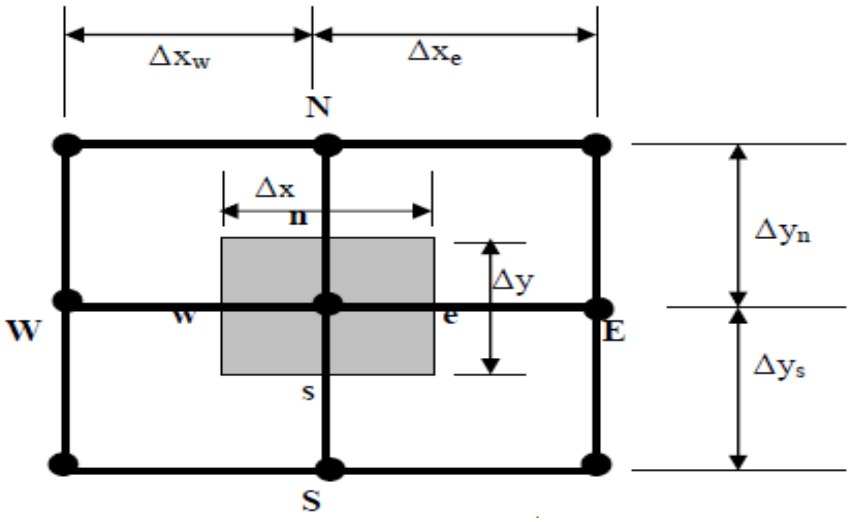

Figure 2.3. Bidimensional description of a finite volume.

The Poisson equation in the bidimensional case is

$$\frac{\partial}{\partial x}\left(\varepsilon\frac{\partial\phi}{\partial x}\right)+\frac{\partial}{\partial y}\left(\varepsilon\frac{\partial\phi}{\partial y}\right)=-\rho \tag{2.68}$$

This equation is projected on a projection function equal to unity. It is then integrated on the finite volume corresponding to the node P, we obtain

$$\int_w^e\int_s^n\frac{\partial}{\partial x}\left(\varepsilon\frac{\partial\phi}{\partial x}\right)dxdy+\int_w^e\int_s^n\frac{\partial}{\partial y}\left(\varepsilon\frac{\partial\phi}{\partial y}\right)dxdy=\int_w^e\int_s^n-\rho dxdy \tag{2.69}$$

So

$$\int_w^e\int_s^n\frac{\partial}{\partial x}\left(\varepsilon\frac{\partial\phi}{\partial x}\right)dxdy+\int_w^e\int_s^n\frac{\partial}{\partial y}\left(\varepsilon\frac{\partial\phi}{\partial y}\right)dxdy=\left[\left(\varepsilon\frac{\partial\phi}{\partial x}\right)_e-\left(\varepsilon\frac{\partial\phi}{\partial x}\right)_w\right]\Delta y+\left[\left(\varepsilon\frac{\partial\phi}{\partial y}\right)_n-\left(\varepsilon\frac{\partial\phi}{\partial y}\right)_s\right]\Delta x \tag{2.70}$$

And

$$\int_w^e\int_s^n-\rho dxdy=\rho_P\,\Delta x\Delta y \tag{2.71}$$

A linear profile was chosen to express the potential variation ϕ between neighbouring nodes. The result is only the nodal values.

$$\left(\varepsilon\frac{\partial\phi}{\partial x}\right)_e = \varepsilon\left(\frac{\phi_E - \phi_P}{\Delta x_e}\right) \tag{2.72}$$

$$\left(\varepsilon\frac{\partial\phi}{\partial x}\right)_w = \varepsilon\left(\frac{\phi_P - \phi_W}{\Delta x_w}\right) \tag{2.73}$$

$$\left(\varepsilon\frac{\partial\phi}{\partial x}\right)_n = \varepsilon\left(\frac{\phi_N - \phi_P}{\Delta y_n}\right) \tag{2.74}$$

$$\left(\varepsilon\frac{\partial\phi}{\partial x}\right)_s = \varepsilon\left(\frac{\phi_P - \phi_S}{\Delta y_s}\right) \tag{2.75}$$

The final algebraic equation is written in the form

$$a_P\phi_P = a_E\phi_E + a_W\phi_W + a_N\phi_N + a_S\phi_S + S \tag{2.76}$$

With

$$a_E = \varepsilon_e\frac{\Delta y}{\Delta x_{\mathrm{e}}} \tag{2.77}$$

$$a_W = \varepsilon_w\frac{\Delta y}{\Delta x_{\mathrm{w}}} \tag{2.78}$$

$$a_N = \varepsilon_n\frac{\Delta x}{\Delta y_{\mathrm{n}}} \tag{2.79}$$

$$a_S = \varepsilon_s\frac{\Delta x}{\Delta y_{\mathrm{s}}} \tag{2.80}$$

$$a_P = a_E + a_W + a_N + a_S \tag{2.81}$$

$$S = \rho_P\Delta x\Delta y \tag{2.82}$$

The result obtained represents an algebraic equation linking the unknown at the main node "P" to the unknowns at the neighbouring nodes "W", "E", "S" and "N".

2.3.4 Jacobi and Gauss-Seidel Iterative Methods

2.3.4.1 Jacobi Method

Two assumptions made on Jacobi Method:

a. The system given by

$$\begin{aligned} a_{11}x_1 + a_{12}x_2 + \cdots a_{1n}x_n &= b_1 \\ a_{21}x_1 + a_{22}x_2 + \cdots a_{2n}x_n &= b_2 \\ &\vdots \\ a_{n1}x_1 + a_{n2}x_2 + \cdots a_{nn}x_n &= b_n \end{aligned}$$

Has a unique solution.

b. The coefficient matrix A has no zeros on its main diagonal, namely, $a_{11}, a_{22}, \dots, a_{nn}$ are nonzeros.

2.3.4.1.1 Main idea of Jacobi

To begin, solve the 1st equation for x_1, the 2nd equation for x_2 and so on to obtain the rewritten equations

$$x_1 = \frac{1}{a_{11}}(b_1 - a_{12}x_2 - a_{13}x_3 - \cdots a_{1n}x_n)$$
$$x_2 = \frac{1}{a_{22}}(b_2 - a_{21}x_1 - a_{23}x_3 - \cdots a_{2n}x_n)$$
$$\vdots$$
$$x_n = \frac{1}{a_{nn}}(b_n - a_{n1}x_1 - a_{n2}x_2 - \cdots a_{n,n-1}x_{n-1})$$

Then make an initial guess of the solution

$$x^{(0)} = \left(x_1^{(0)}, x_2^{(0)}, x_3^{(0)}, \dots\ x_n^{(0)}\right) \tag{2.83}$$

Substitute these values into the right hand side the of the rewritten equations to obtain the first approximation, $\left(\mathrm{x}_1^{(1)}, \mathrm{x}_2^{(1)}, \mathrm{x}_3^{(1)}, \dots\ \mathrm{x}_\mathrm{n}^{(1)}\right)$. This accomplished one iteration.

In the same way, the second approximation $\left(x_1^{(2)}, x_2^{(2)}, x_3^{(2)}, \dots\ x_n^{(2)}\right)$ is computed by substituting the first approximation's value $\left(x_1^{(1)}, x_2^{(1)}, x_3^{(1)}, \dots\ x_n^{(1)}\right)$ into the right hand side of the rewritten equations. By repeated iterations, we form a sequence of approximations $x^{(k)} = \left(x_1^{(k)}, x_2^{(k)}, x_3^{(k)}, \dots\ x_n^{(k)}\right)^t$, $k = 1,2,3, \dots$

2.3.4.1.2 Jacobi methode

For each $k \geq 1$, generate the components $x_i^{(k)}$ of $x^{(k)}$ from $x^{(k-1)}$ by

$$x_i^{(k)} = \frac{1}{a_{ii}}\left[\sum_{\substack{j=1, \\ j\neq i}}^{n}\left(-a_{ij}x_j^{(k-1)}\right) + b_i\right], \qquad \text{for } i = 1,2,, \dots n \tag{2.84}$$

Stopping when

$$\frac{\left\|x^{(k)} - x^{(k-1)}\right\|}{\|x^{(k)}\|} < \varepsilon \quad or \quad \left\|x^{(k)} - x^{(k-1)}\right\| < \varepsilon \tag{2.85}$$

Here ε is a given small number.

Another stopping criterion :

$$\frac{\left\|x^{(k)} - x^{(k-1)}\right\|}{\|x^{(k)}\|} \tag{2.86}$$

– A vector norm on R^n is a function $\|\cdot\|$, from R^n to R with the properties :

(i) $\|x\| \geq 0$ for all $x \in R^n$

(ii) $\|x\| = 0$ if and only if $x = 0$

(iii) $\|\alpha x\| = |\alpha|\|x\|$ for all $\alpha \in R$ and $x \in R^n$

(iv) $\|x + y\| \leq \|x\| + \|y\|$ for all $x, y \in R^n$

– The Euclidean norm l_2 and the infinity norm l_∞ for the vector $x = [x_1, x_2, \ldots, x_n]^t$ are defined by :

$$\|x\|_2 = \left\{\sum_{i=1}^{n} x_i^2\right\}^{\frac{1}{2}} \tag{2.87}$$

And

$$\|x\|_\infty = \max_{1 \leq i \leq n} |x_i| \tag{2.88}$$

2.3.4.1.3 Jacobi method in Matrix form

Consider to solve an $n \times n$ size system of linear equations $Ax = b$ with

$$A = \begin{bmatrix} a_{11} & a_{12} & \cdots & a_{1n} \\ a_{21} & a_{22} & \cdots & a_{2n} \\ \vdots & \vdots & \ddots & \vdots \\ a_{n1} & a_{n2} & \cdots & a_{nn} \end{bmatrix} \quad and \quad b = \begin{bmatrix} b_1 \\ b_2 \\ \vdots \\ b_n \end{bmatrix} \quad for\ x = \begin{bmatrix} x_1 \\ x_2 \\ \vdots \\ x_n \end{bmatrix}$$

We split A into

$$A = \begin{bmatrix} a_{11} & 0 & \cdots & 0 \\ 0 & a_{22} & \cdots & 0 \\ \vdots & \vdots & \ddots & \vdots \\ 0 & 0 & \cdots & a_{nn} \end{bmatrix} - \begin{bmatrix} 0 & \cdots & 0 & 0 \\ -a_{21} & \cdots & 0 & 0 \\ \vdots & \vdots & \ddots & \vdots \\ -a_{n1} & \ldots & -a_{n,n-1} & 0 \end{bmatrix} - \begin{bmatrix} 0 & -a_{12} & \cdots & -a_{1n} \\ 0 & 0 & \cdots & \vdots \\ \vdots & \vdots & \ddots & -a_{n-1,n} \\ 0 & 0 & \cdots & 0 \end{bmatrix} = D - L - U$$

Where

$$D = \begin{bmatrix} a_{11} & 0 & \cdots & 0 \\ 0 & a_{22} & \cdots & 0 \\ \vdots & \vdots & \ddots & \vdots \\ 0 & 0 & \cdots & a_{nn} \end{bmatrix}, L = \begin{bmatrix} 0 & \cdots & 0 & 0 \\ -a_{21} & \cdots & 0 & 0 \\ \vdots & \vdots & \ddots & \vdots \\ -a_{n1} & \ldots & -a_{n,n-1} & 0 \end{bmatrix}, U = \begin{bmatrix} 0 & -a_{12} & \cdots & -a_{1n} \\ 0 & 0 & \cdots & \vdots \\ \vdots & \vdots & \ddots & -a_{n-1,n} \\ 0 & 0 & \cdots & 0 \end{bmatrix}$$

$Ax = b$ is transformed into

$$(D - L - U)x = b \tag{2.89.a}$$

$$Dx = (L + U)x + b \tag{2.89.b}$$

Assume D^{-1} exists and

$$D^{-1} = \begin{bmatrix} \frac{1}{a_{11}} & 0 & \dots & 0 \\ 0 & \frac{1}{a_{22}} & \dots & 0 \\ \vdots & \vdots & \ddots & \vdots \\ 0 & 0 & \dots & \frac{1}{a_{nn}} \end{bmatrix}$$

Then

$$x = D^{-1}(L + U)x + D^{-1}b \tag{2.90}$$

The matrix form of Jacobi iterative methode is :

$$x^{(k)} = D^{-1}(L + U)x^{(k-1)} + D^{-1}b, \qquad k = 1,2,3, \dots \tag{2.91}$$

Define

$$T_j = D^{-1}(L + U) \tag{2.92}$$

And

$$c = D^{-1}b \tag{2.93}$$

Jacobi iteration method can also be written as

$$x^{(k)} = T_j x^{(k-1)} + c, \qquad k = 1,2,3, \dots \tag{2.94}$$

2.3.4.2 Gauss-Seidel Method

2.3.4.2.1 Main idea of Gauss-Seidel

With the Jocobi method, only the values of $x_i^{(k)}$ obtained in the k iteration are used to compute $x_i^{(k+1)}$. With the Gauss-Seidel method, we use the new values $x_i^{(k+1)}$ as soon as they are known. For exemple, once we have computed $x_1^{(k+1)}$ from the first equation, its value is then used in the second equation to obtain the new $x_2^{(k+1)}$, and so on.

2.3.4.2.2 Gauss-Seidel Method

For each $k \geq 1$, generate the components $x_i^{(k)}$ of $x^{(k)}$ from $x^{(k-1)}$ by

$$x_i^{(k)} = \frac{1}{a_{ii}}\left[-\sum_{j=1}^{i-1}\left(a_{ij}x_j^{(k)}\right) + \sum_{j=i+1}^{n}\left(a_{ij}x_j^{(k-1)}\right) + b_i\right] \qquad for\ i = 1,2,,\dots n \qquad (2.95)$$

Namely,

$$a_{11}x_1^{(k)} = -a_{12}x_2^{(k-1)} - \cdots - a_{1n}x_n^{(k-1)} + b_1$$

$$a_{22}x_2^{(k)} = -a_{21}x_1^{(k)} - a_{23}x_3^{(k-1)} - \cdots - a_{2n}x_n^{(k-1)} + b_2$$

$$a_{33}x_3^{(k)} = -a_{31}x_1^{(k)} - a_{32}x_2^{(k)} - a_{34}x_4^{(k-1)} - \cdots - a_{3n}x_n^{(k-1)} + b_3$$

$$\vdots$$

$$a_{nn}x_n^{(k)} = -a_{n1}x_1^{(k)} - a_{n2}x_2^{(k)} - \cdots - a_{n,n-1}x_{n-1}^{(k)} + b_n$$

2.3.4.2.3 Gauss-Seidel Method in Matrix form

$$(D - L)x^{(k)} = Ux^{(k-1)} + b \qquad (2.96.a)$$

$$x^{(k)} = (D - L)^{-1}Ux^{(k-1)} + (D - L)^{-1}b \qquad (2.96.b)$$

Define

$$T_g = (D - L)^{-1}U \qquad (2.97)$$

And

$$c_g = (D - L)^{-1}b \qquad (2.98)$$

Gauss-Seidel method can be written as

$$x^{(k)} = T_g x^{(k-1)} + c_g \qquad \text{for each} \quad k = 1,2,3,\dots \qquad (2.99)$$

2.3.5 Convergence theorems of the iteration methods

Let the iteration method be written as

$$x^{(k)} = Tx^{(k-1)} + c \qquad \text{for each} \quad k = 1,2,3,\dots \qquad (2.100)$$

a) The spectral radius $\rho(A)$ of a matrix A is defined by

$$\rho(A) = \max|\lambda| \tag{2.101}$$

Where λ is an eigenvalue of A.

Remark : For complex $\lambda = a + bj$, we define $|\lambda| = \sqrt{a^2 + b^2}$.

b) If the spectral radius satisfies $\rho(T) < 1$, then $(I + T)^{-1}$ exists, and

$$(I + T)^{-1} = I + T + T^2 + \cdots = \sum_{j=0}^{\infty} T^j \tag{2.102}$$

c) For any $x^{(0)} \in R^n$, the sequence $\{x^{(k)}\}_{k=0}^{\infty}$ defined by

$$x^{(k)} = Tx^{(k-1)} + c \qquad \text{for each} \quad k \geq 1 \tag{2.103}$$

Converges to the unique solution of $x = Tx + c$ if and only if $\rho(T) < 1$.

Proof (only show $\rho(T) < 1$ is sufficient condition)

$$x^{(k)} = Tx^{(k-1)} + c = T\left(Tx^{(k-2)} + c\right) + c = \cdots = T^k x^{(0)} + (T^{K-1} + \cdots + T + I)C \tag{2.104}$$

Since $\rho(T) < 1$:

$$\lim_{k\to\infty} T^k x^{(0)} = 0 \tag{2.105}$$

$$\lim_{k\to\infty} x^{(k)} = 0 + \lim_{k\to\infty} \left(\sum_{j=0}^{k-1} T^j \right) c = (I + T)^{-1} c \tag{2.106}$$

d) A matrix norm $\|\cdot\|$ on $n \times n$ matrices is a real-valued function satisfying

(i) $\|A\| \geq 0$

(ii) $\|A\| = 0$ if and only if $A = 0$

(iii) $\|\alpha A\| = |\alpha|\|A\|$

(iv) $\|A + B\| \leq \|A\| + \|B\|$

(v) $\|AB\| \leq \|A\|\|B\|$

e) If $\|\cdot\|$ is a vector norm, the induced (or natural) matrix norm is given by :

$$\|A\| = \max_{\|x\|=1} \|Ax\| \tag{2.107}$$

f) If $A = [a_{ij}]$ is an $n \times n$ matrices, then :

$$\|A\|_\infty = \max_{1 \le i \le n} \sum_{j=1}^{n} |a_{ij}| \tag{2.108}$$

g) If $\|T\| < 1$ for any natural matrix norm and c is a given vector, then the sequence $\{x^{(k)}\}_{k=0}^{\infty}$ defined by :

$x^{(k)} = Tx^{(k-1)} + c$ converges, for any $x^{(0)} \in R^n$, to a vector $x \in R^n$, with $x = Tx + c$, and the following error bound hold :

(i) $\|x - x^{(k)}\| \le \|T\|^k \|x^{(0)} - x\|$

(ii) $\|x - x^{(k)}\| \le \frac{\|T\|^k}{1-\|T\|} \|x^{(1)} - x^{(0)}\|$

h) If A is strictly diagonally dominant, then for any choice of $x^{(0)}$, both the Jacobi and Gauss-Seidel methods give sequences $\{x^{(k)}\}_{k=0}^{\infty}$ that converges to the unique solution of $Ax = b$.

2.3.6 Rate of Convergence

a) Imply $\|x - x^{(k)}\| \approx \rho(T)^k \|x^{(0)} - x\|$

b) Theorem of Stein-Rosenberg : If $a_{ij} \le 0$, for each $i \ne j$ and $a_{ii} \ge 0$, for each $i = 1,2, \dots, n$, the one and only one of following statements holds:

(i) $0 \le \rho(T_g) < \rho(T_j) < 1$;

(ii) $1 < \rho(T_j) < \rho(T_g)$;

(iii) $\rho(T_j) = \rho(T_g) = 0$;

(iv) $\rho(T_j) = \rho(T_g) = 1$.

Section 3

Results and Discussion :

Part 1

3.1 Introduction

In the third section, we present the mathematical model and initial conditions with validation, and we finish with first part of the simulations where we interest on the passive modifications like change of form of cases (heated wall) the form of the orifice and number of cavities; we also fend the validation as well as the analysis of the results obtained by the simulation of the different modified cases.

3.2 Mathematical model and validation

The governing standard incompressible Navier-Stokes equations were solved:

$$(\nabla . \vec{v}) = 0 \tag{3.1}$$

$$\frac{D\vec{v}}{Dt} = -\frac{1}{\rho}\nabla P + v\Delta\vec{v} \tag{3.2}$$

$$\rho c \frac{DT}{Dt} = \varphi_v + \nabla . (k\Delta T) \tag{3.3}$$

The spatially averaged instantaneous Nusselt number is computed at every time step as:

$$Nu(t) = \frac{q''}{\overline{T_w}(t) - T_b(t)} \frac{H}{k} \tag{3.4}$$

Where T_b is the bulk flow temperature, computed with a mass-weighted average approach and $\overline{T_W}$ is the spatially averaged wall temperature in the location of the heat source. H is the width of the cross-flow channel.

3.2.1 Initial conditions and solving methodology

In this Part we are considering the first configuration like a basic configuration without any modification as shown in Figure 3.1, this configuration was presented by Chandratilleke et al [82]. All the Parametric range for the numerical simulations, thermal properties of the working fluid and conditions of simulation are presented respectively in Table 3.1, Table 3.2, Table 3.3 and Table 3.4

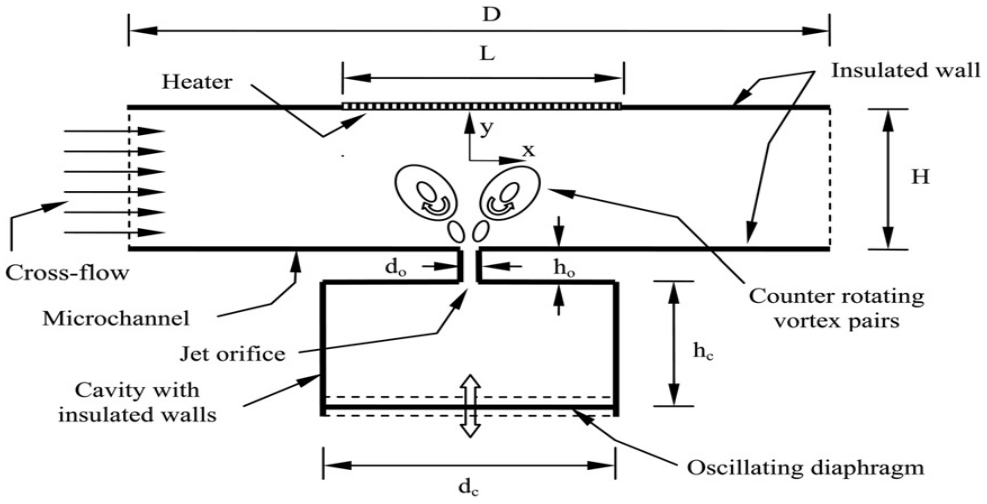

Figure 3.1. Basic case with synthetic jet cross a micro-channel.[82]

Parameter	**Range**
h_0 (μm)	50
H (μm)	500
D (μm)	2250
L (μm)	750
d_c (μm)	750
h_c (μm)	500
d_0 (μm)	50

Table 3.1. Dimensions of the boundary conditions.

Parameter	**Range**
Micro-channel inlet velocity, V_i (m/s)	1
Diaphragm frequency, *f* (kHz)	10
Diaphragm amplitude, A (μm)	25-50-75
Jet Reynolds number, Re_c	≈5-20
Distance from orifice to heated wall, H/d_0	10
T_∞ (K)	300
q'' (W/m^2)	15000
ω	$2\pi f$
φ	$\pi/2$

Table 3.2. Parametric range for the numerical simulations.

The flowing fluid (air) is supposed to be incompressible, and its properties at a temperature T =300 K are presented in Table 3.2. Figure 3.2 shows the different applied boundary condition at the borders of the considered geometry.

Property	**Hypothesis**	**Value**
density	Ideal gas	1.1614
Specific heat	Constant	1.007
viscosity	Constant	1.7894 e-5
Thermal conductivity	Constant	0.0263

Table 3.3. Thermal properties of the working fluid.

Wall heat flux	15 KW/m^2
Time	Transient
Model Energy	On
Model viscous	SST k-ω
Number of time steps	720

Table 3.4. Limit Conditions.

The oscillatory motion of the membrane is modeled by a similar movement to that of a piston by using the dynamic mesh ANSYS FLUENT, a user-defined function (UDF) written in C and incorporating the technique of dynamic-layering (Rizzetta et al, 1999) [83]. The initial position of the diaphragm (when t=0) is taken at the bottom of the cavity. The function of displacement of the diaphragm is expressed as follows:

$$y = A \sin(\omega t - \varphi) \tag{5}$$

Where y is the iris position (y = 0 corresponds to the maximum volume of the cavity and $y = A$ is the minimum volume of the cavity), A is the amplitude of the diaphragm, ω is the angular velocity ($\omega = 2\pi f$), f is the frequency of operation, the angular phase shift is φ which allows the membrane to start its movement from the bottom of the cavity.

The initial solution before starting the unsteady numerical simulations is considered as the velocity and temperature field across the channel without synthetic jet. At each time step of the cycle, the internal iterations continued until the residual mass, momentum and turbulence parameters (k and ω) were reduced blow 10^{-3} and 10^{-6} for the residual of energy.

The numerical model is validated by comparing present numerical results with the

results of Chandratilleke et al [82]. The comparison for the variation of the local Nusselt number versus the normalized distance at velocity inlet of *Vi* =1 m/s is shown in Figure 3.2 and is in reasonably good agreement with Chandratilleke et al. [82] results.

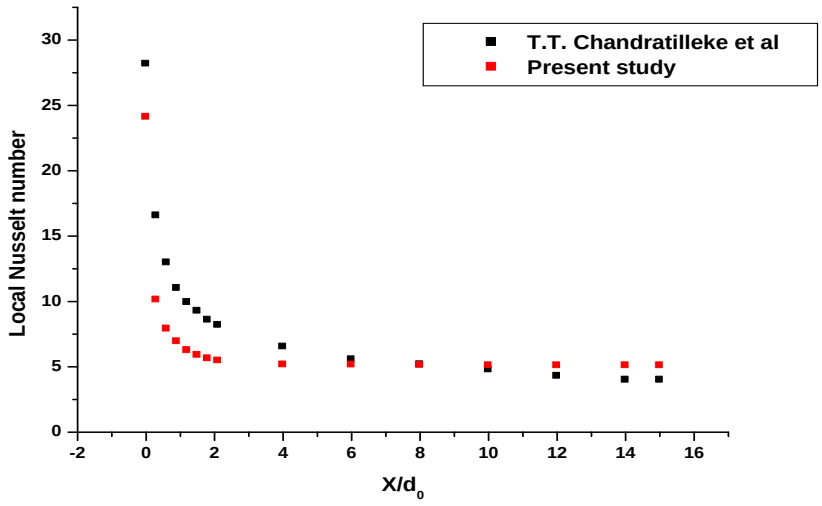

Figure 3.2. Comparison of the present results with those of Chandratilleke et al. [82] for the variation of the Local Nusselt number versus normalized distance for *Vi* = 1 m/s.

3.3 Compare results of each undulation heated wall at deferent amplitudes:

This configuration was similar to the basic case but with converged form of orifice and undulation heated wall ‘’modified case’’ Figures 3.3 and 3.4, I used as follows, 3 different degrees of undulation heated wall: 10, 12.5 and 20 µm, and all the configurations tested for oscillating amplitudes A = 25, 50 and 75 µm while the inlet velocity V_i = 1 m/s.

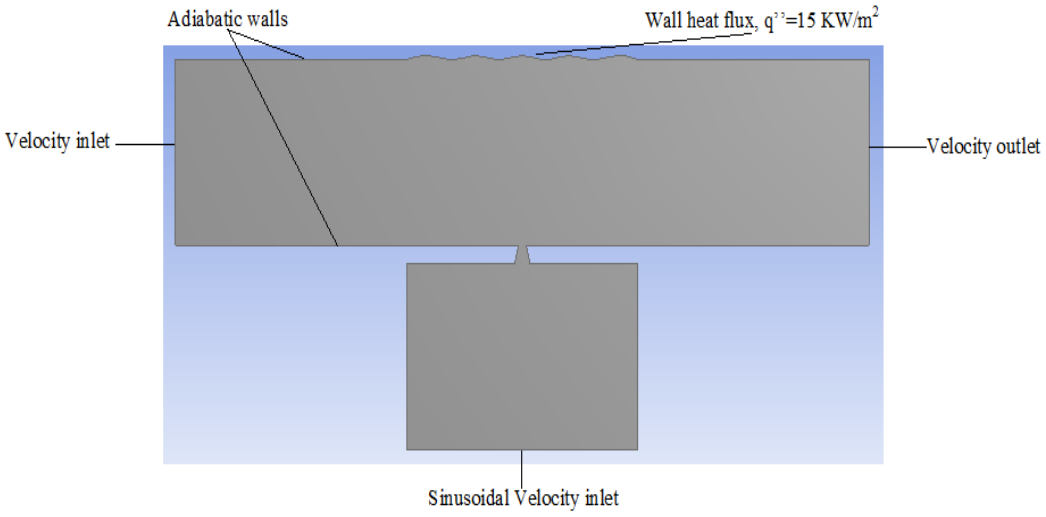

Figure 3.3. Representation of boundary conditions 1.

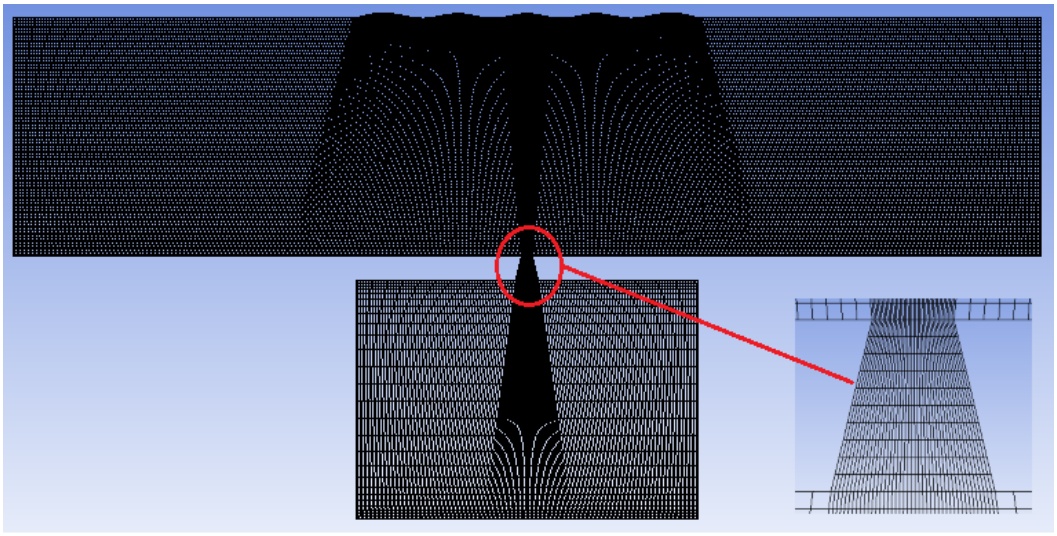

Figure 3.4. Computational grid 1.

Results and discussion

Results are presented in Figure 3.5 shows the Comparison of Nusselt number between Basic case and Modified case at different undulation heated wall 10, 12.5, 20 µm, and A = 75 µm while the inlet velocity V_i = 1 m/s. The wavy form of the heated wall gives a large heat transfer surface then the normal form for that the local nusselt number is higher in modified case exactly at the undulation heated wall of 10 µm.

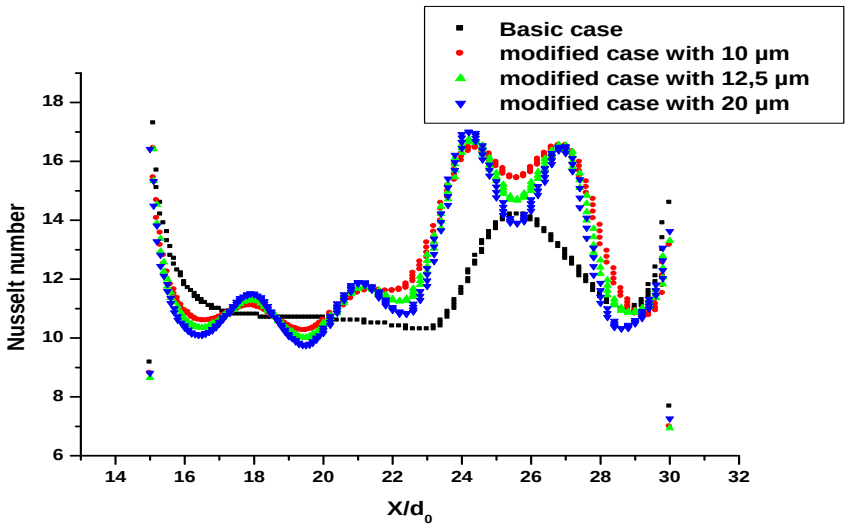

Figure 3.5. Comparison of Nusselt number for the heated surface between Basic case and Modified case at different undulation heated wall 10, 12.5, 20 µm, and A = 75 µm while the inlet velocity V_i = 1 m/s.

Figure 3.6 (a) for Basic configuration case, and Figure 3.6 (b) for the configuration with converged form of orifice and 10 µm of undulation heated wall. For different operating conditions are considered in both of them, namely the different oscillating amplitudes A = 25, 50 and 75 µm while the inlet velocity V_i = 1 m/s. The augmentation rate for further values of the oscillating amplitude falls and the Nusselt number values obtained for amplitude A = 75 µm with converged form of orifice and 10 µm of undulation heated wall are much higher than the other oscillations and for the basic case.

(a)

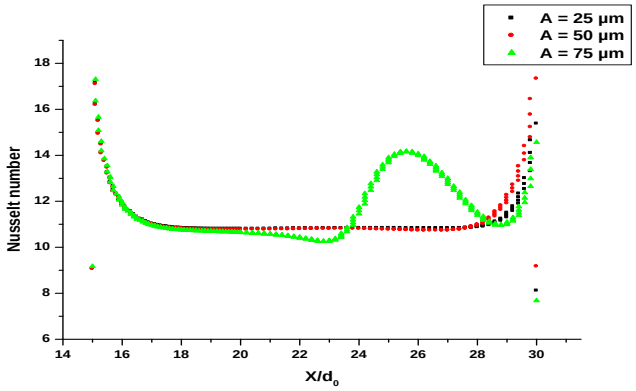

(b)

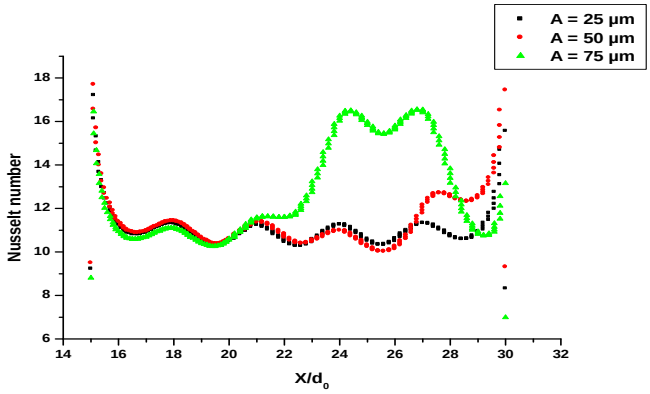

Figure 3.6. Nusselt number on the heated surface for different amplitudes, (a) Basic case, (b) Modified case with undulation heated wall of 10 µm.

A further analysis can be performed with the time mean values of the Nusselt number. The resulting quantities are represented in Figure 3.7, the tendency reported above for the converged form of orifice and 10 µm of undulation heated wall.

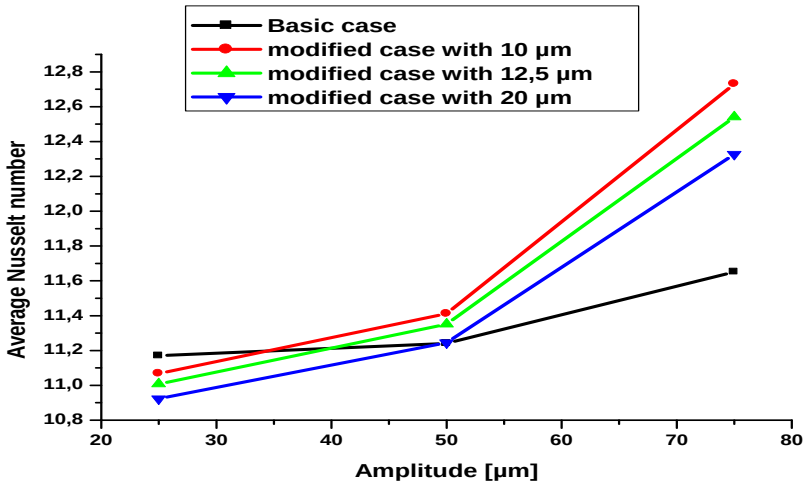

Figure 3.7. Average Nusselt Number for Basic case and Modified case at different undulation heated wall 10, 12.5, 20 µm, for the three amplitudes A = 25, 50 and 75 µm and V_i = 1 m/s.

The temperature field in the smooth channel depicted in Figure 3.8 at the end of an oscillating cycle, for the basic case (a) and for the configuration with converged form of orifice and 10 µm of undulation heated wall (b). The contours clearly show the temperature rise in the vicinity of the heated surface, the process of generating the jet vortex creates a highly conductive heat flow structure at the heated surface.

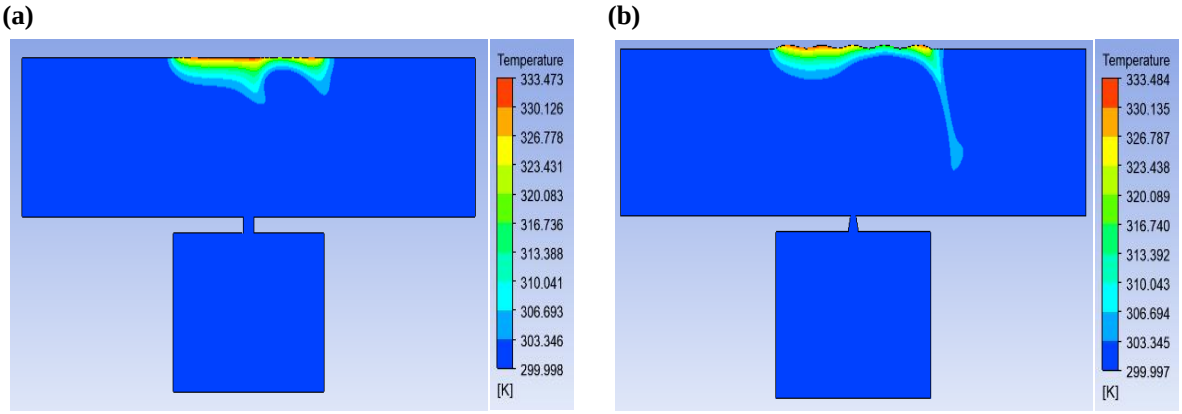

Figure 3.8. Contour plots of the static Temperature after one cycle for V_i = 1 m/s and A = 75 µm, (a) Basic case, (b) Modified case with undulation heated wall of 10 µm.

Figure 3.9 shows the contours of velocity inside the basic case and modified case for the three difference undulation degrees of heated wall with converged form of orifice. The results correspond to a transverse flow velocity V_i = 1 m/s and a jet amplitude A = 75 µm.

The form of orifice helps the injection of fluid with high speed and creates a turbulent flow in the heat transfer region, the results a good heat exchange and high cooling. These measurements are illustrated in more detail in Figure 3.10 for one cycle (page 58).

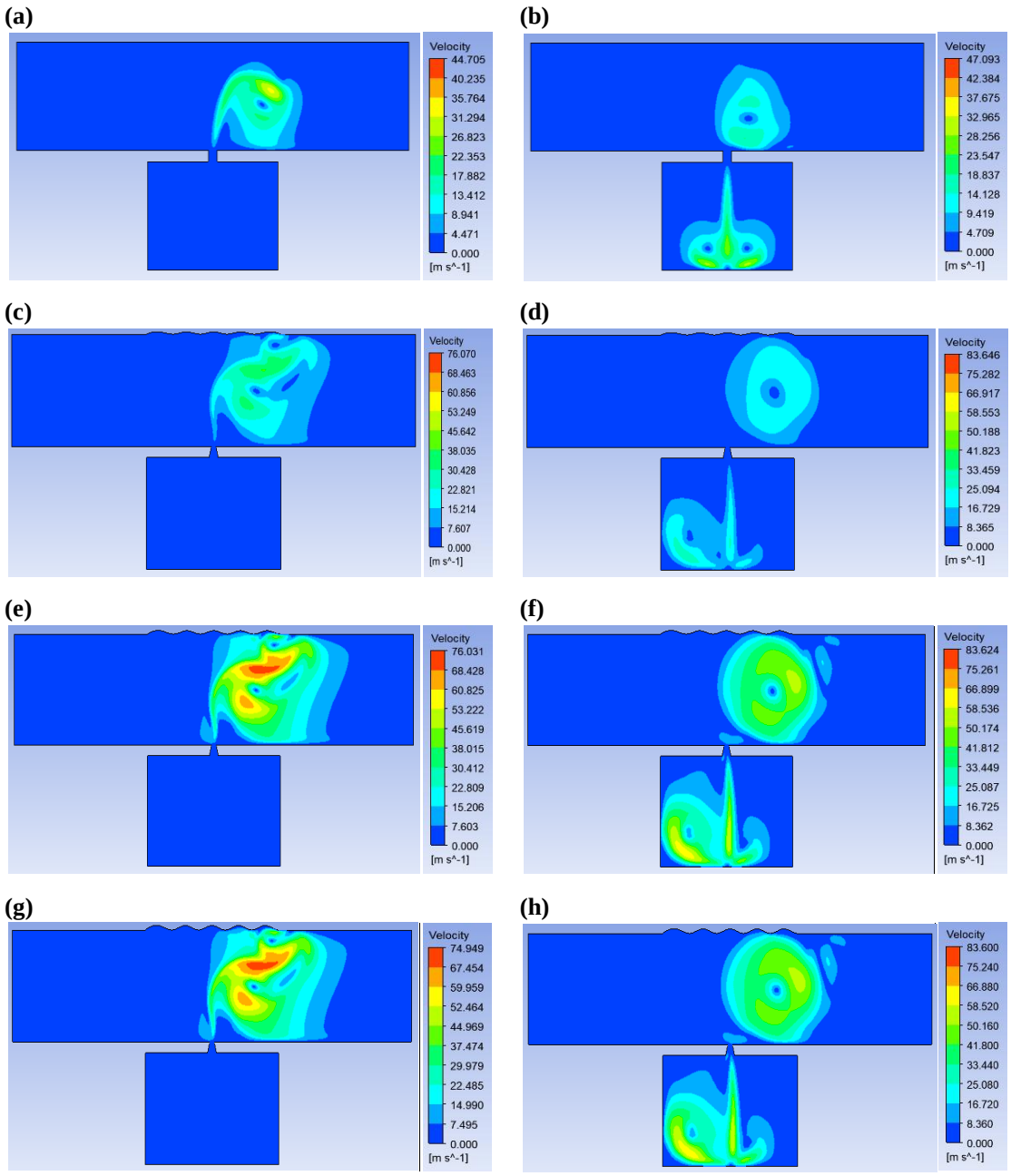

Figure 3.9. Contour plots of the magnitude velocity for four cases [(a) t=T/2 and (b) t=T for the Basic case, (c) t=T/2 and (d) t=T for the Modified case with 10 µm of undulation heated wall, (e) t=T/2 and (f) t=T for Modified case with 12,5 µm of undulation heated wall, (g) t=T/2 and (h) t=T for the Modified case with 25 µm of undulation heated wall]; for V_i = 1 m/s; A = 75 µm.

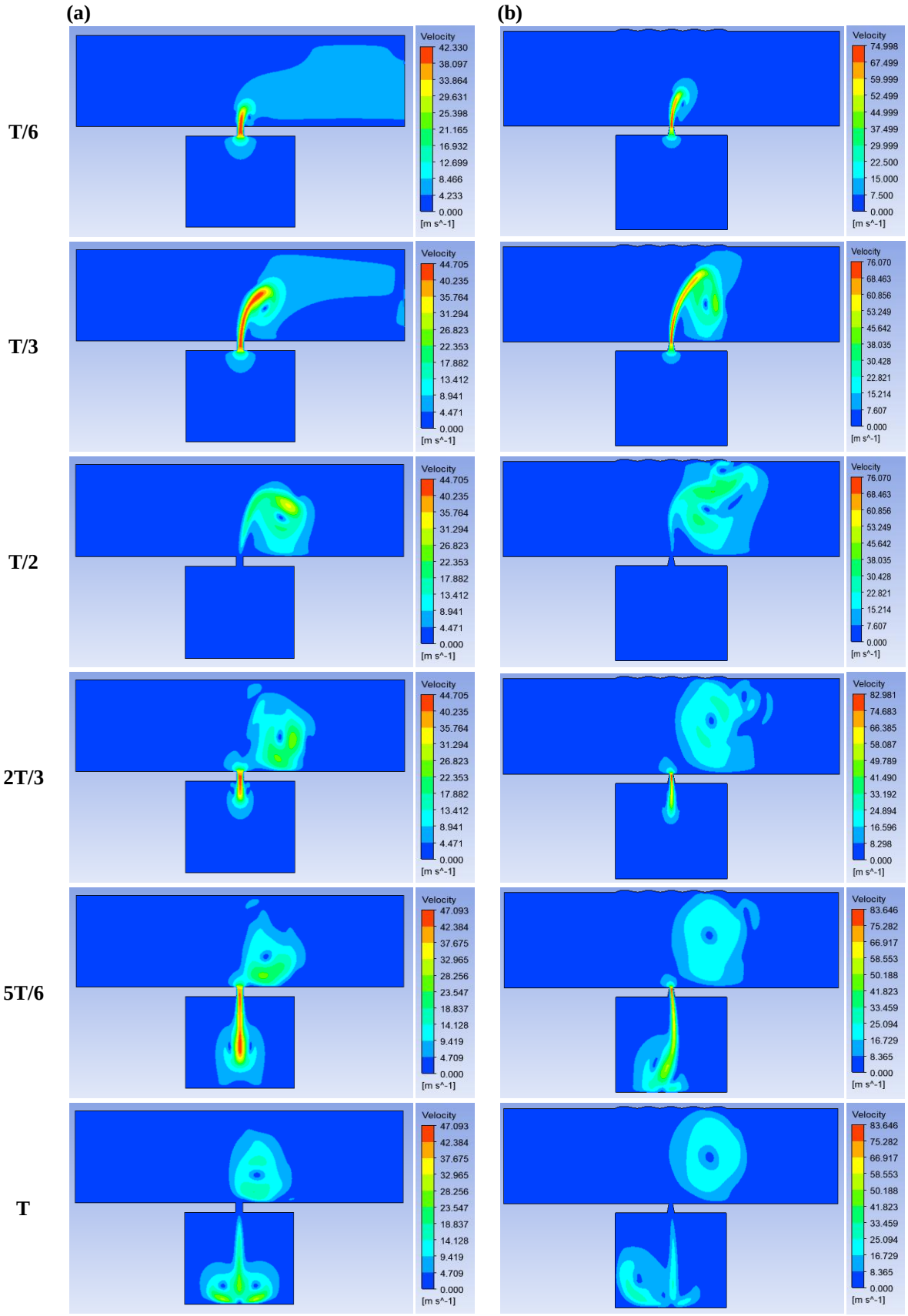

Figure 3.10. Contour plots of the magnitude velocity for one cycle, (a) Basic case, (b) Modified case with undulation heated wall of 10 µm; for V_i = 1 m/s; A = 75 µm.

3.4 Compare results of two synthetic jets at deferent amplitudes:

Now I use a configuration that carries two synthetic jets (two cavities) Figures 3.11 and 3.12 to see the influence of double synthetic jets on the heat transfer for the same summation conditions as the same oscillation function of the first study.

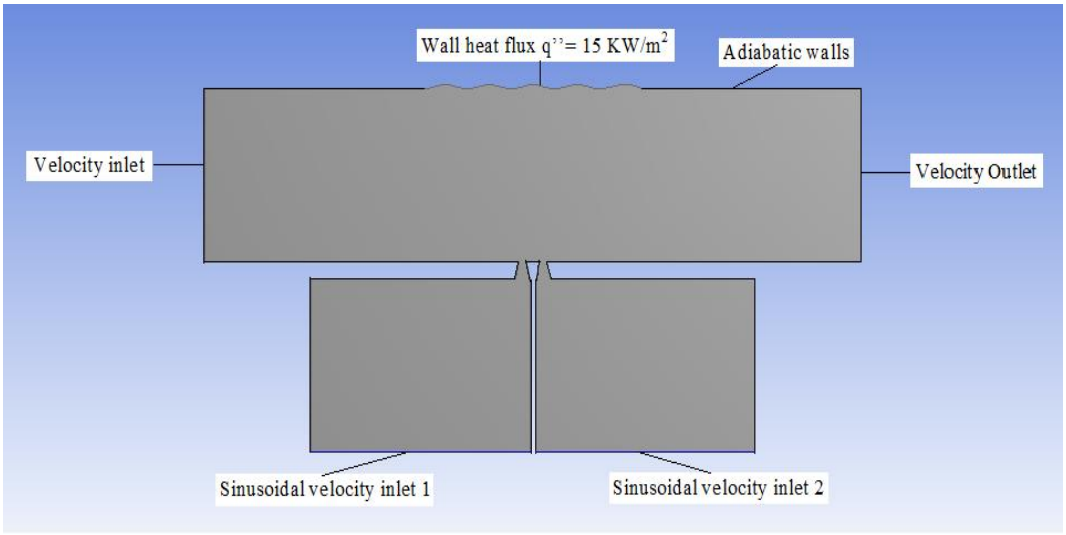

Figure 3.11. Representation of boundary conditions 2.

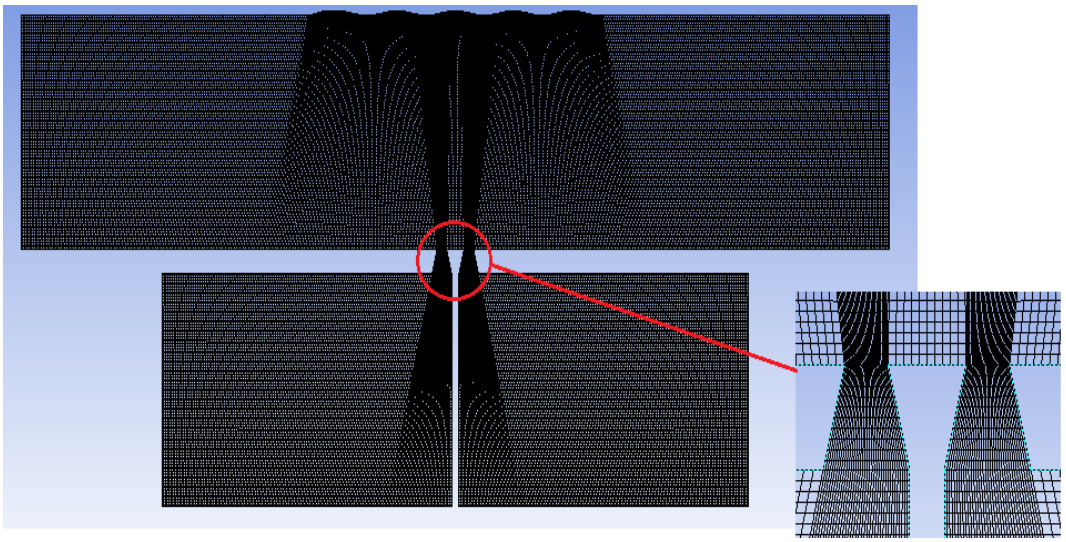

Figure 3.12. Computational grid 2.

Results and discussion

Results are presented in Figure 3.13 (a) Basic case, (b) Modified case with two cavities. For different oscillating amplitudes A= 25, 50 and 75 µm while the inlet velocity V_i= 1 m/s. The results show the effect of the ameliorations on the evolution of the Nusselt number, the values in the modified case are clearly higher compared to the results of the base case.

.

(a)

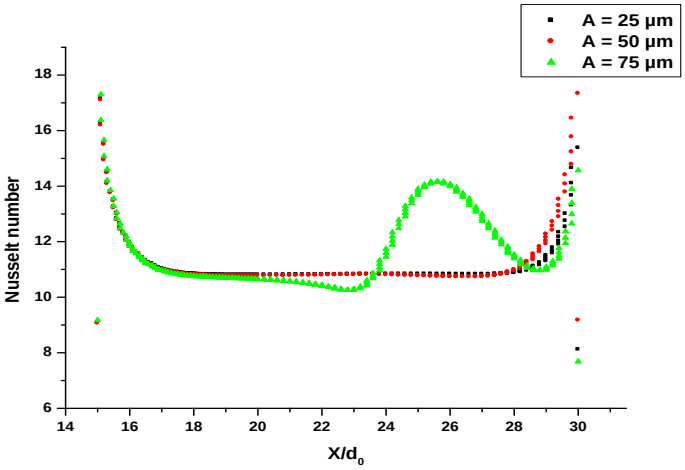

(b)

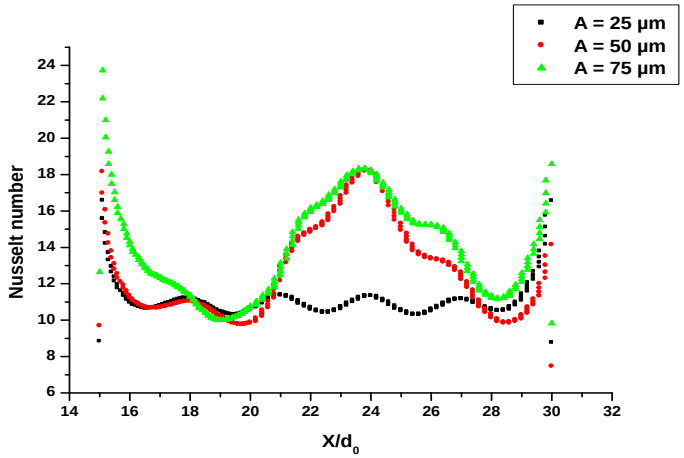

Figure 3.13. Nusselt number on the heated surface for different amplitudes, (a) Basic case, (b) Modified case with two cavities.

An additional analysis can be conducted with the Nusselt number time mean values. The corresponding amounts are shown in Figure 3.14, the above-mentioned propensity for the modified case with two cavities

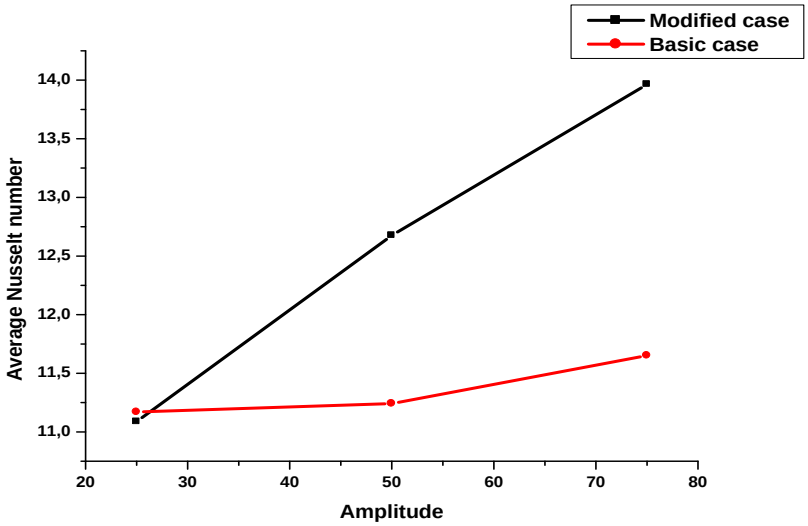

Figure 3.14. Average Nusselt Number for Basic case and Modified case with two cavities, for the three amplitudes A = 25, 50 and 75 µm, for V_i = 1 m/s.

Figure 3.15 shows the contours of velocity inside the (a) Basic case, (b) Modified case with two cavities. The results correspond to a transverse flow velocity V_i = 1 m/s and a jet amplitude A = 75 µm. The injection force of the fluid through the 2 diaphragms causes the process of generation of the vortex of the jet and creates a highly conductive heat flow structure on the heated surface. For one cycle, these analyses are shown in more detail in Figure 3.17 (page 63).

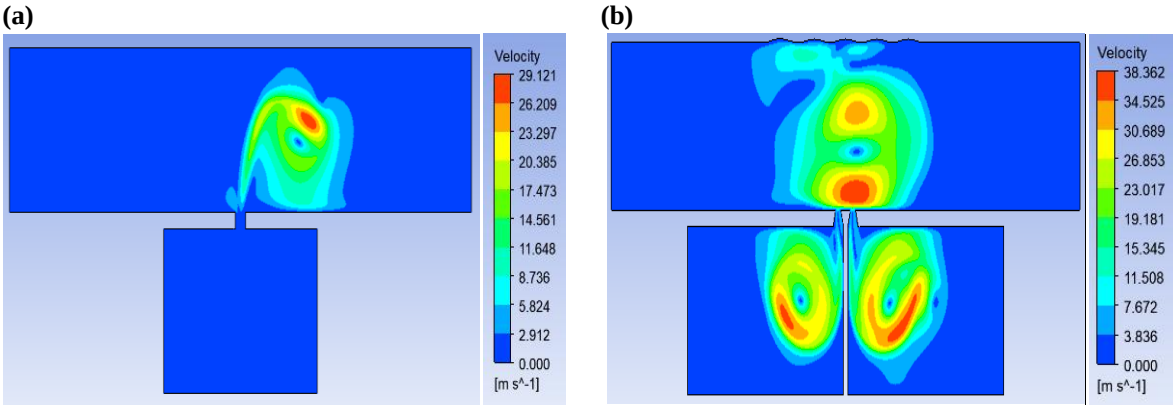

Figure 3.15. Contour plots of the magnitude velocity after one cycle for V_i = 1 m/s and A = 75 µm, (a) Basic case, (b) Modified case with two cavities.

Figure 3.16 shows the temperature field (a) Basic case and (b) Modified case with two cavities, at the end of an oscillating cycle.

The contours show a clear decrease in the temperature of the heated surface because the presence of the jet coming from the two cavities causes an area with a high exchange coefficient.

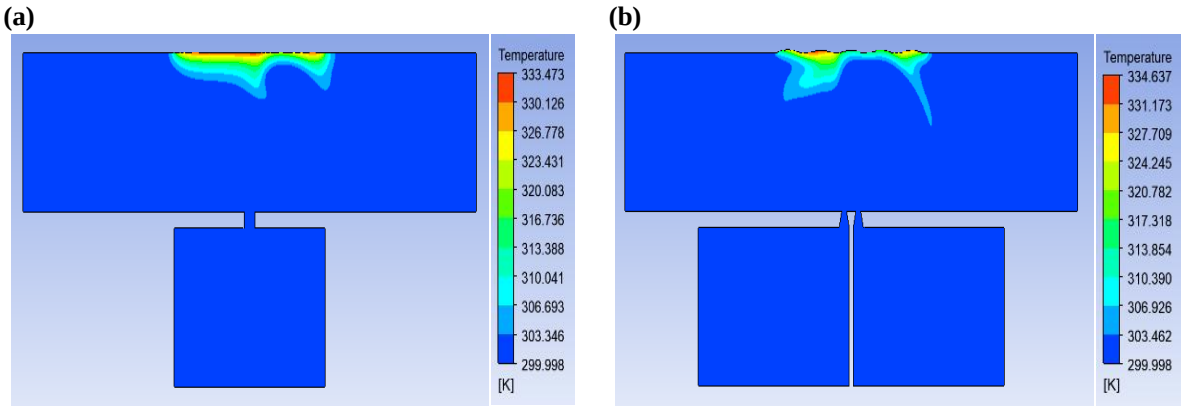

Figure 3.16. Contour plots of the static Temperature after one cycle for V_i = 1 m/s and A = 75 µm, (a) Basic case, (b) Modified case with two cavities.

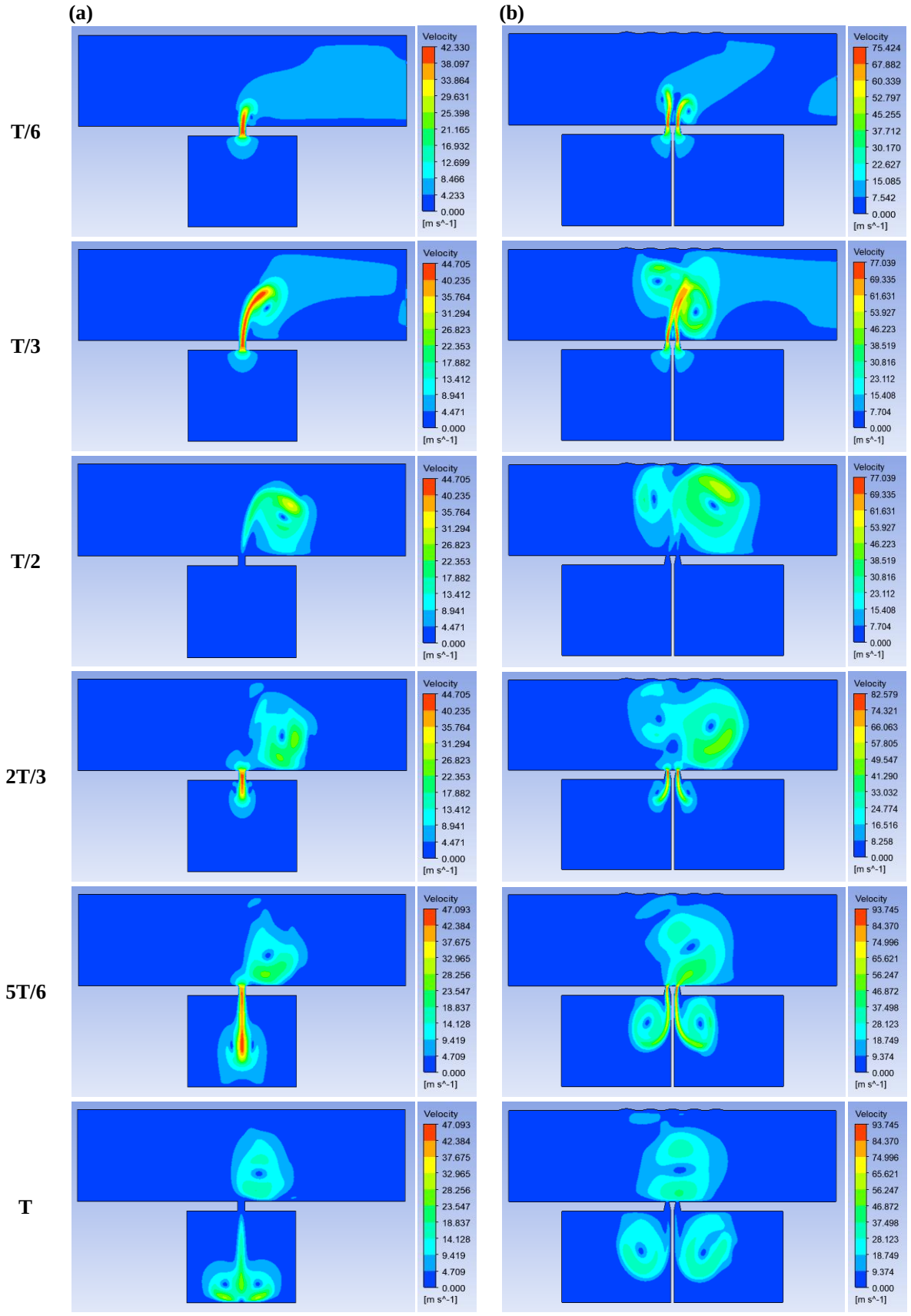

Figure 3.17. Contour plots of the magnitude velocity for one cycle, for V_i = 1 m/s and A = 75 µm, (a) Basic case, (b) Modified case with two cavities.

3.5 Compare results of two synthetic jets inclined at deferent amplitudes:

Here use the same configuration of 3rd simulation but the cavities are inclined 3 degrees to the horizontal for the same oscillation motion of diaphragm. Figures 3.18 and 3.19.

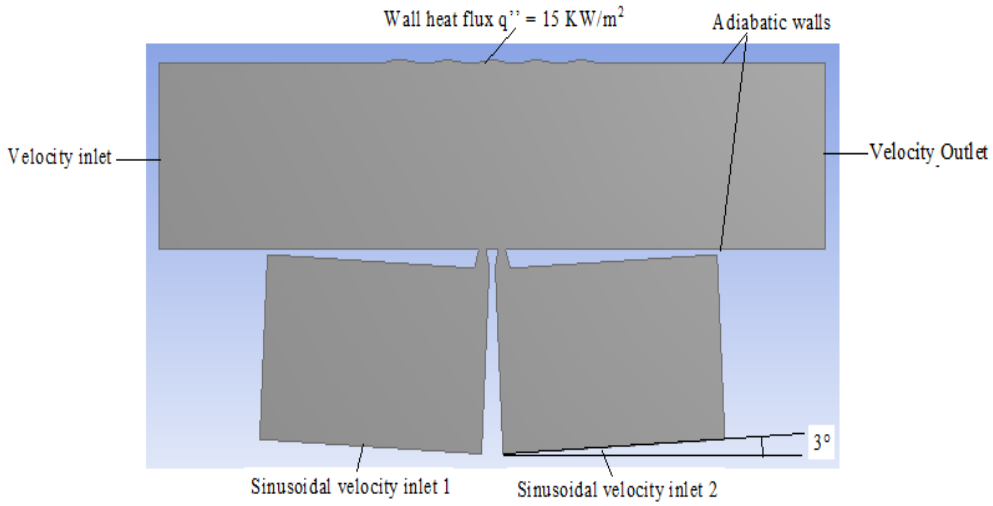

Figure 3.18. Boundary condition 3.

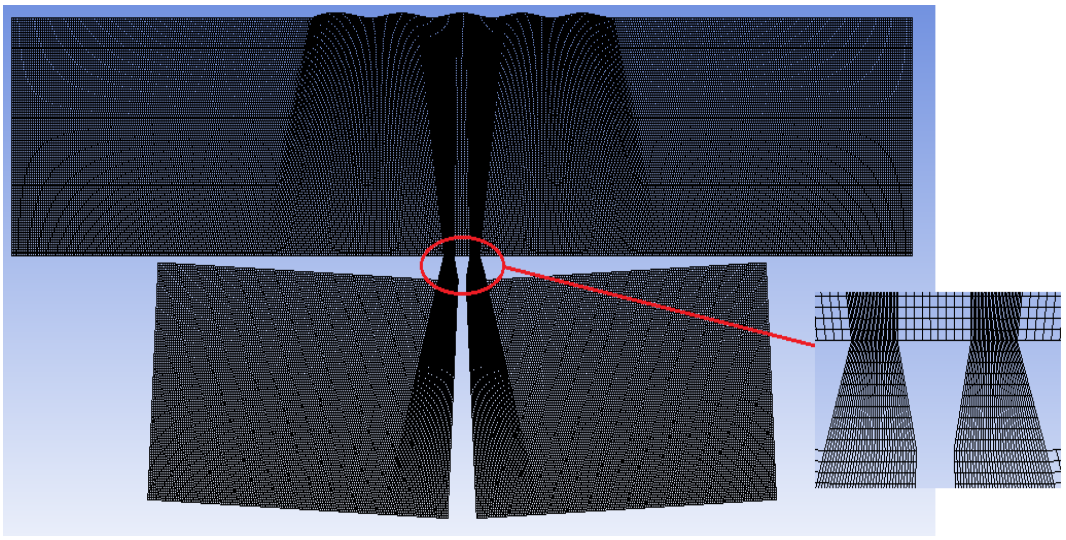

Figure 3.19. Structured quadratic mesh considered 3.

Results and discussion

Figure 3.20 (a) represents the basic configuration, while Figure 20 (b) shows the configuration which has two cavities inclined with 3° and converged form of orifices and 10 µm undulation heated wall, for different oscillating A= amplitudes 25, 50 and 75 µm while the inlet velocity *Vi* = 1 m/s, the comparisons between the results show that the modification affects in the evolution of Nusselt number, because Nusselt numbers are higher in the configuration with modifications. This results confirmed in Figure 3.21.

(a)

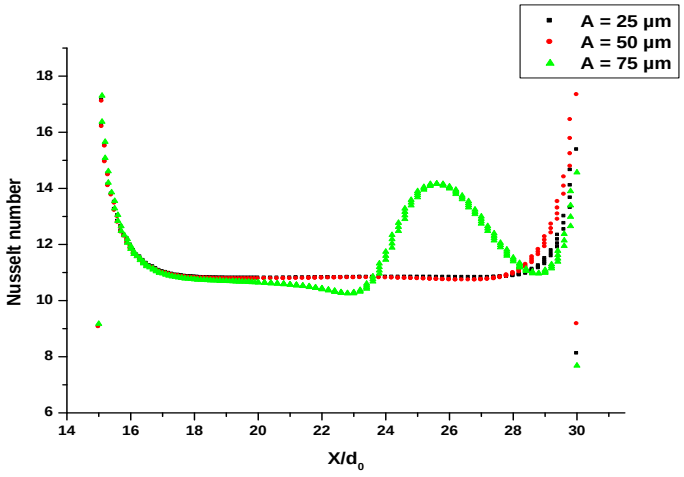

(b)

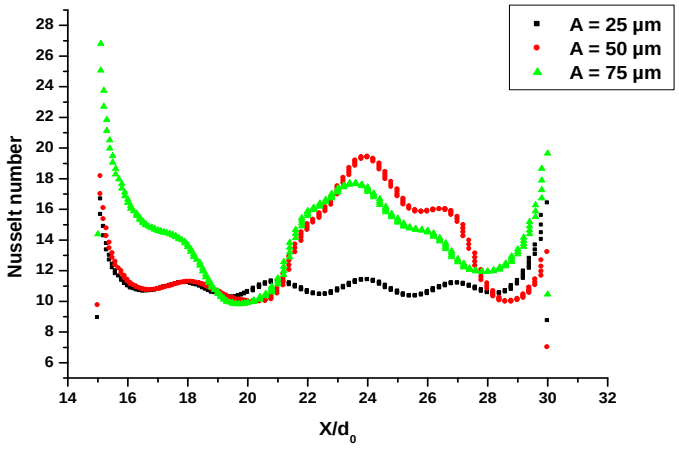

Figure 3.20. Nusselt number on the heated surface for different amplitudes, (a) Basic case, (b) Modified case with two cavities inclined.

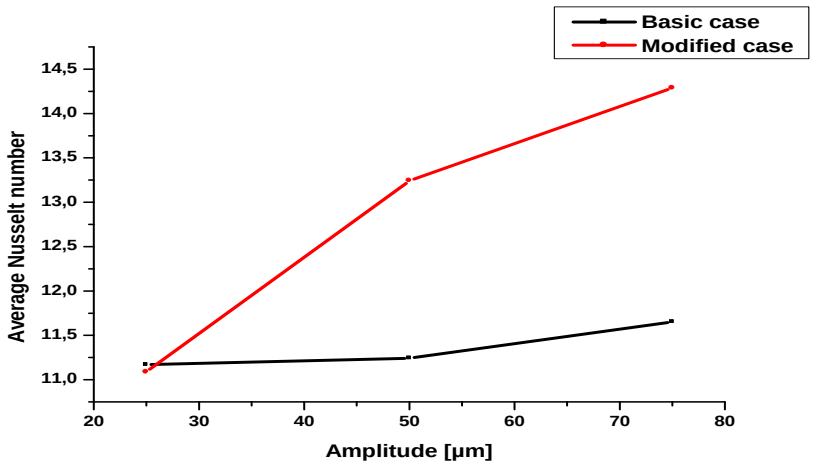

Figure 3.21. Average Nusselt Number for Basic case and Modified case with two cavities Inclined, for the three amplitudes A= 25, 50 and 75 µm, for V_i =1 m/s.

Figure 3.22 shows the contours of velocity for the perfect configuration and for the configuration which has two cavities inclined with 3° and converged form of orifices and 10 µm undulation heated wall at Vi = 1 m/s and a jet amplitude A = 75 µm, the contours show that the distribution of the field velocity is larger in the modified configuration because of the abrupt formation of the vortex.

These measurements are illustrated in more detail in Figure 3.24 for one cycle (page 68).

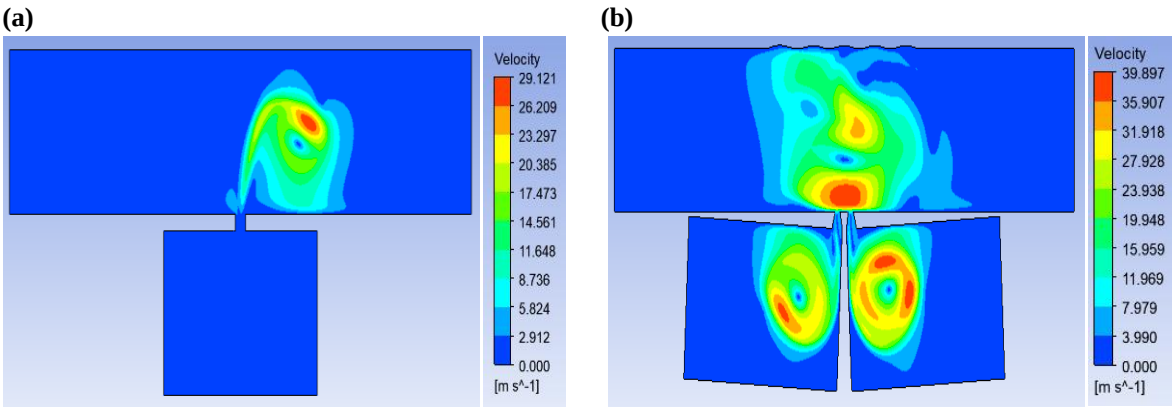

Figure 3.22. Contour plots of the magnitude velocity after one cycle for V_i = 1 m/s and A = 75 µm, (a) Basic case, (b) Modified case with two cavities inclined.

The change of the global temperature for the two examples studied is given by Figure 3.23. At the end of an oscillating cycle for the basic configuration (a) and for the configuration which has two cavities inclined with 3° and converged form of orifices and 10 µm undulation heated wall (b), at oscillating amplitude of A = 75 µm while the inlet velocity *Vi* = 1 m/s. From the distribution of temperature in the contours, we notice that the modification of geometry and synthetic jet reduce the temperature of the heated wall because of the broad contact between the wall and cooling fluid.

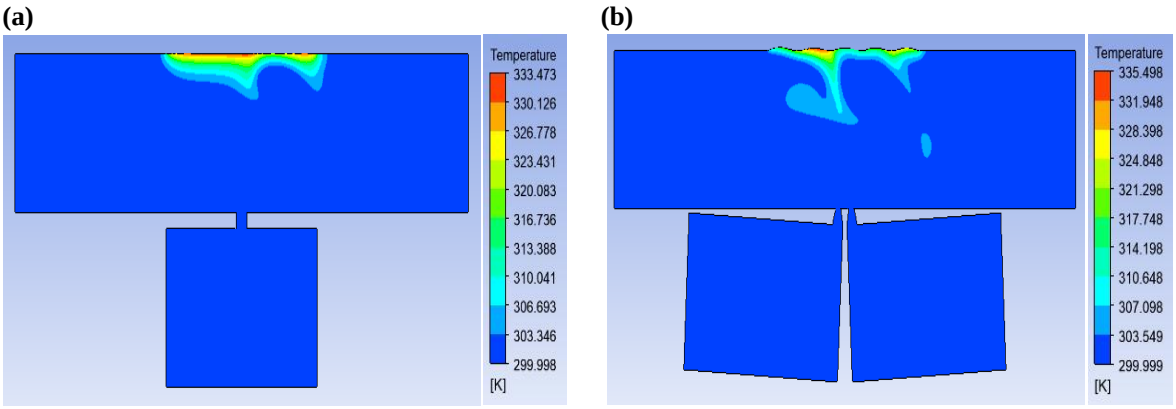

Figure 3.23. Contour plots of the static Temperature after one cycle, for V_i = 1 m/s and A = 75 µm, (a) Basic case, (b) Modified case with two cavities inclined.

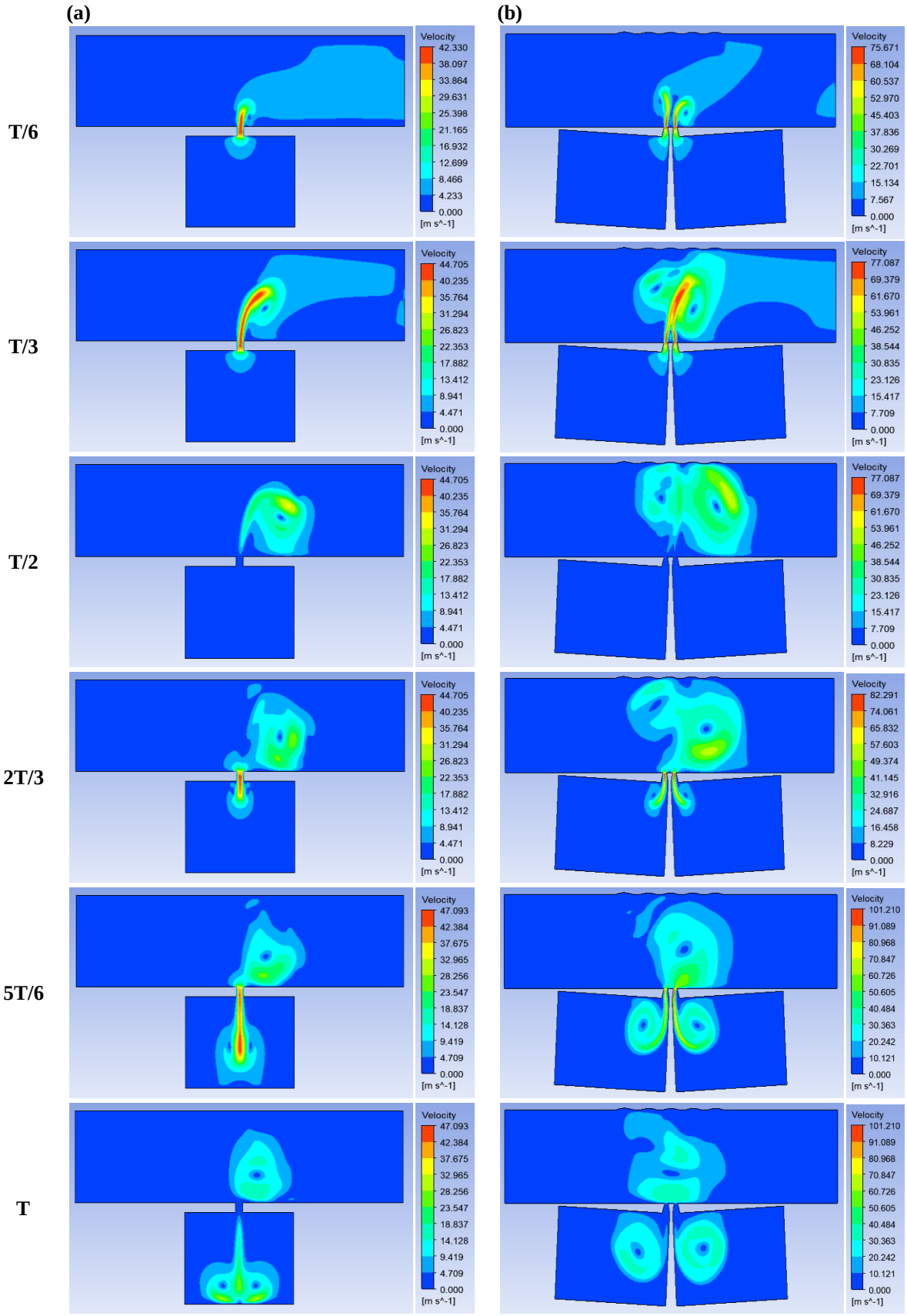

Figure 3.24. Contour plots of the magnitude velocity for one cycle, for V_i = 1 m/s and A = 75 µm, (a) Basic case, (b) Modified case with two cavities inclined.

3.6 Conclusion

Numerical results showing the influence of the obstruction and undulation degree on the heat transfer is presented. It was found that the converged form of orifice has a large influence on the formation of the large vertical structures and the effectiveness. The large vertical structures are the most responsible for the momentum and heat exchange between the jet and cross flow. The presence of the converged in the orifice changes the flow field and the vortex roll. The visualization of the flow shows that the synthetic jet penetrates the cross-flow much deeper in the case of the converged form of orifice than in normal form.

The Modified case with two cavities Inclined gives good results than the other cases and those results confirmed in Figure 3.25 for the changement of Nusselt number on the heated surface and Figure 3.26 for Average Nusselt Number.

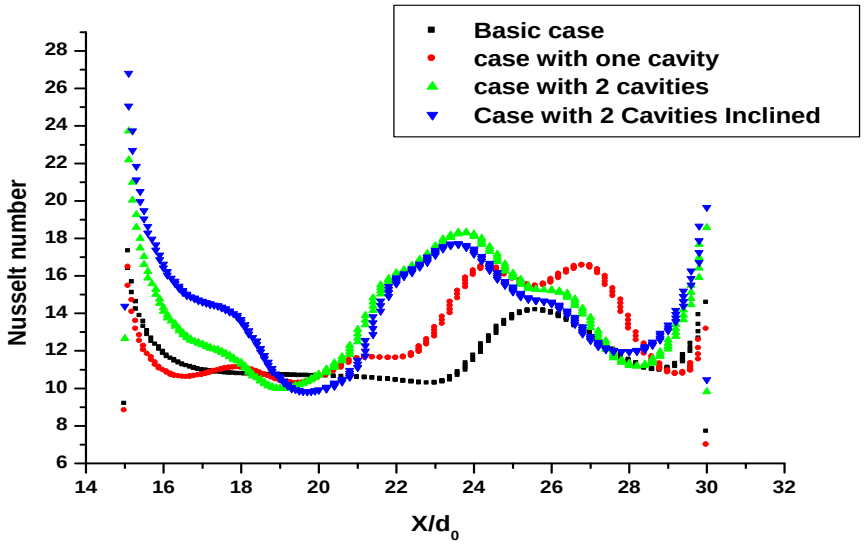

Figure 3.25. Nusselt number on the heated surface for (a) Basic case,

(b) Different Modified cases for V_i = 1 m/s and A = 75 µm.

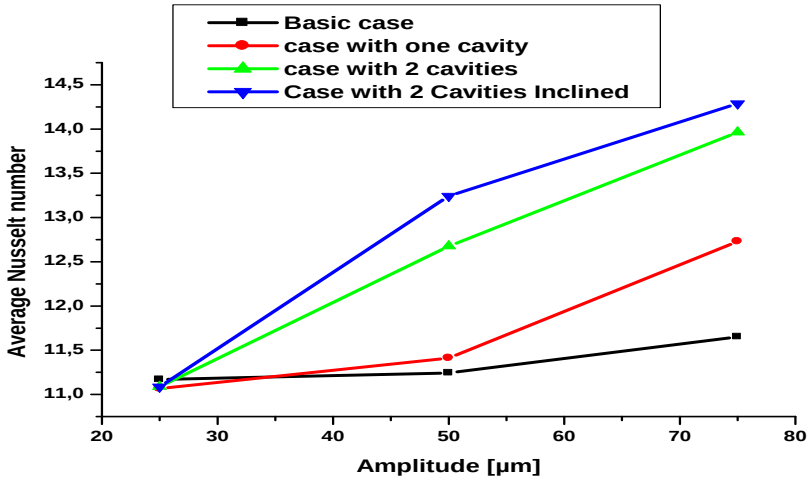

Figure 3.26. Average Nusselt Number for Basic case and Different Modified cases, for the three amplitudes A = 25, 50 and 75 µm, for V_i = 1 m/s.

Section 4

Results and Discussion :

Part 2

4.1 Compare results of two synthetic jets inclined at deferent amplitudes with a bi-periodic signal:

In this Part 2 we are beginning with the best configuration of the first results in Part 1 and we will applicate a variation in the signal of the diaphragm and see his affect in heat transfer and in Nusselt number. For this we will change the signal from periodic signal to bi-periodic signal for the modified case and compare their results with basic case with a periodic signal.

For that two geometrical configurations are considered, the first the basic configuration without any modification as shown in Figure 3.1 (Part 1) Figures 4.1 and 4.2 in first part of the results and presented in detail by Chandratilleke et al [82]. For this configuration the piston motion is sinusoidal with the function of displacement defined as [83]:

$$y = A \sin(\omega t - \varphi) \tag{4.1}$$

The second configuration was similar to the basic case but with two synthetic jets inclined with 3° and converged form of orifice and 10 µm of undulation heated wall ‘’modified case’’ Figure 4.1. The piston motion is bi-periodic non-sinusoidal with the function of displacement defined as

$$y = A\cos(\omega_1 t - \varphi) + \frac{1}{2} A\cos(\omega_2 t) \tag{4.2}$$

With

$$\omega_1 = 2 * \pi * f_0 \tag{4.3}$$

$$\omega_2 = \left(\frac{2}{3}\right) * \pi * f_0 \tag{4.4}$$

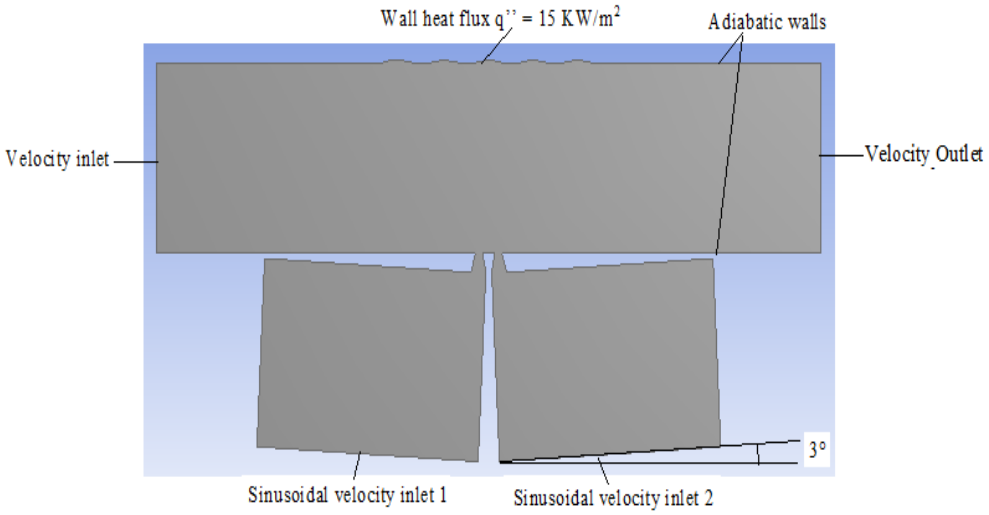

Figure 4.1. Boundary condition 4.

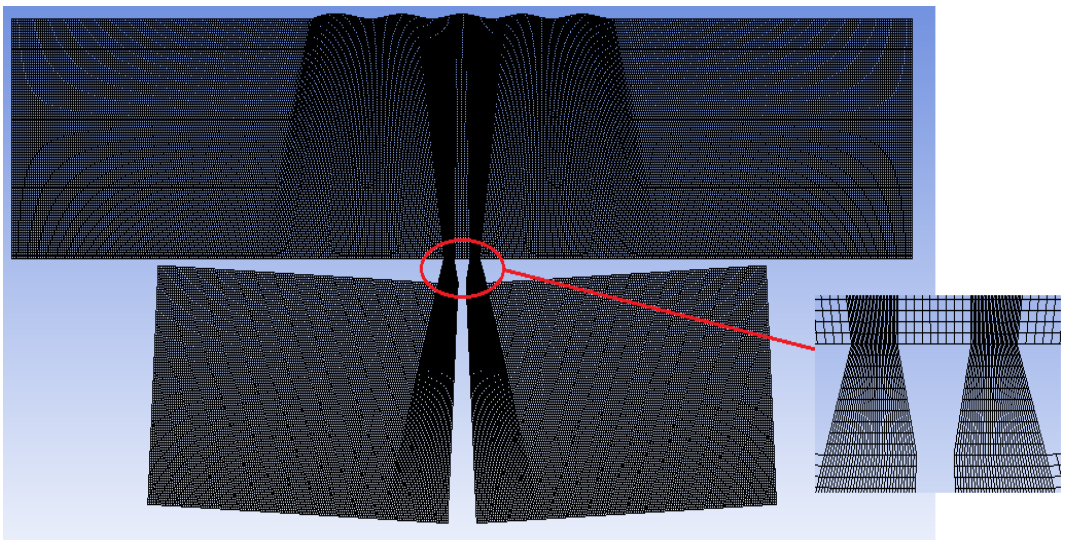

Figure 4.2. Structured quadratic mesh considered 4.

Results and discussion

Results for the basic case with a periodic signal and for the modified case with a bi-periodic signal are presented in Figure 4.3. (a) and 4.3. (b), respectively for different oscillating amplitudes A = 25, 50 and 75 µm and for an inlet velocity Vi = 1 m/s. Results show that Nusselt number increases with increasing the oscillation, and the maximum values could be obtained for the amplitude A = 75 µm. In addition, it is shown that Nusselt values for the modified case with a bi-periodic signal are much higher than the basic case.

(a)

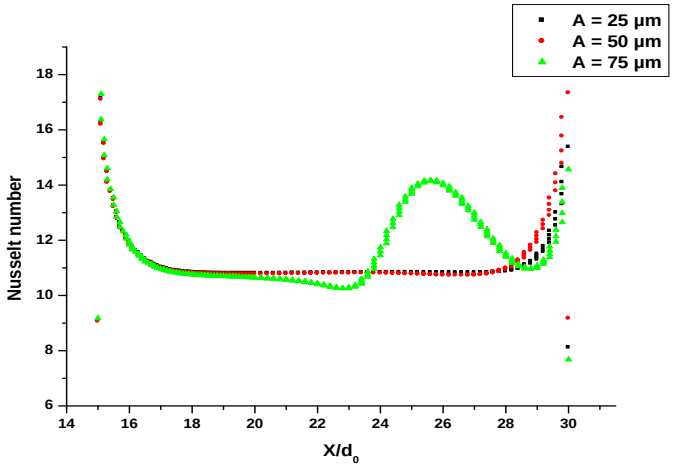

(b)

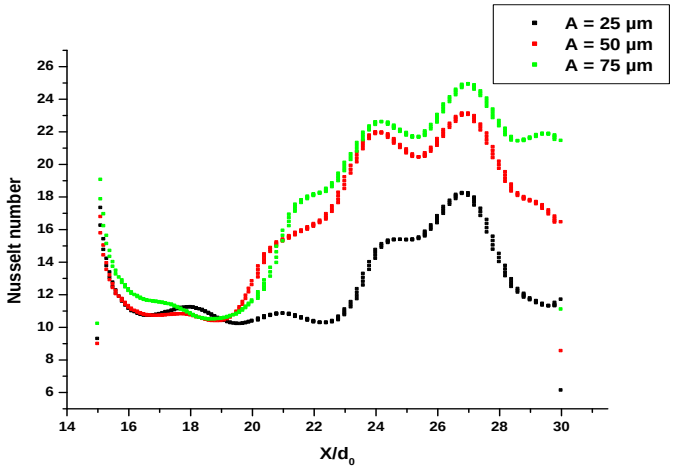

Figure 4.3. Nusselt number on the heated surface for different amplitudes, (a) Basic case with a periodic signal, (b) Modified case with a bi-periodic signal.

These results confirm that the proposed modifications influence the heat transfer rate and it is clearly shown in Figure 4.4 with an average difference of about 51% for case with two synthetic jets inclined with 3° and converged form of orifice and 10 µm of undulation heated wall.

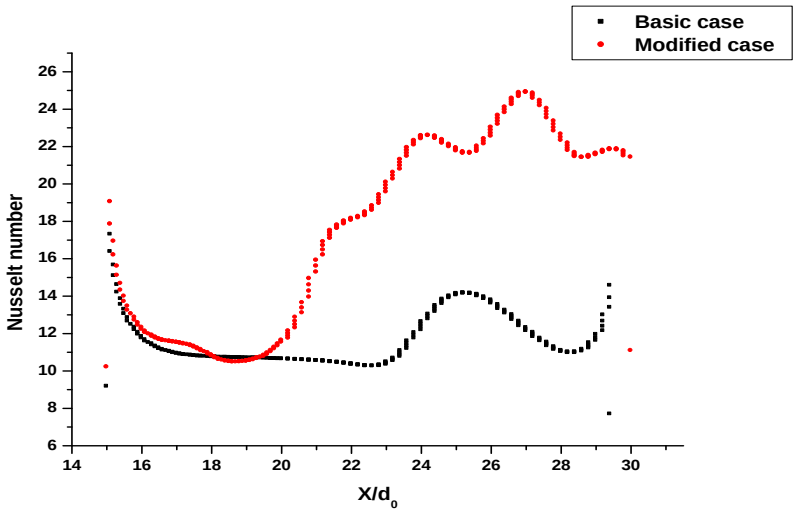

Figure 4.4. Comparison of Nusselt number for the heated surface between basic case with periodic signal and modified case with bi-periodic signal at V_i = 1 m/s; A = 75 µm.

To understand the evolution of the Nusselt number, Figure 4.5 shows the variation of the average Nusselt number for the three amplitudes A= 25, 50 and 75 µm, for Vi =1 m/s. It is shown that the case with modification gives higher values of Nusselt number.

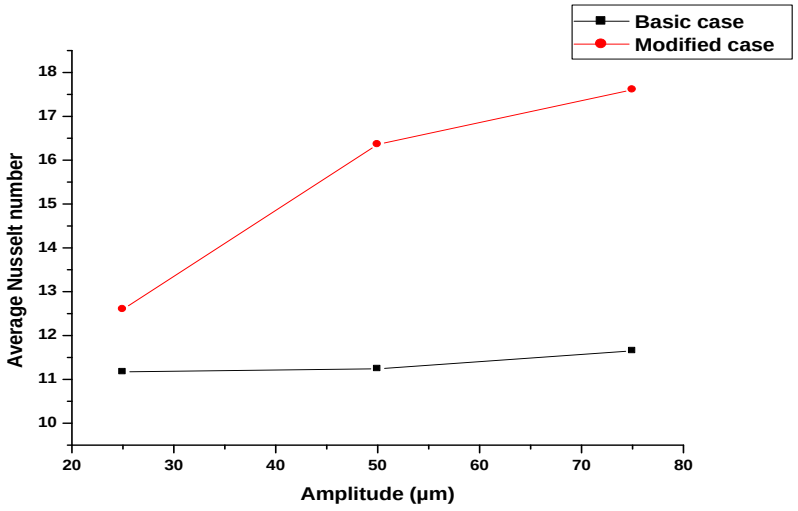

Figure 4.5. Average Nusselt Number for basic case with a periodic signal and modified case with a bi-periodic signal.

Figure 4.6 shows the contours of the magnitude velocity for the basic case with a periodic signal, and in the modified case with the bi-periodic signal. Results correspond to a transverse flow velocity Vi = 1 m/s and a jet amplitude A = 75 µm. Results show clearly that

the magnitude velocity for the modified case is higher because of the acting force of the bi-periodic signal and the generation of the jet vortex due to the small inclined flow coming from the modified orifice inclination and these results confirm what we have obtained in the previous Figures 3.3, 3.4 and 3.5. These results are presented in more detail for one cycle in Figure 4.8 (page 77).

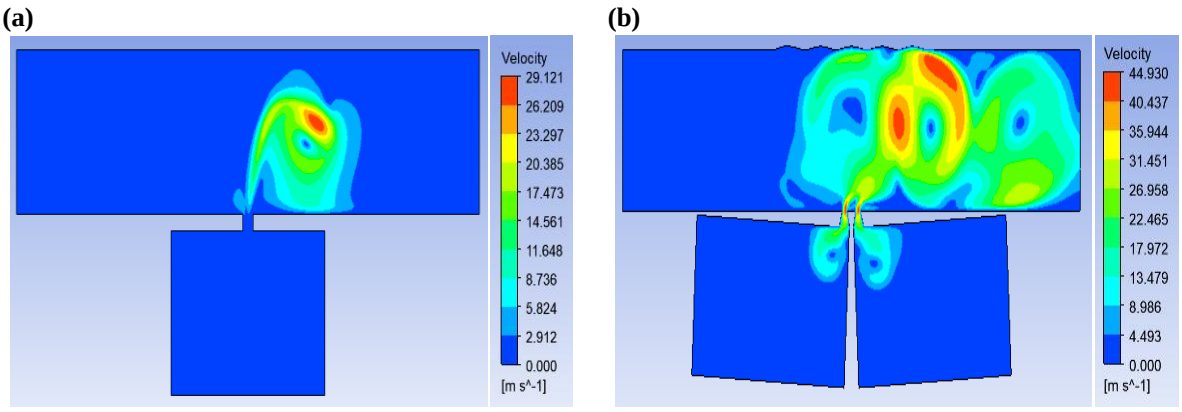

Figure 4.6. Contour plots of the magnitude velocity after one cycle for V_i = 1 m/s and A = 75 µm, (a) Basic case with a periodic signal, (b) Modified case with a bi-periodic signal.

The global temperature field in the channel at the end of an oscillating cycle is presented in Figure 4.7 (a) for the basic case with a periodic signal, and in Figure 4.7 (b) for the modified case with the a bi-periodic signal, at an oscillating amplitude of A = 75 µm and an inlet velocity Vi = 1 m/s. The contour clearly shows that the temperature decreases in the vicinity of the heated surface, for amplitude A = 75 µm the modified case with a bi-periodic signal is much colder than the basic case because the effect of the synthetic jet is high with the presence of two jets as well as the Bi-periodic signal extremely that a periodic signal.

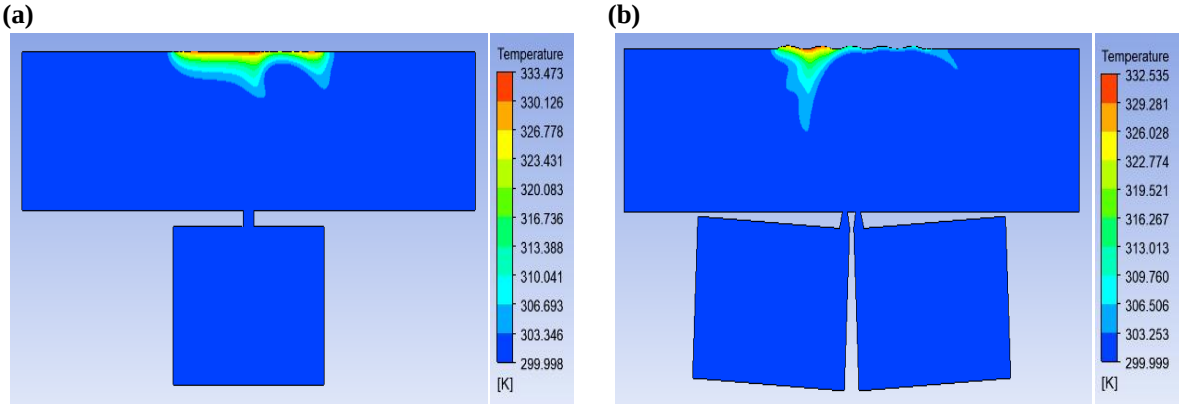

Figure 4.7. Contour plots of the static Temperature after one cycle for V_i = 1 m/s and A = 75 µm, (a) Basic case with a periodic signal, (b) Modified case with a bi-periodic signal.

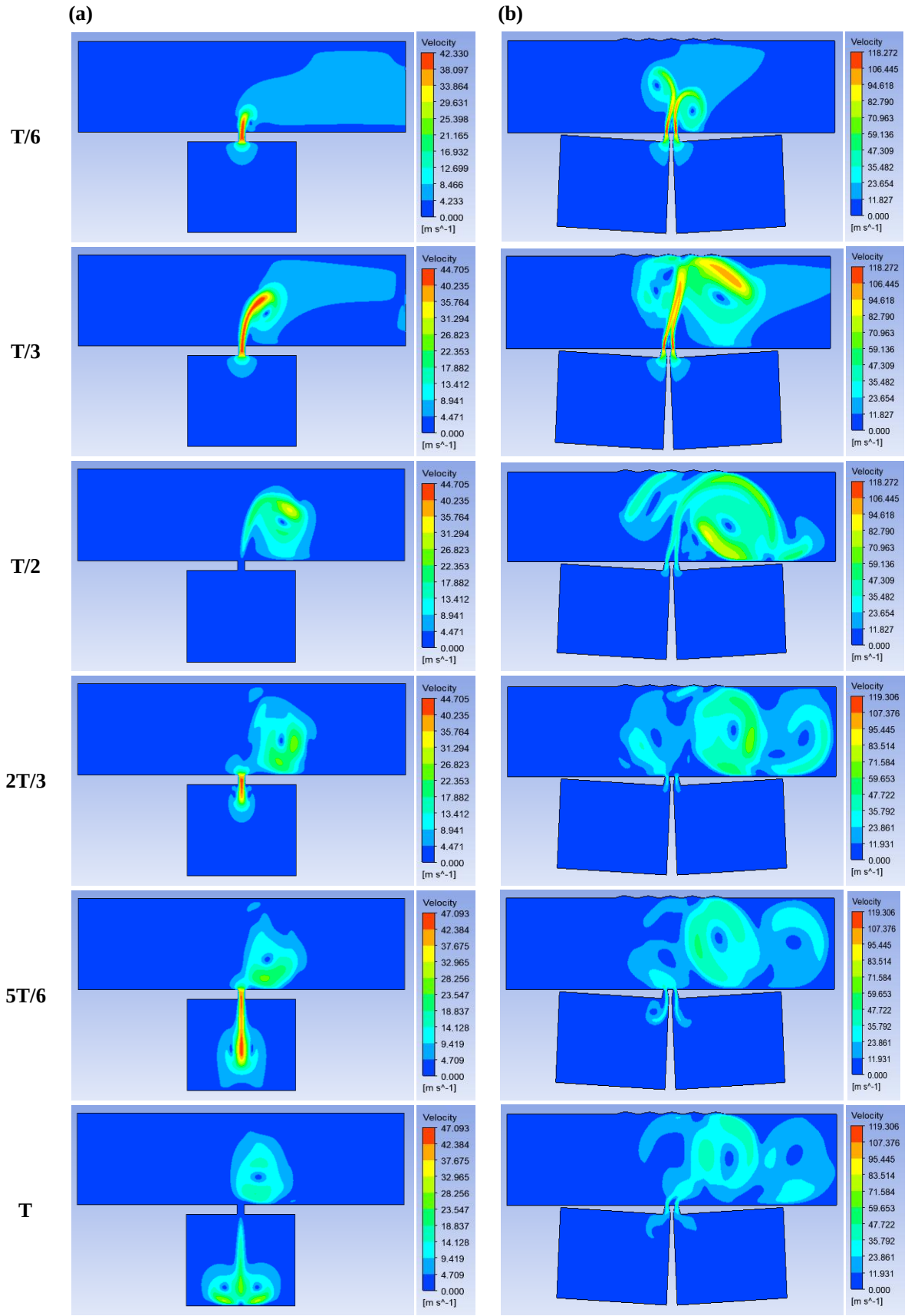

Figure 4.8. Contour plots of the magnitude velocity for one cycle for V_i = 1 m/s and A = 75 µm, (a) Basic case with a periodic signal, (b) Modified case with a bi-periodic signal.

4.2 Modification of the position of the cavities:

Here we use the same configuration of simulation 4 but we change the position of cavities Figures 4.9 and 4.10.

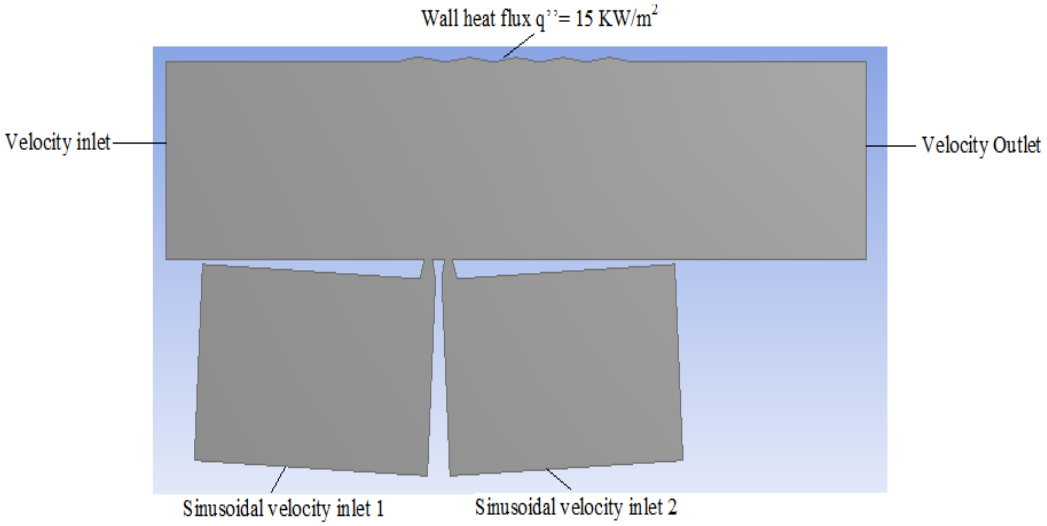

Figure 4.9. Boundary condition 5.

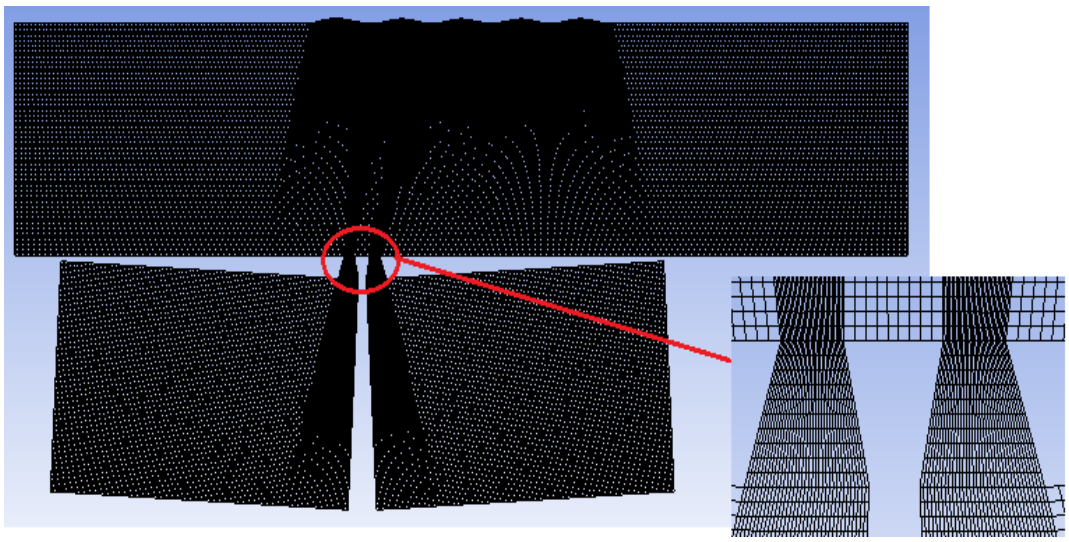

Figure 4.10. Structured quadratic mesh considered 5.

Results and discussion

The results in Figure 4.11 show that the local Nusselt number is high almost throughout the entire heated wall in the modified case due to the better homogeneity of the initial incoming fluid and the fluid injected through the diaphragm which allows most of the heated wall to be cooled. Figure 4.12 shows the comparison of Average Nusselt Number for basic case with a periodic signal and modified case with a bi-periodic signal.

(a)

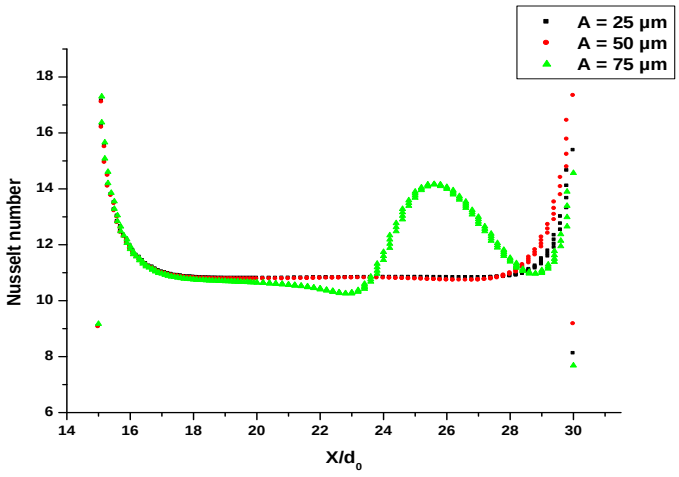

(b)

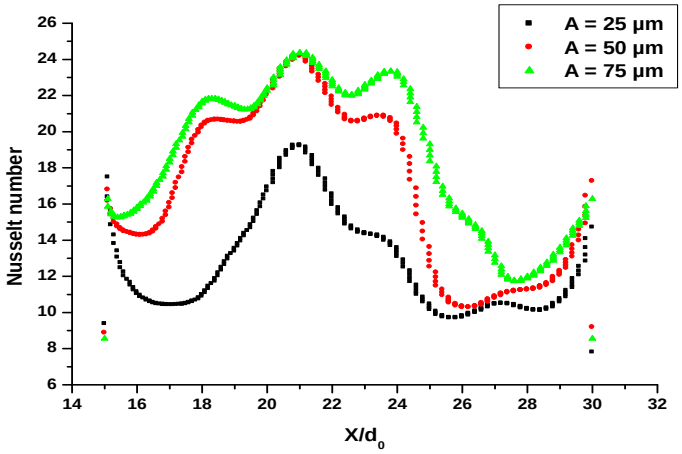

Figure 4.11. Nusselt number on the heated surface for different amplitudes, (a) Basic case with a periodic signal, (b) Modified case with a bi-periodic signal.

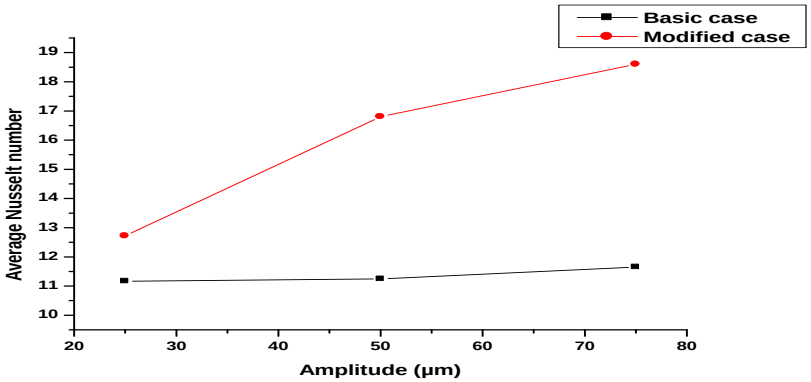

Figure 4.12. Average Nusselt Number for basic case with a periodic signal and modified case with a bi-periodic signal.

Figure 4.13 shows the magnitude velocity contours for the base case and the modified case. The results show that the magnitude velocity for the modified case is higher and that the turbulent flow starts before the heated surface, which gives maximum heat transfer and improved speed and cooling rate. These results are presented in more detail for one cycle in Figure 4.15 (page 81).

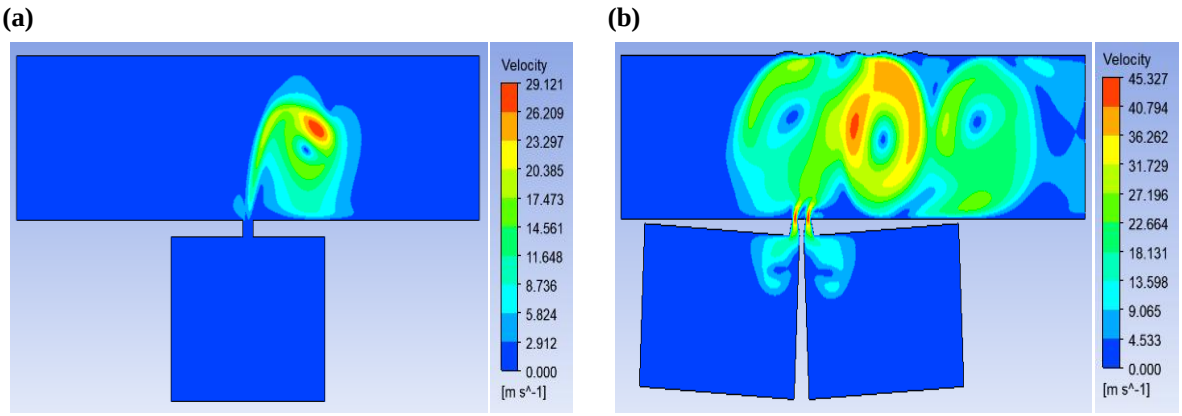

Figure 4.13. Contour plots of the magnitude velocity after one cycle for V_i = 1 m/s and A = 75 µm, (a) Basic case with periodic signal, (b) Modified case with bi-periodic signal.

The results in Figure 4.14 show the level curves of the static temperature after one cycle for Vi = 1 m/s and A = 75 µm is noted that the temperature dropped over the entire heated wall.

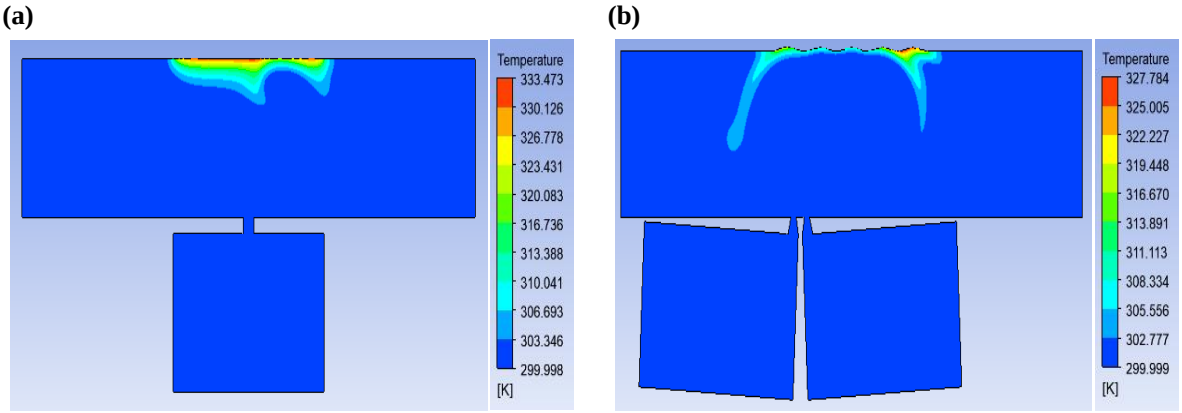

Figure 4.14. Contour plots of the static Temperature after one cycle for V_i = 1 m/s and A = 75 µm, (a) Basic case with a periodic signal, (b) Modified case with a bi-periodic signal.

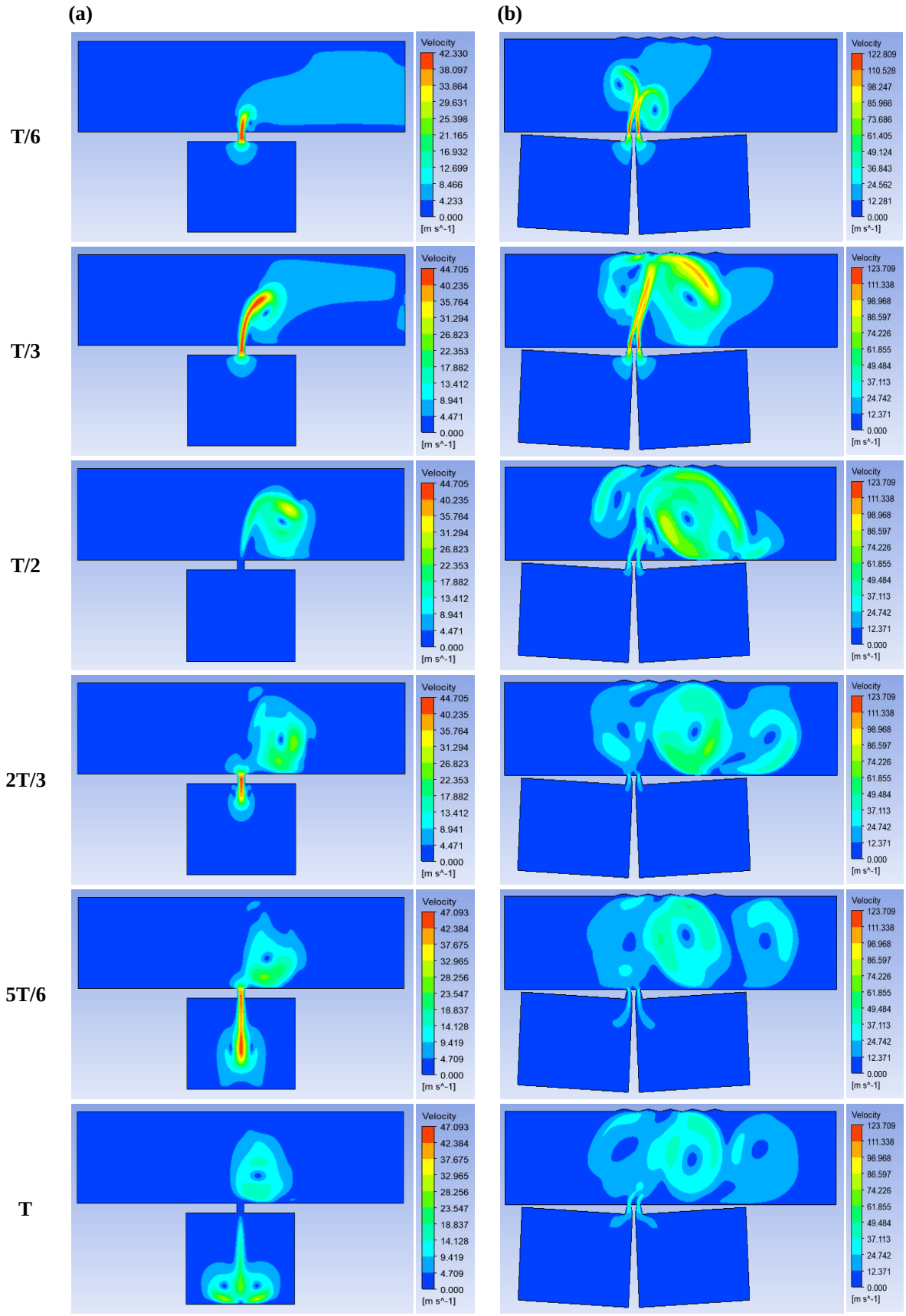

Figure 4.15. Contour plots of the magnitude velocity for one cycle for V_i = 1 m/s and A = 75 µm, (a) Basic case with periodic signal, (b) Modified case with bi-periodic signal.

4.3 Conclusion

Temperature contours showed that the form of the undulant heated wall helped the emigration of the temperature and has a large influence on the heat transfer rate. The presence of inclined cavities with 3° and converged form of orifice and 10 μm of undulation heated wall increased the Nusselt number by about 60% compared with the basic case due to the increased vortices in the flow domain.

General conclusion

In the present study, the form of heating surface and the signal of the diaphragm for a synthetic jet has been modified to improve the synthetic jet performance. These modifications are novel and have been applied for the first time with very good thermal enhancement efficiency for microchannels with synthetic jets applications.

The comparison between the basic and the modified configurations have been numerically investigated using ANSYS fluent softwar. The k- ω SST turbulence model is applied with success to highlight the main features of the presence of such obstruction. For comparison purpose; the perfect case is also done.

Our study is composed of two parts, the first part presents the effect of changing the geometry shape, the effect of the synthetic jet with single cavity and double cavity, also the effect of the injection orifice shape on heat transfer.

The second part is addressed to the operation of the diaphragm by changing the signal function. In the first part, the diaphragm is supplied with a periodic sinusoidal signal, but in this part, this signal is changed to a bi-periodic signal.

This study gives many of the results that prove the reliability of the cooling system of electronic components by the synthetic jet:

– The presence of the synthetic jet causes a turbulent regime which improves the thermal change between the fluid and the heated wall.

– The heated wall is cooled quickly with the synthetic jet than simple applications.

– The cooling efficiency increases by 30% in the presence of geometry changes with a synthetic jet of a periodic sinusoidal signal and by 60% in the presence of a bi-periodic signal.

For future research related to this field :

– 3D simulation is being prepared to understand the heat transfer phenomenon and cooling parameters of electronic components.

– Launch an energy study (consumption and work) to compare with thermal efficiency.

References

References

[1] A. Arshad, M. Jabbal, Y. Yan; Synthetic jet actuators for heat transfer enhancement – A critical review, International Journal of Heat and Mass Transfer 146 (2020) 118815.

[2] S.S. Anandan, V. Ramalingam; Thermal management of electronics: A review of literature, Thermal Science, Vol. 12 (2008), No. 2, pp. 5-26.

[3] C. Lasance, R. Simons; Advances in high-performance cooling for electronics, Electron. Cool. 11 (4) (2005) 22–39.

[4] Kathryn Oseen-Senda; Etude de l'ébullition du pentane en monocanal en vue de son utilisation pour le refroidissement des piles à combustible PEMFC, Phd Thesis, Université Henri Poincaré - Nancy I (2006).

[5] P.E. Phelan, V.A. Chiriac, Tien-Yu Tom Lee; Current and future miniature refrigeration cooling technologies for high power microelectronics, IEEE Transactions on Components and Packaging Technologies, VOL. 25, NO. 3, 356–365 (2002), pp. 356–365.

[6] M. Faraji, H. El Qarnia; Optimisation d'un système de stockage d'énergie par chaleur latente de fusion : application au refroidissement d'une composante électronique. 13èmes Journées Internationales de Thermique, Albi, France du 28 au 30 Août 2007, pp. 5.

[7] Luc Meysenc; Etude des micro-échangeurs intégrés pour le refroidissement des semi-conducteurs de puissance. Phd Thesis, Institut National Polytechnique de Grenoble - INPG (1998).

[8] Roland Baviere; Etude de l'Hydrodynamique et des Transferts de Chaleur dans des Microcanaux. Phd Thesis, Université Joseph-Fourier - Grenoble I (2005).

[9] Palne Mogensen AB, Fluid to duct wall heat transfer in duct system heat storages, Swedish Council for Building Research, ref : 3 International conference on subsurface heat storage in theory and practice, Sweden 1983, pp 652-657.

[10] A. Mativet, F. Meunier; Etude expérimentale d'un procédé de chauffage et de refroidissement par changement de phase du fluide caloporteur (1997).

[11] Z.J. Zuo, M.T. North; Miniature high heat flux heat pipes for cooling electronics, Proc SEE 573–579 (2000).

[12] K.A. Estes, I. Mudawar; Correlation of sauter mean diameter and critical heat flux for spray cooling of small surfaces, International Journal of Heat and Mass Transfer 38 (1995), pp. 2985–2996.

[13] Daniel Thibault; Etude du refroidissement par impact de jets à travers une paroi mince et avec un écoulement cisaillant amont : application aux aubes de turbines, Phd Thesis, ISAE-ENSMA Ecole Nationale Supérieure de Mécanique et d'Aérotechique - Poitiers (2009).

[14] Francis J. Stenger; Experimental feasibility study of Water-filled Capillary-pumped heat transfer Loops, Lewis Research Center, Ohio, NASA TM X-1310 (1966).

[15] Amélie Veillere; Drains thermiques adaptatifs : Cuivre allié / Fibre de Carbone, Phd Thesis, Université Sciences et Technologies - Bordeaux I (2009).

[16] Boris Bellin; Contributions a l'étude des bobinages supraconducteurs : le projet dga du SMES HTS impulsionnel, Phd Thesis, Institut National Polytechnique de Grenoble – INPG (2006).

[17] K.C. Nathsarma, B.B. Nayak, P. Brahmbhatt, S. Pradhan; Purification of niobium oxide by dissolution and solvent extraction, Minerals & Metallurgical Processing Vol. 28 No. 4, November 2011, pp.204-205.

[18] T. Murugan, M. Deyashi, S. Dey, S.C. Rana, P. Chatterjee; Recent developments on synthetic jets, Defence Science Journal, Vol. 66, No. 5, September 2016, pp. 489-498.

[19] R. Holman, Y. Utturkar, R. Mittal, Barton L. Smith, L. Cattafesta; Formation criterion for synthetic jets, AIAA Journal, vol. 43,No 10, pp. 2110-2116, 2005.

[20] L. Silva-Llanca; Replicating impinging synthetic jets as a train of consecutive viscous lamb-ossen vortex pairs, 15th IEEE 15th IEEE ITHERM Conference, IEEE, 2016, pp. 930–938.

[21] J. P. d'Alençon, L. Silva-Llanca; Two-dimensional numerical analysis of a low Re turbulent impinging synthetic jet, 15th IEEE 15th IEEE ITHERM Conference, IEEE, 2016, pp. 921–929.

[22] U. Akdag, O. Cetin, D. Demiral, I. Ozkul; Experimental investigation of convective heat transfer on a flat plate subjected to a transversely synthetic jet, International Communications in Heat and Mass Transfer 49 (2013), pp. 96–103.

[23] G. Krishan, Kean C. Aw, Rajnish N. Sharma; Synthetic jet impingement heat transfer enhancement – A review, Applied Thermal Engineering 149 (2019), pp. 1305–1323

[24] Suresh V. Garimella, T. Persoons, J. Weibel, Lian-Tuu Yeh; Technological drivers in data centers and telecom systems, Multiscale thermal, electrical and energy management, Applied Energy 107 (2013), pp. 66–80.

[25] J. Stephen Campbell, W. Z. Black, A. Glezer, J. G. Hartley; Thermal management of a laptop computer with synthetic air microjets, Inter Society Conference on Thermal Phenomena, IEEE, Seattle, Washington, May (1998), pp.27-30.

[26] R. Mahalingam, A. Glezer; Air cooled heat sinks integrated with synthetic jets, Inter Society Conference on Thermal Phenomena, IEEE, Vol. 27 (2002), pp. 285-291.

[27] R. Mahalingam, N. Rumigny, A. Glezer; Thermal management using synthetic jet ejectors, IEEE, Vol. 27 No. 3 (2004), pp. 439-444.

[28] T. Persoons, K. Balgazin, K. Brown, D.B. Murray; Scaling of convective heat transfer enhancement due to flow pulsation in an axisymmetric impinging jet, Journal of Heat and Transfer 135 (2013) 111012-111022.

[29] J. Mohammadpour, M. Rajabi-Zargarabadi, A.S. Mujumdar, H. Ahmadi; Effect of intermittent and sinusoidal pulsed flows on impingement heat transfer from a concave surface, International Journal of Thermal Sciences 76 (2014), pp. 118-127.

[30] T. Persoons, A. McGuinn, D. B. Murray; A general correlation for the stagnation point Nusselt number of an axisymmetric impinging synthetic jet, International Journal of Heat and Mass Transfer 54 (2011), pp. 3900–3908.

[31] B. Sagot, G. Antonini, F. Buron; Heat transfer by jet impacting on plate plan corruguée, French conger of thermics, SFT 2007, Ile des Embiez, 29 mai - 1er juin 2007.

[32] C.S. Greco, A. Ianiro, G. Cardone; Time and phase average heat transfer in single and twin circular synthetic impinging air jets, International Journal of Heat and Mass Transfer 73 (2014), pp. 776–788.

[33] M.B. Gillespie, W.Z. Black, C. Rinehart, A. Glezer; Local convective heat transfer from a constant heat flux flat plate cooled by synthetic air jets, Journal of Heat Transfer 128 (2006), pp. 990–1000.

[34] L.A. Silva, A. Ortega; Convective heat transfer in an impinging synthetic jet: a numerical investigation of a canonical geometry, Journal of Heat Transfer 135 (2013), pp. 082201-1 - 082201-11.

[35] D.S. Kercher, J.-B. Lee, O. Brand, M.G. Allen, A. Glezer; Microjet cooling devices for thermal management of electronics, IEEE Transactions on Components and Packaging Technologies 26 (2003), pp. 359–366.

[36] O. Ghaffari, S. A. Solovitz, M. Arik; An investigation into flow and heat transfer for a slot impinging synthetic jet, International Journal of Heat and Mass Transfer 100 (2016), pp. 634–645.

[37] P. Gil, J. Wilk; Heat transfer coefficients during the impingement cooling with the use of synthetic jet, International Journal of Thermal Sciences 147 (2020), 106132.

[38] Laxmikant D. Mangate, Mangesh B. Chaudhari; Experimental study on heat transfer characteristics of a heat sink with multiple-orifice synthetic jet, International Journal of Heat and Mass Transfer 103 (2016), pp. 1181–1190.

[39] C. Greco, G. Castrillo, C. Crispo, T. Astarita, G. Cardone; Investigation of impinging single and twin circular synthetic jets flow field, Experimental Thermal and Fluid Science 74 (2016), pp. 354–367.

[40] T. Persoons, T.S. O'Donovan, D.B. Murray; Heat transfer in adjacent interacting impinging synthetic jets, ASME 2009 Heat Transfer Summer Conference collocated with the InterPACK09 and 3rd Energy Sustainability Conferences, American Society of Mechanical Engineers, 2009, pp. 955–962.

[41] G. Paolillo, C.S. Greco, G. Cardone; Impingement heat transfer of quadruple synthetic jets, International Journal of Heat and Mass Transfer 135 (2019), pp. 1192–1206.

[42] Zh-bing Luo, X. Deng, Zhi-xun Xia, L. Wang, Wei-jie Gong; Flow field and heat transfer characteristics of impingement based on a vectoring dual synthetic jet actuator, International Journal of Heat and Mass Transfer 102 (2016), pp. 18–25.

[43] M. Chaudhari, B. Puranik, A. Agrawal; Multiple orifice synthetic jet for improvement in impingement heat transfer, International Journal of Heat and Mass Transfer 54 (2011), pp. 2056–2065.

[44] E. Fanning, T. Persoons, D.B. Murray; Heat transfer and flow characteristics of a pair of adjacent impinging synthetic jets, International Journal of Heat and Fluid Flow 54 (2015), pp. 153–166.

[45] Xiao-ming Tan, Jing-zhou Zhang, Shan Yong, Gong-nan Xie; An experimental investigation on comparison of synthetic and continuous jets impingement heat transfer, International Journal of Heat and Mass Transfer 90 (2015), pp. 227–238.

[46] Lei Wang, Li-Hao Feng, Jin-Jun Wang, Tian Li; Characteristics and mechanism of mixing enhancement for noncircular synthetic jets at low Reynolds number, Experimental Thermal and Fluid Science 98 (2018), pp. 731–743.

[47] M. Chaudhari, B. Puranik, A. Agrawal; Effect of orifice shape in synthetic jet based impingement cooling, Experimental Thermal and Fluid Science 34 (2010), pp. 246–256.

[48] C.M. Crispo, C.S. Greco, G. Cardone; Convective heat transfer in circular and chevron impinging synthetic jets, International Journal of Heat and Mass Transfer 126 (2018), pp. 969–979.

[49] A.K.M.F Hussain, K.B.M. Zaman; Vortex pairing in a circular jet under controlled excitation, Part 2, 1980, Coherent structure dynamics, Journal of Fluid Mechanics vol 101, part 03 (1980), pp. 493- 544.

[50] L. Huang, M.S. El-Genk; Heat transfer and flow visualization experiments of swirling, multi-channel and conventional impinging jets, International Journal of Heat and Mass Transfer 41 No. 3 (1998) , pp. 583-600.

[51] S. Laouedj, J.P. Solano, A. Benazza; Synthetic jet cross-flow interaction with orifice obstruction, International Journal of Numerical Methods for Heat and Fluid Flow, Vol. 25 No. 4 (2015), pp. 749-761.

[52] Shu-Shen Hsu, Zdenek Travnicek, Chi-Cheng Chou, Cha-Chih Chen, An-Bang Wang; Comparison of double-acting and single-acting synthetic jets, Sensors and Actuators A 203 (2013), pp. 291– 299.

[53] S. Cadirci, H. Gunes, U. Rist; Active flow control applications with a jet and vortex actuator in a laminar cross flow, International Journal of Heat and Fluid Flow 39 (2013), pp. 146–159.

[54] C. Nuntadusit, M. Wae-hayee, A. Bunyajitradulya, S. Eiamsa-ard; Heat transfer enhancement by multiple swirling impinging jets with twisted-tape swirl generators, International Communications in Heat and Mass Transfer 39 (2012), pp. 102–107.

[55] L. Thielen, H.J.J. Jonker, K. Hanjalić; Symmetry breaking of flow and heat transfer in multiple impinging jets, International Journal of Heat and Fluid Flow 24 (2003), pp. 444–453.

[56] Ye-zheng Yu, Jing-zhou Zhang, Hua-sheng Xu; Convective heat transfer by a row of confined air jets from round holes equipped with triangular tabs, International Journal of Heat and Mass Transfer 72 (2014), pp. 222–233.

[57] Ye-zhen Yu, Jing-zhou Zhang, Yong Shan; Convective heat transfer of a row of air jets impingement excited by triangular tabs in a confined crossflow channel, International Journal of Heat and Mass Transfer 80 (2015), pp. 126–138.

[58] Wei He, Zhen-bing Luo, Xiong Deng, Zhi-xun Xia; Experimental investigation on the performance of a novel dual synthetic jet actuator-based atomization device, International Journal of Heat and Mass Transfer 142 (2019), pp. 118406

[59] L. Mangate, H. Yadav, A. Agrawal, M. Chaudhari; Experimental investigation on thermal and flow characteristics of synthetic jet with multiple-orifice of different shapes, International Journal of Thermal Sciences 140 (2019), pp. 344–357.

[60] A. Agrawal, G. Verma; Similarity analysis of planar and axisymmetric turbulent synthetic jets, International Journal of Heat and Mass Transfer 51 (2008), pp. 6194–6198.

[61] M. Al-Atabi; Experimental investigation of the use of synthetic jets for mixing in Vessels, Journal of Fluids Engineering 133 (2011), pp. 094503-1 - 094503-4.

[62] M.A. Feero, P. Lavoie, P.E. Sullivan; Influence of cavity shape on synthetic jet performance, Sensors and Actuators A 223 (2015), pp. 1–10.

[63] Lv Yuan-wei, Zhang Jing-zhou, Shan Yong, Tan Xiao-ming; Numerical investigation for effects of actuator parameters andexcitation frequencies on synthetic jet fluidic characteristics, Sensors and Actuators A 219 (2014), pp. 100–111.

[64] G. Buchberger, B. Jakoby, J. Schöftner, A. Schützenberger, B. Wiesmayr, W. Baumgartner, S. Puttinger, A. Brandl, W. Hilber; Simple synthetic jet actuators for cooling applications using soft or rigid magnets, 30th Eurosensors Conference, EUROSENSORS 2016, Procedia Engineering 168 (2016), pp. 1541 – 1546.

[65] C. Yao, F.J. Chen, D. Neuhart, J. Harris; Synthetic jet flow field database for CFD validation, NASA Langley Research Center, Hampton, 2nd AIAA Flow Control Conference, June 28 – July 1, Portland, Oregon, AIAA-2004-2218.

[66] Harinaldi, D. Rhakasywi, R. Defriadi; Flow and heat transfer characteristics of an impinging synthetic air jet under sinusoidal and triangular wave forcing, International Journal of Engineering & Technology IJET-IJENS Vol: 11, No: 03, pp. 29-36.

[67] Y. Zhang, P. Li, Y. Xie; Numerical investigation of heat transfer characteristics of impinging synthetic jets with different waveforms, International Journal of Heat and Mass Transfer 125 (2018), pp. 1017–1027.

[68] A. J. C. King, D. Jagannatha; Simulation of synthetic jets with non-sinusoidal forcing functions for heat transfer applications, 18th World IMACS / MODSIM Congress, Cairns, Australia, 13-17 July 2009, pp. 1732-1738.

[69] Lars Davidson; Fluid mechanics, turbulent flow and turbulence modeling, Division of Fluid Dynamics, Department of Applied Mechanics, Chalmers University of Technology, SE-412 96 G¨oteborg, Sweden, September 1, 2016, pp 24-25.

[70] S. Toll and M. Ekh; Mechanics of solids & fluids Part I: Fundamentals. Report, Div. of Material and Computational Mechanics, Dept of Applied Mechanics, Chalmers University of Technology, G¨oteborg, Sweden, 2011.

[71] Khaled Saleh; Simulation d'Écoulements Turbulents Solution Analytique de l'Équation de la chaleur avec des conditions aux limites particulières, Rapport de stage long, Mécanique des fluides numérique (CFD), EDF R&D, Département Mécanique des Fluides, Énergie et Environnement, Juillet 2007 - Août 2008, pp 17-20.

[72] S. B. Pope; Turbulent Flows, Cambridge University Press, 2000.

[73] Lars Davidson. Fluid mechanics, turbulent flow and turbulence modeling, Division of Fluid Dynamics, Department of Applied Mechanics, Chalmers University of Technology, SE-412 96 G¨oteborg, Sweden, September 1, 2016, pp 157-161.

[74] Launder, B. E., & Spalding, D. B; The numerical computation of turbulent flows, Computer Methods in Applied Mechanics and Engineering, 1974, 3(2), pp 269–289.

[75] Versteeg, Henk Kaarle, Malalasekera; An introduction to Computational Fluid Dynamics: The Finite Volume Method, 1995, pp 67-71.

[76] WILCOX, D. C; Reassessment of the scale-determining equation for advanced turbulence models. AIAA Journal, 26(11), (1988), 1299–1310.

[77] R. C. Morgans, B. B. Dally, G. J. Nathan, P .V. Lanspeary and D. F. Fletcher; Application of the revised WILCOX (1998) k-ω Turbulence model to a jet in co-flow, Second International Conference on CFD in the Minerals and Process Industries, CSIRO, Melbourne, Australia, 6-8 December 1999, pp 479-484.

[78] Menter, F. R; Two-equation eddy-viscosity turbulence models for engineering applications. AIAA Journal, 32(8), (1994), 1598–1605.

[79] H. Nouri, F. Ravelet; Introduction à la simulation numérique des écoulements : Application au transfert thermique sur plaque plane avec StarCCM+, DynFluid - Arts et Metiers ParisTech, 151 boulevard de l'Hôpital, 75013 Paris, France, 201, pp 13-14.

[80] S. V. Patankar ; Numerical Heat Transfer and Fluid Flow, Hemisphere Publishing Corporation, Washington DC, 1980, pp31-67.

[81] Z. Becer ; Investigation de la concentration de gaz d'électrons à deux dimensions 2DEG dans les Hétérostructures $n - Al_xGa_{1-x}As/In_yGa_{1-y}As/GaAs$ dopé sélectivement, Thèse de Magister, Departement de Physique, Université Mohammed Khider de Biskra, 2006, pp54-61.

[82] Chandratilleke TT, Jagannatha D, Narayanaswamy R; Heat transfer enhancement in microchannels with cross-flow synthetic jets, International Journal of Thermal Sciences, Volume 49, Issue 3, March 2010, Pages 504-513.

[83] Rizzetta, D.P., Visbal, M.R. and Stanek, M.J. (1999) ; Numerical Investigation of synthetic jet flow fields, AIAA Journal, Vol. 37 No. 8, pp. 919-927.